

Phase Field Modelling of Magnetoelasticity in Antiferromagnets



Robert Alexander Mackay

University of Leeds

School of Physics and Astronomy

Submitted in accordance with the requirements for the degree of

Doctor of Philosophy

February, 2025

Intellectual Property Statement

The candidate confirms that the work submitted is his own and that appropriate credit has been given where reference has been made to the work of others.

This copy has been supplied on the understanding that it is copyright material and that no quotation from the thesis may be published without proper acknowledgement.

The right of Robert Alexander Mackay to be identified as Author of this work has been asserted by him in accordance with the Copyright, Designs and Patents Act 1988.

© 2025 The University of Leeds and Robert Alexander Mackay.

Acknowledgements

Firstly, I'd like to thank both of my supervisors, Dr. Joseph Barker and Dr. Steve Fitzgerald, for their advice, support and inspiration throughout my PhD, and for the opportunity to do this PhD project, something I wouldn't have thought possible years ago. Furthermore, I want to acknowledge Prof. Stephen McVitie of the University of Glasgow for informing me of this opportunity and for his advice. In the same vein, I'd like to thank the Bragg Centre, in particular Prof. Edmund Linfield and Dr. Andrew Lee, for their support, financial and otherwise, of this project, as well as the opportunity to present my work at multiple conferences. Additionally, my time at the University of Leeds wouldn't have been the same without my friends and colleagues from Barker Lab, Dr Thomas Nussle, Dr Ioannis Charalampidis and Dr Sean Stansill, who helped me improve academically through discussions and advice, and kept me going through the PhD during the tougher times and beyond. I'd also like to acknowledge the support and valuable advice I have received from the wider Condensed Matter Physics department at the University of Leeds.

I'd also like to acknowledge the other important people in my personal life, whose inspiration and support has been invaluable during the course of this work and well beyond. To start, I wish to show my deepest gratitude for my family for their unyielding support during my research journey and beyond, in particular my parents Audrey & Kenneth, my brother Ross, my late grandparents James and Elizabeth, and of course my little feline family members, Odin and the late Ginger and Toffee. Next, I'd like to give my appreciation to the friends I met in Leeds along the way, who made my experience here all the more enjoyable, in particular David Thompson, Robert Elkington, Reece Beadsley, Matthew Yusuf and Iason Sofos. Last but certainly not least, I'd like to acknowledge the support from my friends back home, especially during the lockdown era; this includes, but is not limited to, Jack Peggie (plus Ellen and Raymond Bennett), Shannon Donaldson, Josh Hail, Owen McWilliams, Niall & Jemma McHugh, Gordon McNicol, Amy Young, Adam Gray, Finlay Powlesland-Spears, Matthew Pound, Josh Donaldson and Georgie Pritchard.

This work was undertaken on ARC4, part of the High Performance Computing facilities at the University of Leeds, UK.

Abstract

The global need for data storage only grows year on year, imposing additional hardware requirements for devices we use in our day-to-day lives. However, we are fast approaching the technical limit for data bit density in devices currently in circulation. We therefore have to look to different materials and device types to circumvent these technical limitations. Antiferromagnetic materials have received interest in this field due to their impervious nature with respect to stray magnetic fields, allowing closer data bit packing, and the terahertz (THz) frequency spin dynamics present in these materials is an order of magnitude higher than that present in ferromagnets, allowing faster data read/write. For these materials to be used effectively for this purpose, however, the magnetic structure of these materials needs to be thoroughly understood. This, presently, is not the case. A significant area of interest is the observed presence of magnetic domains in these materials, which can not be explained by magnetostatics, the case for ferromagnets. Works have been undertaken to explain the presence of these domains, using the magnetoelastic coupling. These important works gave analytic explanations as to how antiferromagnetic domains form for specific sample geometries and boundary conditions. We seek to expand on these important works by creating a software package to examine the magnetoelastic effect on antiferromagnets for general sample geometries and device level ($> 10\text{nm}$) lengthscales. We use the phase field model as the basis of our work, allowing us to explore larger lengthscales without massively increased computational costs due to us not having to consider precessional dynamics, and adapt a modular approach to the problem. This thesis details how we developed our software package, and how we tested it. We demonstrate the large effect that inclusion defects have on the magnetic structure of antiferromagnets, showing the antiferromagnetic domains produced as a result. We analyse how the size, shape and location of these defects, as well as altering the magnetoelastic coupling strength, affect the nucleation of these domains and the resultant change in shape and size of the domains produced. The effect of these defects on already present domain textures (domain walls) is also studied, showing even the presence of a single small defect is enough to distort the domain wall. In producing this software package, we believe we have given a platform for further examination of the magnetic structure of antiferromagnets, and in doing so inform future implementation of antiferromagnets in data storage devices.

CONTENTS

1	Background Information	1
1.1	Motivation	2
1.2	Magnetism: An Overview	5
1.2.1	Ferromagnetism	5
1.2.2	Antiferromagnetism	6
1.2.3	Magnetocrystalline Anisotropy	7
1.2.4	Magnetic Domains	8
1.3	Strain & Magnetoelasticity	11
1.3.1	Elastic Strain	11
1.3.2	Magnetoelasticity	12
1.4	Dislocations and Defects: A Brief Overview	18
1.4.1	Eshelby Inclusion	19
1.4.2	Crystalline Dislocations	21
1.5	Introduction to Phase Field Modelling	26
2	Development of MESMER	36
2.1	The MOOSE Framework	37
2.2	Finite Difference and Finite Element Methods	37
2.2.1	Finite Difference Method	37
2.2.2	Finite Element Method	40
2.3	Phase Field Model	43
2.3.1	Ferromagnetic Exchange	43
2.3.2	Antiferromagnetic Exchange (<i>ADImprovedAFM</i>)	44
2.3.3	Magnetocrystalline Anisotropy	45

2.3.4	Elasticity	46
2.3.5	Magnetoelasticity	48
2.4	Defect Modelling	48
3	Verification of MESMER	53
3.1	Using Domain Wall Width Analysis to Verify Exchange and Anisotropy Implementation	54
3.2	Using the Spin-Flop and Spin-Flip Transition to Verify the Antiferromagnetic Exchange	58
4	Nucleation of Magnetic Domains in Antiferromagnets by the Magnetoelastic Coupling	62
4.1	Nucleation of Magnetic Domains in Antiferromagnets by the Magnetoelastic Coupling	63
4.1.1	Antiferromagnet without Magnetoelastic Coupling - 2D	63
4.1.2	Domain Nucleation by a Single Defect with Magnetoelastic Coupling	64
4.1.3	Interaction of Domains Nucleated by Two or More Defects	72
5	Magnetoelastic Interaction of Inclusion Defects with Domain Walls	88
5.1	Interaction of Multiple Inclusion Defects and Their Interaction with Domain Walls	89
5.1.1	Interaction of a Single Defect with Magnetoelastic Coupling with a Domain Wall	89
5.1.2	Interaction of Multiple Defects with Magnetoelastic Coupling with a Domain Wall	94
5.1.3	Interaction of a Domain Wall with a Single Defect at Variable Distance	97
6	Conclusions	105
6.1	Conclusions	106
6.2	Future Work	108
	References	110

LIST OF FIGURES

1.1	Diagram showing possible electron spin alignments for an Mn-O-Mn ion chain, for both ferromagnetic and antiferromagnetic configurations. Adapted from [1].	8
1.2	Example of a closed-flux domain structure in a ferromagnet, which fully minimises the magnetostatic energy of the ferromagnet. Adapted from [2].	9
1.3	Micromagnetic simulations of an example bar ferromagnet, with varying exchange stiffness A , using the software package <i>mumax</i> ³ [3], starting with the initial condition of magnetisation wholly aligned with the z -axis. The direction of the unit magnetisation vector is visualised. The values of the exchange stiffness for each simulation is given underneath each subfigure. It should be noted these simulations contain no magnetocrystalline anisotropy. Visualised using Paraview [4].	10
1.4	Illustration of the form of the elastic stiffness tensor in Voigt notation for different crystal classes from [5]. Only tensor components above and including the diagonal are displayed, as the others are given by previously discussed symmetry arguments. The \bullet symbols represent independent tensor components, with lines between these elements representing that they are equivalent. The \cdot symbols represent zero elements. The \circ symbols, with a line attached to a \bullet , indicate that the \circ element is equal to the negative of the \bullet element. $*$ symbols with attached lines indicate equality with the attached elements. $+$ components are the average of the top-left-most component and the component to the right (i.e. $\frac{1}{2}(C_{11} - C_{12})$), with a line between them representing equivalence between these elements.	13

1.5 Diagram describing the Eshelby inclusion analysis. Part a) shows the initial ill-fitting material (inclusion) and its surrounding material (the matrix). Part b) then shows the inclusion being removed, and being allowed to expand under a "stress-free" strain (the eigenstrain). Part c) shows the application of tractions T_i to the now-expanded inclusion back to its original shape. Finally, part d) shows the inclusion being re-inserted back into the material, where a "canceling" force F_i , applied to surface S_{Inc} (the surface exposed after the inclusion was removed), is applied to cancel the tractions used to return the inclusion to its original state, allowing the calculation of the strain field in the material. Adapted from [6]. 20

1.6 Stress tensor components resulting from an edge dislocation along the z -axis, with Burgers vector $\mathbf{b} = [0, 0.419, 0]$, implemented via initial conditions in MOOSE [7]. Visualised using Paraview [4]. 24

1.7 Stress tensor components resulting from an edge dislocation along the z -axis, with Burgers vector $\mathbf{b} = [0, 4.19, 0]$ (in units of \AA). As a contrast to Figure 1.6, these components are shown using a discrete, atomic supercell (where we visualise the top face) using the software package AtomsK [8], and therefore the atomic displacements resulting from the insertion of the half-plane of atoms are easily discernible. Visualised using OVITO [9]. 25

1.8 Stress tensor components resulting from a screw dislocation along the y -axis, with Burgers vector $\mathbf{b} = [0, 0.419, 0]$, implemented via initial conditions in MOOSE [7]. Note the absence of the σ_{11} , σ_{22} and σ_{33} as these terms are equal to zero, a key feature of screw dislocations. Visualised using Paraview [4]. . . . 27

1.9 Top and front faces of the crystalline lattice featuring a screw dislocation, with the dislocation line along the y -axis and the z -axis being the axis perpendicular to the dislocation line along which displaced atoms are allowed to move to relax the system. The magnitude of the Burgers vector is 4.19\AA . The xy and yz -components of stress are visualised (qualitatively) using a colour map (shown next to the lattice, where the blue regions indicate a negative component and green regions indicate a positive component). Created with AtomsK [8] and visualised using OVITO [9]. 28

1.10	Perspective view of the front-face of the crystalline lattice with the screw dislocation shown in Figure 1.9. Created with AtomsK [8] and visualised using OVITO [9].	29
1.11	$\dot{\eta}$ with respect to η calculated by the input of the polynomial free energy system into the Allen-Cahn Equation (1.52). Note that $\dot{\eta}$ is only zero at $\eta = -1$, and has opposite sign on either side of this point, showing that the system will relax to the $\eta = -1$ point.	32
2.1	Temperature distribution throughout our material, evolved through time according to the one-dimensional heat equation.	39
2.2	Example diagram of a sample being split into elements, for use in the FEM. We represent the nodal value of point i as f_i and the internal elemental function of element j as e_j . Boundary conditions at y_1 and y_3 give $f_5 = f_6 = f_7 = a$ and $f_8 = f_9 = f_{10} = f_{11} = f_{12} = b$ respectively. To find the values of the non-nodal points within each element, we will need to interpolate the solution function throughout the element. Adapted from [10].	41
2.3	Easy (green), medium (yellow) and hard (red) axes for regions of values of the two cubic anisotropy constants, from an isometric perspective of the positive octant.	47
2.4	An example of an Eshelby inclusion defect, as implemented in our simulations. The defect concentration c , in Figure 2.4a, is directly related to the eigenstrain, observable in the centre in Figures 2.4b and 2.4d.	50
2.5	Example of an inverted defect configuration, where the top-right defect is inverted (the sign variable s is set to -1) and the bottom-left defect is not inverted (the sign variable s is set to 1).	51
3.1	Steady-state solution of our domain wall simulation, which we can use to verify the implementation of ferromagnetic coupling, uniaxial anisotropy and the unit magnetisation vector constraint by fitting the magnetisation profile.	56

3.2	An example of the fitting profiles used to ascertain the domain wall width δ . The value of 64.13, in units of nm, is the exact domain wall width; the value we obtain by fitting is 64.17 in the same units, which is a convincing match, verifying our implementation of the magnetocrystalline anisotropy and the ferromagnetic exchange in our model. The domain wall is centered at $x = 500\text{nm}$ and has a magnitude of 1.	57
3.3	Graph of domain wall width δ (in nm) versus time (in arbitrary units), showing the convergence of the model towards the correct analytic result. This result verifies that the exchange interaction, the uniaxial anisotropy and the magnetisation vector normalisation are working correctly. The values used in this plot were obtained from the fitting profiles, an example of which can be observed in Fig. 3.2.	57
3.4	Graphs showing magnetisation vectors of the two magnetic sublattices vs the magnetic induction applied to the antiferromagnet for different ranges of applied magnetic induction. The analytic flop/flip points are illustrated on Fig. 3.4a/3.4b respectively with blue dotted lines. The results obtained from our simulation match very well with the analytic results, which is particularly obvious in the spin flop case. This verifies that antiferromagnetic coupling is working correctly.	61
4.1	Néel vector profile for a 2D antiferromagnet simulation, where the magnetelastic coupling is not present.	64
4.2	Néel vector profile of the 2D antiferromagnet with an inclusion defect located in the centre of the material and a magnetoelastic coupling is present, where we have a weaker λ_{100} term. The defect location is highlighted with a white outline.	66
4.3	Néel vector profile of the 2D antiferromagnet with an inclusion defect located in the centre of the material and a magnetoelastic coupling is present, where we have a very strong λ_{100} term. The defect location is highlighted with a white outline.	67
4.4	Néel vector profile of the 2D antiferromagnet with an inclusion defect located in the centre of the material and a magnetoelastic coupling is present, where we have a very strong λ_{111} term. The defect location is highlighted with a white outline.	67

4.5	Graph of domain area versus both of the magnetostriction coefficients.	68
4.6	Néel vector profile for the offset defect case, where the defect is located at the top-right, where we have a very strong λ_{100} term. The defect location is highlighted with a white outline.	69
4.7	Néel vector profile for the offset defect case, where the defect is located at the top-right, where we have a weaker λ_{100} term. The defect location is highlighted with a white outline.	69
4.8	Graph of domain area versus the λ_{100} magnetostriction coefficient, for the case of a defect located at the centre of the material and the case of a defect located near the top-right of the material.	70
4.9	Néel vector profile result from the simulation where we have a single rectangular defect in the centre, where we have magnetoelastic coupling with a weak λ_{100} term. The defect location is highlighted with a white outline.	71
4.10	Néel vector profile result from the simulation where we have a single rectangular defect in the centre, where we have magnetoelastic coupling with a strong λ_{100} term. The defect location is highlighted with a white outline.	71
4.11	Graph of the domain area versus λ_{100} for the original square defect and for a rectangular defect.	72
4.12	λ_{100} parameter sweep for a $10\text{nm} \times 10\text{nm}$ defect, a $8\text{nm} \times 8\text{nm}$ defect and a $6\text{nm} \times 6\text{nm}$ defect, all located at the centre of the material.	73
4.13	Néel vector profile and hydrostatic pressure values for the case of two tensile defects, for a separation distance of 20nm . The defect locations are highlighted with a white outline.	74
4.14	Néel vector profile and hydrostatic pressure values for the case of two tensile defects, for a separation distance of 10nm . The defect locations are highlighted with a white outline.	74
4.15	Néel vector profile and hydrostatic pressure values for the case of two tensile defects, for a separation distance of 60nm . The defect locations are highlighted with a white outline.	75
4.16	Néel vector profile and hydrostatic pressure values for the case of two tensile defects, for a separation distance of 95nm . The defect locations are highlighted with a white outline.	75

4.17 Plot of domain area versus the separation distance of the two tensile defects, for two different values of λ_{100} . The error bars are given by varying the threshold by which we verify if a domain is present. The horizontal bars are given by the expected domain area of two non-interacting defects; the red bar represents the domain area of two non-interacting defects for the original value of λ_{100} , and the green bar represents the same for the doubled value of λ_{100}	76
4.18 Néel vector profile and hydrostatic pressure values for the case of two compressive defects, for a separation distance of 10nm. The defect locations are highlighted with a black outline.	77
4.19 Néel vector profile and hydrostatic pressure values for the case of two compressive defects, for a separation distance of 35nm. The defect locations are highlighted with a black outline.	77
4.20 Néel vector profile and hydrostatic pressure values for the case of two compressive defects, for a separation distance of 55nm. The defect locations are highlighted with a black outline.	78
4.21 Néel vector profile and hydrostatic pressure values for the case of two compressive defects, for a separation distance of 80nm. The defect locations are highlighted with a black outline.	78
4.22 Graph of domain area versus separation distance of two compressive defects, for the cases of our standard magnetostriction coefficient and the case where it is doubled. The horizontal lines represent the total domain area which would be represented by two non-interacting defects, for both of the magnetostriction coefficient cases. The bars represent the same as described in Figure 4.17. . . .	79
4.23 Néel vector profile, for the case of two compressive defects separated by 60nm, and a λ_{100} value of $1.14 \cdot 10^{-4}$. The defect locations are highlighted with a black outline.	80
4.24 Néel vector profile and hydrostatic pressure values for the case of a tensile and a compressive defect, for a separation distance of 35nm. The defect locations are highlighted with a white outline for the tensile defect and a black outline for the compressive defect.	80

4.25 Néel vector profile and hydrostatic pressure values for the case of a tensile and a compressive defect, for a separation distance of 70nm. The defect locations are highlighted with a white outline for the tensile defect and a black outline for the compressive defect.	80
4.26 Néel vector profile and hydrostatic pressure values for the case of a tensile and a compressive defect, for a separation distance of 85nm. The defect locations are highlighted with a white outline for the tensile defect and a black outline for the compressive defect.	81
4.27 Graph of domain area versus separation distance of the tensile defect and the compressive defect, for the cases of our standard magnetostriction coefficient and the case where it is doubled. The horizontal lines represent the total domain area which would be represented by two non-interacting defects, for both of the magnetostriction coefficient cases.	82
4.28 Graph of domain area versus separation distance of the tensile defect and the compressive defect, for the cases of our standard magnetostriction coefficient and the case where it is doubled. Here, we have switched the positions of the tensile and compressive defects relative to Figure 4.27.	83
4.29 Néel vector profiles for corresponding defect patterns resembling those of a standard six-sided dice (D6). The defect locations are highlighted with a white outline.	85
4.30 Néel vector profiles for corresponding defect patterns resembling those of a standard six-sided dice (D6), where we switch certain defects to be compressive, as specified in the individual captions. The defect locations are highlighted with a white outline for tensile defects and a black outline for compressive defect.	86
5.1 Néel vector profiles for a central defect (of different types) interacting with a domain wall, with a strong magnetoelastic coupling, with $\lambda_{100} = -1.14 \cdot 10^{-4}$. The defect locations are highlighted with a white outline for the tensile defect and a black outline for the compressive defect.	91
5.2 Néel vector profiles for a central defect (of different types) interacting with a domain wall, with a strong magnetoelastic coupling, with $\lambda_{111} = -5.71 \cdot 10^{-5}$. The defect locations are highlighted with a white outline for the tensile defect and a black outline for the compressive defect.	92

5.3 Néel vector profiles for a central defect (of different types) interacting with a domain wall with $\lambda_{100} = -1.43 \cdot 10^{-5}$. The defect locations are highlighted with a white outline for the tensile defect and a black outline for the compressive defect.	93
5.4 Néel vector profiles for a central defect (of different types) interacting with a domain wall with $\lambda_{111} = -7.14 \cdot 10^{-6}$. The defect locations are highlighted with a white outline for the tensile defect and a black outline for the compressive defect.	95
5.5 Néel vector profiles for a tensile defect and a compressive defect interacting with a domain wall, with differing λ_{100} coefficients. The defect locations are highlighted with a white outline for a tensile defect and a black outline for a compressive defect.	96
5.6 Néel vector profiles for a compressive defect and a tensile defect interacting with a domain wall, with differing λ_{100} coefficients. The defect locations are highlighted with a white outline for a tensile defect and a black outline for a compressive defect.	98
5.7 Néel vector profiles for two tensile defects interacting with a domain wall, with differing λ_{100} coefficients. The defect locations are highlighted with a white outline.	99
5.8 Néel vector profiles for two compressive defects interacting with a domain wall, with differing λ_{100} coefficients. The defect locations are highlighted with a black outline.	100
5.9 Néel vector profiles for defects in the negative x half of the material with respect to the centre, where a domain wall is already present in the sample. The defect locations are highlighted with a white outline.	102
5.10 Néel vector profiles for defects in the negative x half of the material with respect to the centre, where a domain wall already exists in the sample (by initial conditions). The defect locations are highlighted with a white outline.	103
5.11 The missing case from Figures 5.9 and 5.10, that of a central defect with a domain wall (initial condition). The defect location is highlighted with a white outline.	104

LIST OF TABLES

4.1	Terms used in the simulation of an antiferromagnet without magnetoelastic coupling, together with the relevant equations and parameter values.	63
5.1	Terms used in the simulation of an antiferromagnet with magnetoelastic coupling, together with the relevant equations and parameter values.	89

Abbreviations

AFM	Antiferromagnet	FM	Ferromagnet
PDE	Partial Differential Equation	FEM	Finite Element Modelling
PEEM	Photo Emission Electron Micro- scopy	XMLD	X-ray Magnetic Linear Dichroism
DFT	Density Functional Theory	FMR	Ferromagnetic Resonance
SAMR	Small-Angle Magnetization Rota- tion	SMFMR	Strain Modulated Ferromagnetic Resonance
LLG	Landau-Lifshitz-Gilbert		

CHAPTER 1

Background Information

1.1 Motivation

Antiferromagnetism, originally discovered in 1932 by Louis Néel [11], describes an alignment of magnetic moments wherein neighbouring magnetic moments align antiparallel to each other, in contrast to the parallel alignment present in ferromagnets. He then in 1947 described a new type of magnetic order to explain experimental results which gave a far smaller magnetisation than the magnitude of the constituent magnetic moments would indicate [12]. These results were explained by Néel as an uncompensated antiferromagnet; wherein moments aligned along the magnetisation direction are partially cancelled by others aligned antiparallel; this magnetic alignment hence became known as ferrimagnetism [13]. For these contributions to science, he was awarded the Nobel Prize in Physics in 1970. However, even the discoverer of antiferromagnetism was sceptical of the usefulness of these materials; indeed, during his Nobel Prize speech in 1970, Néel famously referred to the materials as being “interesting but useless”. The veracity of this claim has been put into question in more recent times, as works have been published that use these materials in data storage devices, such as those conceived by the group of Tomas Jungwirth.

These devices aim to overcome limitations of conventional magnetic data storage, which predominantly uses ferromagnetic materials. One of these limitations is the limit on the minimum areal density of memory bits, which we can explore by describing the magnetic recording trilemma [14]. The issue arises when the areal density bypasses a certain critical lower value, where thermal fluctuations are energetically sufficient to overcome the energy of the magnetic anisotropy, to flip the magnetisation state of the memory bit. A way to stop these bits from spontaneously flipping to another magnetisation state would be to increase the anisotropy; however, this simultaneously increases the difficulty in writing to these same bits, and increasing the writing field incurs the risk that other bits in the region are flipped also, in error. This therefore means we have to compromise between the size of memory bits, their anisotropy, and the writing field applied, hence giving us the aforementioned trilemma. Antiferromagnets offer us a way to overcome this trilemma, due to the fact that antiferromagnets are resistant to magnetic stray fields; meaning that a strong write field targeting one memory bit would be unlikely to affect another nearby memory bit, allowing denser data storage [15]. Additionally, antiferromagnets have terahertz frequency spin dynamics, giving additional benefit in the form of faster magnetic switching when recording data [16]. However, given the resistance antiferromagnets have to external fields, it is prudent to find alternative ways to read and write data to these devices, a concept that has seen much exploration in recent years.

Antiferromagnetic data storage devices explored in these works include those which use cooling under an applied magnetic field to store data [17] and ones that use electrical current to switch domain states [16, 18]. In addition to these devices, applicability of antiferromagnets in the rising field of neuromorphic computing has been discussed, something that was implied by their memristor-like behaviour, with an increased number of applied current pulses leading to an increased electrical read-out signal [19]. Furthermore, antiferromagnetic domain walls, driven by magnetic field pulses (or by a spin-Hall torque), can be used to mimic a human neuron as well as its associated mechanisms [20]. However, for all these applications to be fully realised, and for the optimisation of future devices, the domain structures of these materials needs to be fully understood.

In particular, the reason for domain formation in antiferromagnets has not been fully explored at the device level, despite the fact that they have been experimentally observed, for example by Grzybowski et al. [21] using photo emission electron microscopy (PEEM) with x-ray magnetic linear dichroism (XMLD) giving the contrast required for imaging; indeed, the fact that these antiferromagnetic domains exist underpins the functionality of many of the previously discussed data storage devices. This is not to say that research has not been undertaken in this vein, at the microscopic level, this has been explained analytically, using the magnetoelastic coupling, for example in [22, 23], which look at the relation of the magnetism to the mismatch strain between a magnet and its substrate, with further work [24] exploring the connection between this and device patterning, demonstrating the interplay between the short-range anisotropy (from the patterned edges) and the long-range magnetoelastic effect. However, these analytic explanations are only applicable for specific geometries and at small lengthscales. Alternative studies have looked at numerically modelling antiferromagnets, such as by evaluating coupled Landau-Lifshitz-Gilbert equations [25] or by evaluating equations of motion resulting from the Euler-Lagrange equation [26]. In both cases, these models involve resolving the precessional dynamics of the Néel vector. Given the sample sizes we wish to simulate have dimensions around and above magnitude $\sim 100\text{nm}$, and that antiferromagnetic domain walls can potentially be on the length scale of hundreds of nanometres [27], the complexity of these simulations therefore skyrockets in this case as we would have to simulate an increasingly impractical number of pairs of precessing magnetic moments (we will describe what we mean by precessing in a brief aside in Subsection 1.5).

In order to overcome this, other studies have used micromagnetics (in brief, where we treat a selection of magnetic moments in a selected element of the sample as a collective and ascribe

collective characteristics, for example a net magnetisation vector \mathbf{M}) to explore domain formation in antiferromagnets [28]. In [28], domains are nucleated with the help of preferred boundary connections, arising as a result of crystallographic continuity, which are inserted as a free energy term in the following Monte-Carlo simulation. Whilst important, this work only explores the domain structure specific to nickel oxide and its crystal structure. Another example of numeric modelling of domain walls in antiferromagnets is the work of Consolo et al. [29], where it is modelled under the magnetoelastic formalism, with the strain originating both from the magnetoelastic coupling (modelled as “incompatibility” charges in an analogy to electrostatics) and the reaction to said strains to preserve the structural integrity of the material. The former strain, known in our work and in [29] as “spontaneous” strain (for which we will use the notation ξ in this work), will be utilised in this work to describe the effect the magnetoelastic coupling has on the strain in the material. This important work also employs energy minimisation, a method we will also employ, to find the energetically preferred domain wall states in the relevant system. The works described previously not only provided us with information and inspiration for the topic and methods deployed in this thesis, but also gave us the ideas with which we set out to contribute further to this interesting and rapidly evolving area of physics. We wish to use the knowledge gained in the aforementioned works to expand our understanding of antiferromagnetic domains to the device level, using the magnetoelastic coupling. We also wish to do so without experiencing the drawbacks of sample geometry specificity, having to resolve precessional dynamics of pairs of magnetic moments, and being able to use a generalised strain field. These requirements led us to the selection of the phase field model for our future endeavours. The phase field model, applied in a variety of diverse fields [30, 31] as well as to magnetism [32], is an energy minimisation method, where we “push” variables down their free energy landscape. This method has the key advantage of being able to incorporate different physical phenomena by including their relevant free energy densities, making the method highly adaptable. To our knowledge, no other works in the literature have used the phase field model to explore the domain structure in antiferromagnetic materials. In order for us to develop our numerical model using this method, we first explore the origin of antiferromagnetism, the magnetoelastic coupling and other important phenomena before developing, testing, using and evaluating our model.

1.2 Magnetism: An Overview

1.2.1 Ferromagnetism

To explain the ferromagnetic exchange interaction, we must first discuss the Pauli exclusion principle and Hund's Rule (specifically Hund's Rule of Maximum Multiplicity), as in this discussion of ferromagnetism (and antiferromagnetism), we will limit ourselves to discussions of magnetic insulators; for metallic substances, other models such as the Landau model and the Weiss model can be considered for ferromagnets and antiferromagnets (in the case of the Weiss model) [1]. The Pauli exclusion principle states that no two electrons within an atomic structure can possess the same values of the four quantum numbers (the principal quantum number n , azimuthal quantum number ℓ , magnetic quantum number m_ℓ and the spin quantum number m_s). More colloquially, if two electrons are in the same atomic orbital, they cannot also have the same spin state; since electrons can only have two spin states ($\frac{1}{2}$ and $-\frac{1}{2}$), this means the electronic orbitals can only be filled with a maximum of two electrons.

Hund's Rule of Maximum Multiplicity states that, in the open electronic shell, degenerate orbitals are filled singly before double-occupation begins, in order to maximise the total spin quantum number of the system. Let us assume we have an atomic element with a partial occupation of the $3d$ subshell. The $4s$ subshell (which is of lower energy than the $3d$ subshell; see the Aufbau principle [33]) is fully occupied; the other electrons are then left to fill the outer subshell, $3d$. The $3d$ subshell consists of five orbitals (given by the total possible amount of values for the magnetic quantum number, which for the $3d$ subshell is the range of integers between -2 and 2 , so five), so according to Hund's Rule of Maximum Multiplicity and the Pauli exclusion principle, these five orbitals are filled singly before being doubly occupied. The unpaired electrons, all possessing the same spin state, are then free to interact magnetically with the unpaired electrons of other nearby atoms.

Using an analogy to bar magnets, if these electrons, which are, in themselves, magnetic dipoles, are in the same spin state (and thus the same dipole orientation) will repel each other. This, in turn, will lower the electrostatic energy caused by the repulsion between the two negatively-charged electrons. Therefore, to lower the energy of the system, electrons in the immediate vicinity to each other will seek to adopt the same spin state, to form localised domains. This phenomenon, where we have regions of uniformly aligned spin states without a magnetic field being applied, is known as spontaneous magnetisation, and is a key feature of ferromagnetism (and ferrimagnetism). Furthermore, this compulsion that spins in ferromagnets have to align

with each other is known as ferromagnetic exchange, or simply the exchange interaction. At the continuum level, the ferromagnetic exchange can be described by the free energy density [34]

$$F_{ex} = \int_{\Omega} A [(\nabla m_x)^2 + (\nabla m_y)^2 + (\nabla m_z)^2] dV, \quad (1.1)$$

where Ω is the volume of the sample, A is the exchange stiffness (in units of Am^{-1}), m_i is the i^{th} component of the unit magnetisation. Atomic species with less unpaired electrons in the d- or f- subshells may have their spin-states aligned instead by the application of a magnetic field (to minimise the Zeeman energy); this ordering is known as paramagnetism. However, this description, as it stands, does not explain how antiferromagnetic coupling originates. For the case of ionic antiferromagnets, we may look at the phenomena of superexchange.

1.2.2 Antiferromagnetism

To explain the magnetic superexchange interaction, let us take the ionic antiferromagnet MnO , an insulator, as an example. Following the description outlined in [1], we will be making the assumption that the magnetic behaviour of the manganese ions are as a result of the single unpaired electrons (the case for multiple unpaired electrons follows by a similar logic). We can then look at an individual chain of two manganese ions ionically bonded to a single oxygen atom (with two p -subshell electrons as bonding electrons). If we assume the manganese electrons have an antiferromagnetic spin alignment, we can see in the associated diagram (Figure 1.1) that this ground state can mix with the excited states, which lowers the overall kinetic energy of the system.

However, this mixing of the ground state with excited states is prohibited for a ferromagnetic alignment of the manganese electrons by the Pauli exclusion principle. Hence, if the ferromagnetic alignment were to be adopted by the manganese ions, this would result in a higher energy state. Therefore the manganese ions will adopt the antiferromagnetic alignment to reduce the overall energy of the system; this explanation of antiferromagnetic superexchange applies to antiferromagnetic ionic substances, which, while limiting, explains the magnetic exchange for the substances modelled in this work, particularly the antiferromagnet Nickel Oxide (NiO), which we will study due to its antiferromagnetic exchange, cubic crystal structure, and comparatively high magnetoelastic coupling strength. It should be noted, however, that this indirect exchange interaction may be antiferromagnetic or ferromagnetic in nature. For collinear cubic antiferromagnets, the antiferromagnetic coupling may be described by the following free

energy density,

$$f_E = J (m_{1x}m_{2x} + m_{1y}m_{2y} + m_{1z}m_{2z}), \quad (1.2)$$

where f_E is the antiferromagnetic exchange energy density in units of $\text{meV}(\text{nm})^{-3}$, J is the exchange constant in units of $\text{meV}(\text{nm})^{-3}$, and \mathbf{m}_a is the unit magnetisation vector of the a^{th} magnetic sublattice.

The nature of this exchange can be qualitatively described by the ‘‘Goodenough-Kanamori’’ rules, taken from a series of influential papers from the authors of the same name [35–37]. These rules stipulate that superexchange between the half-filled orbitals of metallic ions is strongly antiferromagnetic (as we outlined above), whereas the superexchange between half-filled and full orbitals is ferromagnetic. Additionally, the superexchange between empty orbitals and half-filled or filled orbitals can have either character; generally, however, the ferromagnetic alignment is preferred. Given the considerations before, the antiferromagnetic exchange will usually win out in a mixed configuration of these scenarios. An algebraic representation of these rules is given in [38], as well as corrections to these original formulations. Of course, the previous only explains antiferromagnets which arise through superexchange; there are antiferromagnetic conductors, of which the metallic alloy Mn_2Au is an example [39], whose antiferromagnetism has to be explained by direct exchange, but these will not be studied in this work.

1.2.3 Magnetocrystalline Anisotropy

Magnetocrystalline anisotropy is a phenomenon where interaction between the magnetisation and the crystal lattice the magnetic atoms belong to, leads to certain magnetisation directions becoming energetically favourable. The preferred direction(s) depend on the symmetry of the crystal lattice and the geometry of the sample. Two prominent examples are the uniaxial anisotropy, represented by the free energy density f_{Uni} (in units of $\text{meV}(\text{nm})^{-3}$),

$$f_{\text{Uni}} = K_{\text{Uni}} (1 - m_z^2), \quad (1.3)$$

for a uniaxial anisotropy along the z -direction. K_{Uni} is the uniaxial anisotropy constant in units of $\text{meV}(\text{nm})^{-3}$. Here, $K_{\text{Uni}} > 0$ corresponds to an easy-axis anisotropy (here along the z -axis), and $K_{\text{Uni}} < 0$ corresponds to an easy-plane anisotropy (here along the $x - y$ -plane). Alternatively, if our underlying crystal lattice has cubic symmetry, we could have a cubic anisotropy, represented by the energy density f_{Cub} (in units of $\text{meV}(\text{nm})^{-3}$),

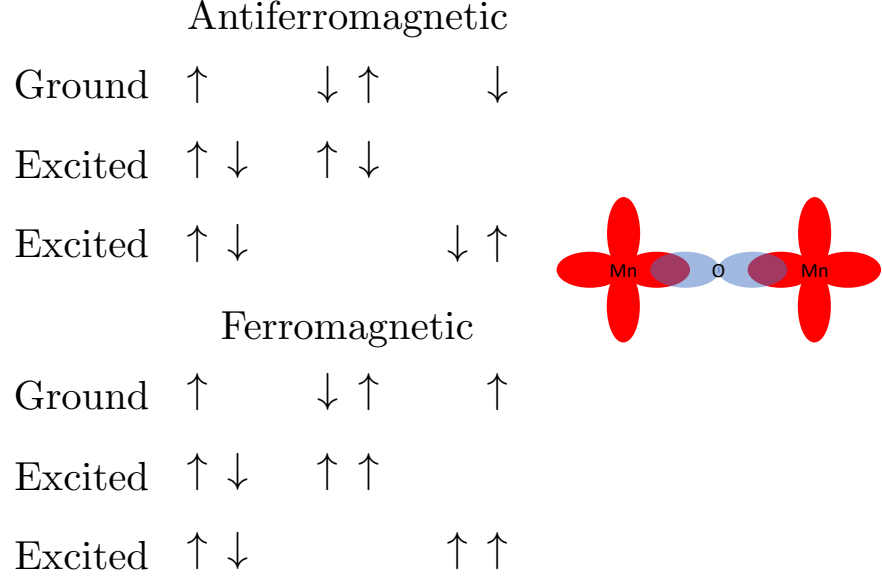


Figure 1.1: Diagram showing possible electron spin alignments for an Mn-O-Mn ion chain, for both ferromagnetic and antiferromagnetic configurations. Adapted from [1].

$$f_{\text{Cub}} = K_1 (m_x^2 m_y^2 + m_x^2 m_z^2 + m_y^2 m_z^2) + K_2 (m_x^2 m_y^2 m_z^2), \quad (1.4)$$

where K_1 and K_2 are the first and second order anisotropy constants respectively, both with units of $\text{meV}(\text{nm})^{-3}$. This cubic anisotropy will become instrumental in our later description of the magnetoelastic coupling.

1.2.4 Magnetic Domains

Magnetic domains are regions of magnetic material which share the same magnetisation direction, where magnetisation (units of Am^{-1}) is the volumetric density of the resultant magnetic moment over a given volume V ,

$$\mathbf{M} = \frac{\sum_V^i \boldsymbol{\mu}_i}{V}, \quad (1.5)$$

where $\boldsymbol{\mu}$ are magnetic dipole moments, in units of Am^2 , and V is the volume of the region of magnetic material (in m^3). Whilst the magnetic exchange will cause a perfectly ordered ferromagnet (and ferrimagnet) to have totally uniform magnetisation (a perfectly ordered antiferromagnet will have zero total magnetisation), other phenomena may cause this uniform

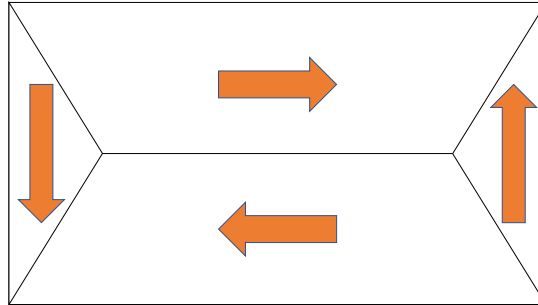


Figure 1.2: Example of a closed-flux domain structure in a ferromagnet, which fully minimises the magnetostatic energy of the ferromagnet. Adapted from [2].

magnetisation state to break into smaller regions of differing magnetisation; in other words, a multidomain state. In ferromagnets (and ferrimagnets), the magnetostatic interaction is the driving mechanism for domain formation.

The magnetostatic interaction arises due to the dipolar (or “stray”) field, originating as a result of the magnetisation of the ferromagnet. This stray field then interacts with the magnetisation of the ferromagnet through the Zeeman interaction. The way to fully minimise the magnetostatic energy in ferromagnets, therefore, is to form a “flux-closed” state, an example of which is shown in Figure 1.2. Realistically, the competition between the exchange and the magnetostatic interaction will lead to a domain structure somewhere between these two extremes; even more so when other phenomena are considered, such as an applied magnetic field or magneto-crystalline anisotropy, which will promote the growth of certain domains at the expense of others. An example of this compromise between the magnetostatic and exchange interactions in ferromagnets is shown in Figure 1.3; in the visualised bar magnet, an increasing exchange stiffness A (Figures 1.3b and 1.3c) leads to the magnet coming closer to a perfectly ordered antiferromagnet, whereas a lower exchange stiffness A (Figure 1.3a) leads to a vortex-like state, to help close the magnetic flux.

The magnetostatic interaction, however, is negligible for a perfectly ordered antiferromagnet, because there is no net magnetisation present in antiferromagnets and so therefore no dipolar field is created from the magnetisation. Therefore, to explain domain formation in antiferromagnets, we need to explore a different underlying mechanism. The mechanism in question is magnetoelasticity; the long-range strain/stress field acts as an analogue to the stray field produced by ferromagnets. Other works, for example [22, 40, 41], have explored this analytically,

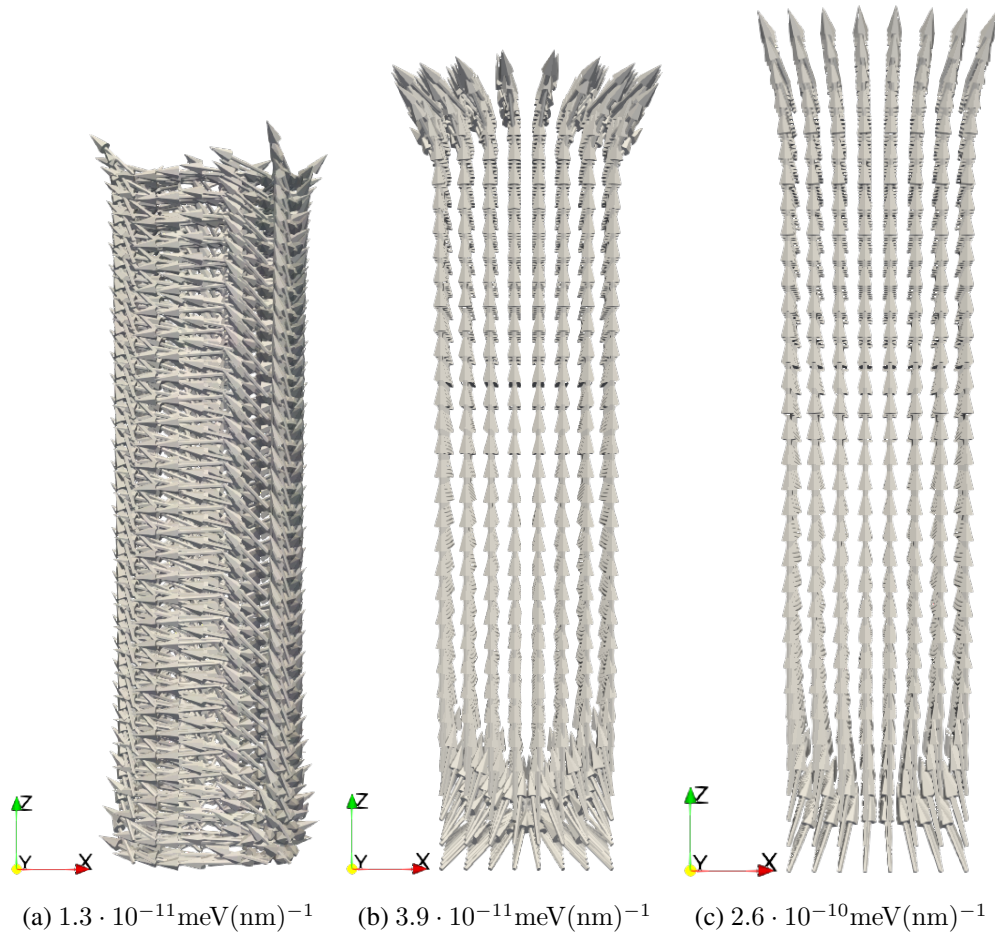


Figure 1.3: Micromagnetic simulations of an example bar ferromagnet, with varying exchange stiffness A , using the software package *mumax*³ [3], starting with the initial condition of magnetisation wholly aligned with the z -axis. The direction of the unit magnetisation vector is visualised. The values of the exchange stiffness for each simulation is given underneath each subfigure. It should be noted these simulations contain no magnetocrystalline anisotropy. Visualised using Paraview [4].

for specific sample geometries. Using our model, we wish to examine the effect of magnetoelasticity on domain dynamics at the device-level lengthscale. Work to this effect has been conducted before, specifically in [42]; our model seeks to generalise, and therefore further expand, the variety of samples and defect arrays/types within said samples that can be studied. Before we discuss our model directly, we will first examine the origin of the magnetoelastic coupling, and then give an introduction to phase field modelling.

1.3 Strain & Magnetoelasticity

1.3.1 Elastic Strain

In order for us to effectively describe the defects we will be adding our simulations to apply mechanical strain to the material, a treatment of these defects using linear elasticity theory will be prescribed, following the continuum approximation scheme laid out in [43]. When a material is deformed mechanically, inter-atomic distances are shifted. This shift in distance can be described in each instance by a displacement vector \mathbf{u} . The strain tensor components ζ_{ij} are given by the symmetric part of the displacement gradient,

$$\zeta_{ij} = \frac{1}{2} \left(\frac{\partial u_i}{\partial j} + \frac{\partial u_j}{\partial i} \right). \quad (1.6)$$

This consequently means the strain tensor is symmetric (i.e. $\zeta_{ij} = \zeta_{ji}$). The elastic energy density for this system is

$$f_{\text{el}} = \frac{1}{2} \sigma_{ij} \zeta_{ij}, \quad (1.7)$$

where $\hat{\sigma}$ is the elastic stress tensor, which is also symmetric. The corresponding stress tensor components σ_{ij} are then found using Hooke's Law,

$$\sigma_{ij} = C_{ijkl} \zeta_{kl}, \quad (1.8)$$

where C_{ijkl} is the elastic stiffness tensor, the constant of proportionality between the stress and the strain. The elastic stiffness tensor components, in turn, can be described as the second derivative of the elastic energy density f_{el} with respect to the strain tensor components,

$$C_{ijkl} = \frac{\partial^2 f_{\text{el}}}{\partial \zeta_{ij} \partial \zeta_{kl}}. \quad (1.9)$$

This elastic stiffness tensor C_{ijkl} , since its four indices represent three basis unit vectors, can then in turn have a possible 81 independent components, which is highly unwieldy. Symmetry considerations, however, can reduce this amount. Consider the symmetry of the strain and stress tensor, where $\zeta_{ij} = \zeta_{ji}$ and $\sigma_{ij} = \sigma_{ji}$. This, in turn, implies that the elastic stiffness tensor elements that contract with the strain must remain invariant under these transformations, i.e. $C_{klij} = C_{klji}$ and $C_{ijkl} = C_{jikl}$. This reduces the number of independent components to 36. Furthermore, considering Equation 1.9, George Green argued in [44] that the order of the partial derivatives doesn't matter, hence $C_{ijkl} = C_{klij}$ [43]. This second constraint limits us to having, at most, 21 independent elastic stiffness tensor components, which is the case for a triclinic crystal. This new symmetric elastic stiffness tensor can now be described using Voigt notation (recasting the matrix indices as $11 \rightarrow 1$, $22 \rightarrow 2$, $33 \rightarrow 3$, $23 \rightarrow 4$, $13 \rightarrow 5$ and $12 \rightarrow 6$) as

$$\hat{C} = \begin{bmatrix} C_{11} & C_{12} & C_{13} & C_{14} & C_{15} & C_{16} \\ C_{12} & C_{22} & C_{23} & C_{24} & C_{25} & C_{26} \\ C_{13} & C_{23} & C_{33} & C_{34} & C_{35} & C_{36} \\ C_{14} & C_{24} & C_{34} & C_{44} & C_{45} & C_{46} \\ C_{15} & C_{25} & C_{35} & C_{45} & C_{55} & C_{56} \\ C_{16} & C_{26} & C_{36} & C_{46} & C_{56} & C_{66} \end{bmatrix}. \quad (1.10)$$

The symmetry of a given crystal class can place additional restrictions on the number of independent elastic stiffness tensor components for that material [45]; how this varies between crystal class is displayed in Figure 1.4 [5], where the cubic and isotropic elastic stiffness matrices will be used extensively in this work. Having discussed the basics of linear elasticity theory and some of the important results from this, we can now discuss how it affects our magnetic system, through the magnetoelastic coupling between the elastic strain and the magnetisation of the system.

1.3.2 Magnetoelasticity

Magnetoelastic coupling is the phenomenon in which the elastic strain present inside a material couples to the magnetisation. This effect can lead to local variations in the effective anisotropy (i.e. changes to the local easy, medium and hard axes), which in turn can lead to interesting non-trivial domain patterns. To derive the mathematical form of this coupling that will be used in this work, which is for a cubic crystal class (point group $\mathbf{m3m}$) system, we will give a

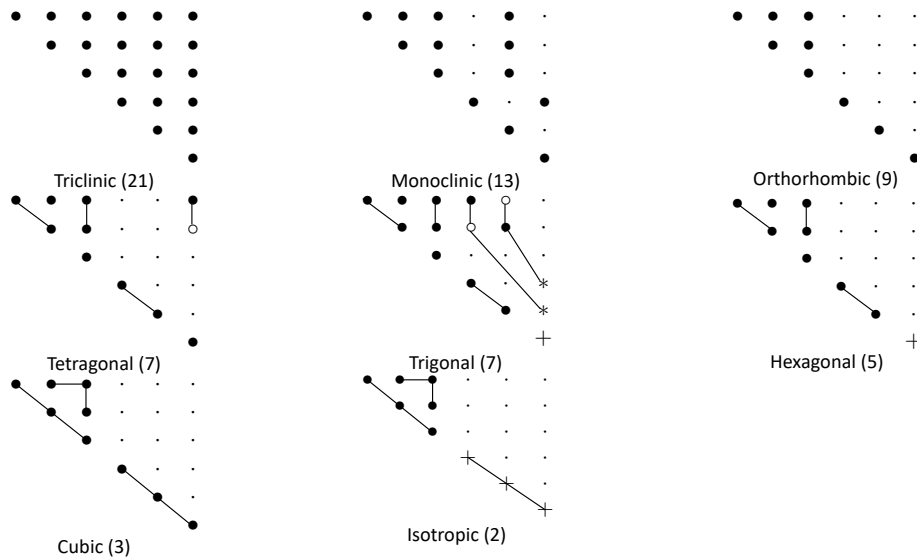


Figure 1.4: Illustration of the form of the elastic stiffness tensor in Voigt notation for different crystal classes from [5]. Only tensor components above and including the diagonal are displayed, as the others are given by previously discussed symmetry arguments. The \bullet symbols represent independent tensor components, with lines between these elements representing that they are equivalent. The \cdot symbols represent zero elements. The \circ symbols, with a line attached to a \bullet , indicate that the \circ element is equal to the negative of the \bullet element. $*$ symbols with attached lines indicate equality with the attached elements. $+$ components are the average of the top-left-most component and the component to the right (i.e. $\frac{1}{2}(C_{11} - C_{12})$), with a line between them representing equivalence between these elements.

pseudo-elastic approach, followed by a Taylor expansion approach using the magnetocrystal-line anisotropy.

Pseudo-Elastic Treatment

Firstly, we will suppose an analogy exists to the elastic stiffness tensor, called the magnetoelastic tensor \hat{B} , which has units of an energy density. We will change one of the vectors used in the elastic energy density equation, to one containing magnetisation vector components,

$$\hat{m} = \begin{bmatrix} m_x^2 \\ m_y^2 \\ m_z^2 \\ 2m_x m_y \\ 2m_x m_z \\ 2m_y m_z \end{bmatrix}, \quad (1.11)$$

representing the remaining strain vector as

$$\hat{\zeta} = \begin{bmatrix} \zeta_{xx}^2 \\ \zeta_{yy}^2 \\ \zeta_{zz}^2 \\ 2\zeta_{xy} \\ 2\zeta_{xz} \\ 2\zeta_{yz} \end{bmatrix}, \quad (1.12)$$

and let the magnetoelastic tensor possess cubic symmetry in an analogous fashion to how we described the cubic elastic stiffness tensor before (Equation 1.10), where we introduce b_0 , b_1 and b_2 , which possess units of energy density. This gives us the form of the magnetoelasticity matrix,

$$\hat{B} = \begin{bmatrix} b_0 + 2b_1 & b_0 & b_0 & 0 & 0 & 0 \\ b_0 & b_0 + 2b_1 & b_0 & 0 & 0 & 0 \\ b_0 & b_0 & b_0 + 2b_1 & 0 & 0 & 0 \\ 0 & 0 & 0 & b_2 & 0 & 0 \\ 0 & 0 & 0 & 0 & b_2 & 0 \\ 0 & 0 & 0 & 0 & 0 & b_2 \end{bmatrix}, \quad (1.13)$$

and contracting this with the strain vector $\hat{\zeta}$ and the magnetic vector \hat{m} , we can obtain the magnetoelastic energy density according to the expression

$$f_{\text{Mel}} = B_{ijkl} m_{kl} \zeta_{ij} \quad (1.14)$$

(itself analogous to the elastic energy density) we obtain the expression

$$\begin{aligned} f_{\text{Mel}} = & b_0 (\zeta_{xx} + \zeta_{yy} + \zeta_{zz}) + 2b_1 (m_x^2 \zeta_{xx} + m_y^2 \zeta_{yy} + m_z^2 \zeta_{zz}) \\ & + 4b_2 (m_x m_y \zeta_{xy} + m_x m_z \zeta_{xz} + m_y m_z \zeta_{yz}) \end{aligned} \quad (1.15)$$

using the fact that the magnetisation vector here has unit magnitude. The first term can be safely disregarded, as it is a volume changing term with no direct coupling to the magnetisation. Rescaling the constants by setting $B_0 = 2b_1$ and $B_1 = 4b_2$, we arrive at the free energy density of the magnetoelastic coupling,

$$f_{\text{Mel}} = B_0 (m_x^2 \zeta_{xx} + m_y^2 \zeta_{yy} + m_z^2 \zeta_{zz}) + 2B_1 (m_x m_y \zeta_{xy} + m_x m_z \zeta_{xz} + m_y m_z \zeta_{yz}), \quad (1.16)$$

where B_0 and B_1 are the magnetoelastic constants, in units of energy density. We can further change our constants in terms of the more widely used magnetostriction coefficients (whose forms are given in [46]),

$$\lambda_{100} = -\frac{2}{3} \frac{B_0}{(C_{11} - C_{12})}, \quad (1.17)$$

and

$$\lambda_{111} = -\frac{1}{3} \frac{B_1}{C_{44}}, \quad (1.18)$$

which are dimensionless, to give the magnetostriction energy density,

$$\begin{aligned} f_{\text{Mel}} = & -\frac{3}{2} (C_{11} - C_{12}) \lambda_{100} (m_x^2 \zeta_{xx} + m_y^2 \zeta_{yy} + m_z^2 \zeta_{zz}) \\ & - 6C_{44} \lambda_{111} (m_x m_y \zeta_{xy} + m_x m_z \zeta_{xz} + m_y m_z \zeta_{yz}). \end{aligned} \quad (1.19)$$

These magnetostriction coefficients, λ_{100} and λ_{111} , can be calculated and/or measured in different ways. On calculating these coefficients, *ab initio* calculations have been conducted in the past, for example in [47] where the collective electron model was used; however, these

values differed from those found in experiment by a not-inconsiderable margin. More recent works, for example [48], have, however, successfully reproduced experimental results, within an acceptable margin, for the magnetostriction coefficients using modern first principles calculations, in this case using the local density full potential linearised augmented plane wave method. This was enabled by using modern state tracking and torque approaches to calculate the magnetocrystalline anisotropy accurately. A widely used alternative *ab initio* calculation method is density functional theory (DFT), an example of which is [49], meaning existing software packages used for DFT calculations can be utilised for this purpose. On the measurement of these coefficients, an excellent review articles on the measurement methods available are detailed in [50]; a broad summary of this work divides the measurement techniques into two approaches; direct and indirect measurement, depending on whether the strain is measured directly, or some other parameter which relies on the strain is measured instead. The direct methods include the strain gauge methods, i.e. by varying the length (i.e. strain) of a wire the resistance increases, hence the magnetostriction coefficients may be measured, and dilatometry methods, i.e. measuring the volume change originating as a result of the magnetoelastic coupling. The indirect methods use the Villari effect, i.e. inverse Joule magnetostriction, for use in measurement. These methods include ferromagnetic resonance (FMR), measuring the shift in the ferromagnetic resonance to determine the change in permeability in the sample caused by an applied stress, small-angle magnetization rotation (SAMR), where a constant \mathbf{H} field and an alternating transverse \mathbf{H} field cause a voltage in a measuring coil around the sample, and an applied time-varying strain field leads to a voltage variation in the measuring coil, which in turn gives a measurement of the magnetoelastic coupling, and strain modulated ferromagnetic resonance (SMFMR), essentially a dynamic variation of the FMR method using an time-varying strain field. The type of method selected depends on the type of material and the accuracy required (i.e. 10^{-9} to 10^{-5} etc.). We will now look at deriving Equations 1.16 and 1.19 by considering a Taylor expansion of the magnetocrystalline anisotropy, comparing the two and discussing the final form of the magnetoelastic coupling used in this work.

Taylor Expansion Treatment

Following the directions of ([46, 51, 52]), we will express the magnetoelastic coupling as an effective perturbation of the magnetocrystalline anisotropy, after the crystal lattice undergoes some mechanical distortion. We characterise this distortion by expanding the effective magnetic anisotropy energy density of the system f_K as a MacLaurin series with respect to the

strain tensor components,

$$f_K = \left(f_k^0\right) + \left(f_k^0\right)'_{ij} \zeta_{ij} + \frac{1}{2} \left(f_k^0\right)''_{ijkl} \zeta_{ij} \zeta_{kl} + \dots, \quad (1.20)$$

where the superscript 0 indicates this object was evaluated for the undeformed lattice. The first term is our original magnetocrystalline anisotropy, without any distortion. The third term gives us a correction to the elastic energy of the system as a result of the lowered crystalline symmetry caused by the distortion [52]. The third term is small compared to the other terms, so will be ignored in this analysis. The second term describes our magnetoelastic coupling, where the magnetocrystalline anisotropy interacts with the mechanical strain. Since $\left(f_k^0\right)'_{ij}$ is a function of the magnetisation components exclusively [52], we can write it as

$$\left(\frac{\partial f_K}{\partial \zeta_{ij}}\right) = \left(f_k^0\right)'_{ij} = b_{ij} + b_{ijkl} m_k m_l + \dots \quad (1.21)$$

where we b_{ijkl} will be defined as our magnetoelastic tensor, as the tensor b_{ij} , merely contracts with the strain, and since the component of $\left(f_k^0\right)'_{ij}$ which contains this has no magnetisation terms, this has no direct coupling effect with the strain on our magnetisation hence will be ignored. Higher order terms are considered negligible in the following derivation. Given the general form of the second term displayed here, we propose the following forms of the differentials present in the Taylor expansion,

$$\frac{\partial f_K}{\partial \zeta_{ii}} = B_0 m_i m_i, \quad (1.22)$$

and, where $i \neq j$,

$$\frac{\partial f_K}{\partial \zeta_{ij}} = B_1 m_i m_j. \quad (1.23)$$

This gives, for our magnetoelastic term,

$$f_{\text{Mel}} = B_0 \left(m_x^2 \zeta_{xx} + m_y^2 \zeta_{yy} + m_z^2 \zeta_{zz}\right) + B_1 \left(m_x m_y \zeta_{xy} + m_y m_x \zeta_{yx} + m_x m_z \zeta_{xz} + m_z m_x \zeta_{zx} + m_y m_z \zeta_{yz} + m_z m_y \zeta_{zy}\right), \quad (1.24)$$

and using that our strain tensor is symmetric, $m_i m_j \zeta_{ij} = m_j m_i \zeta_{ji}$, so the final form of the magnetoelastic energy density for a cubic crystal becomes

$$f_{\text{Mel}} = B_0 \left(m_x^2 \zeta_{xx} + m_y^2 \zeta_{yy} + m_z^2 \zeta_{zz}\right) + 2B_1 \left(m_x m_y \zeta_{xy} + m_x m_z \zeta_{xz} + m_y m_z \zeta_{yz}\right). \quad (1.25)$$

We can clearly see that for these approaches to be equivalent, Equations 1.16 and 1.25 must be equal hence $2b_1 = B_0$ and $4b_2 = 2B_1$, and $b_0 = 0$ (we can set this to be so because here we are not interested in what is a purely volumetric strain term). The reason we have derived this magnetoelastic energy twice using different means was to demonstrate that the magnetoelastic coupling arises from the nuanced relation that the mechanical strain of the lattice has to the magnetocrystalline anisotropy. This was shown by showing that applying an elasticity-style tensor to a combination of magnetic and strain terms could indeed give a coupling between these variables; an expansion of the magnetocrystalline anisotropy and logical symmetry arguments then confirms the form of this coupling and gives a more suitable redefinition of the previously used constants, and by arriving at the same form for both approaches, we furthermore confirm the link between the elastic strain and the magnetic anisotropy. For us to examine the effect of this coupling at the device level lengthscale (mm– to μm –), we then looked at realistic defects which occur in antiferromagnetic materials to provide us with realistic strain fields, which would be practical to implement in a numerical model. These conditions led us to the selection of inclusion defects and crystalline dislocations (which both have verified precedence in influencing magnetic behaviour, for example in [53]) as vehicles to provide a meaningful test of the effect of the magnetoelastic coupling.

1.4 Dislocations and Defects: A Brief Overview

For us to investigate the effect of strain in antiferromagnets, we need to produce the necessary strain fields inside the material. Whilst mechanical strain is present in all real materials, and hence will affect the magnetic domain structure of antiferromagnets, for our model we sought to define strain fields that were calculable and that had a realistic origin. These criteria led us to look at crystalline defects and dislocations, a realistic source of strain in real crystalline materials and these strain fields are calculable by elastic strain theory. We will start the discussion on these objects with the simplest case, where there exists an analytical solution. This case, named after the postulator and solver, applied mathematician John Eshelby, is called the Eshelby Inclusion, where an ill-fitting section of otherwise homogeneous material, and its interaction with the surrounding material, is considered. We shall not repeat the derivation given by Eshelby (shown in the original paper [54]), but rather give the key arguments, with the assistance of [43] following the original paper, and quote the result for an elliptical inclusion, as by assuming this, the stress inside the inclusion is uniform.

1.4.1 Eshelby Inclusion

Firstly, we will remove the ill-fitting inclusion from the surrounding material, which for this derivation, importantly, we will assume extends to infinity and is homogeneous. We then allow the inclusion to relax elastically, by undergoing a stress-free strain. During this process, the stress inside the inclusion and the (previously) surrounding material is zero. We then return the inclusion to its original shape by applying surface tractions $-\sigma_{ij}^T n_j$, where σ_{ij}^T is the transformation stress given by applying Hooke's Law to the strain we applied earlier, and n_j is the j^{th} component of the surface normal. We then reattach and seal the inclusion to the previously surrounding material. These surface tractions give a body force, applied along the surface between the inclusion and the surrounding material. We then have to annihilate (to reach a steady state) these surface tractions by applying equal and opposite surface tractions $+\sigma_{ij}^T n_j$ which, in turn, will give the "constrained" displacements present throughout both the inclusion defect and the rest of the material [43]. A diagram of this situation is shown in Figure 1.5.

Using Green's functions, and using the symmetry of the stress tensor σ , the constrained displacement u_i^C can be described as

$$u_i^C(\mathbf{r}) = \frac{\sigma_{jk}^T}{16\pi\mu(1-\nu)} \int_{\mathbb{R}} \frac{1}{\|\mathbf{r} - \mathbf{r}'\|^2} \left((1-2\nu)(\rho_k\delta_{ij} + \rho_j\delta_{ik}) - \rho_i\delta_{jk} + 3\rho_i\rho_j\rho_k \right) dV, \quad (1.26)$$

where ρ_a is the direction cosine along the a^{th} direction, ν is Poisson's ratio (equivalent to $0.5 \cdot (C_{11} + 2C_{12} - 2C_{44}) / (C_{11} + 2C_{12} + C_{44})$ for a cubic or isotropic system, giving maximal and minimal values of 0.5 and -1 respectively) and μ is the shear modulus (equivalent to C_{44} for a cubic or isotropic system). By converting the integrand to a series of infinitesimal cones (and therefore the integrand from volume to solid angle subtended by the cone base, ω) and using Hooke's Law to convert the transformation stress to strain, the constrained strain ζ_{ij}^C can be derived,

$$\zeta_{ij}^C = \frac{\zeta_{jk}^T}{16\pi(1-\nu)} \int \frac{\lambda_i g_{ijk} + \lambda_l g_{ljk}}{g} d\omega, \quad (1.27)$$

where ζ_{jk}^T is the transformation strain, λ_a is the a^{th} component of the vector $(\rho_1 a_1^{-2}, \rho_2 a_2^{-2}, \rho_3 a_3^{-2})$, g is result of $(\rho_1 a_1^{-2} + \rho_2 a_2^{-2} + \rho_3 a_3^{-2})$ and g_{ijk} is $\left((1-2\nu)(\rho_k\delta_{ij} + \rho_j\delta_{ik} - \rho_i\delta_{jk}) + 3\rho_i\rho_j\rho_k \right)$. This expression can be simplified as follows,

Figure 1.5: Diagram describing the Eshelby inclusion analysis. Part a) shows the initial ill-fitting material (inclusion) and its surrounding material (the matrix). Part b) then shows the inclusion being removed, and being allowed to expand under a "stress-free" strain (the eigen-strain). Part c) shows the application of tractions T_i to the now-expanded inclusion back to its original shape. Finally, part d) shows the inclusion being re-inserted back into the material, where a "cancelling" force F_i , applied to surface S_{Inc} (the surface exposed after the inclusion was removed), is applied to cancel the tractions used to return the inclusion to its original state, allowing the calculation of the strain field in the material. Adapted from [6].

$$\zeta_{ij}^C = S_{ijkl}\zeta_{kl}^T, \quad (1.28)$$

by introducing S_{ijkl} , the Eshelby tensor,

$$S_{ijkl} = \frac{1}{16\pi(1-\nu)} \int \frac{\lambda_i g_{ijk} + \lambda_l g_{ijk}}{g} d\omega. \quad (1.29)$$

Being able to express the constrained strain components in this way, means that if we know the transformation strain (an eigenstrain) we can express the strain in the surrounding material and inside the inclusion. This means that we can derive an analytic solution for this inclusion defect, which can be compared to the solution we derive from our model, to verify that our numerical calculations conducted in Chapter 3 are correct. We can also explore the effect of another type of defect, crystalline dislocations, which we will detail in the following.

1.4.2 Crystalline Dislocations

Dislocations occur when an atomic plane “slips” over another, over a finite region [55]. We can describe the magnitude and direction of the displacement of the “slipped” plane, with respect to the atomic plane beneath, with the Burgers vector \mathbf{b} . The complete derivation of the stress/strain fields of these objects is beyond the scope of this work; however, like with the Eshelby Inclusion subsection, we will quote the relevant results from [43], and adapt these to the situations we wish to explore. Starting with Mura’s formula,

$$u_{a,b}(\mathbf{x}) = \zeta_{rlb} C_{ijkl} b_k \oint_{L'} G_{ja,i'}(\mathbf{x} - \mathbf{x}') dx_{r'} \quad (1.30)$$

for the distortion tensor of a dislocation, we can apply Hooke’s Law to get the stress field,

$$\sigma_{ab}(\mathbf{x}) = C_{abij} \frac{\zeta_{rmj} b_k}{8\pi(1-\nu)} \oint_{L'} \left[(1-2\nu) \frac{\delta_{ki} X_m + \delta_{mi} X_k - \delta_{km} X_i}{X^3} + 3 \frac{X_k X_m X_i}{X^5} \right] dx_{r'} \quad (1.31)$$

where we define \mathbf{X} as $\mathbf{x} - \mathbf{x}'$, and $X = |\mathbf{X}|$. We can simplify this by recasting the indices and defining the line integral I_{ijkl} as

$$I_{ijkl} = \oint_{L'} \left[(1-2\nu) \frac{\delta_{ij} X_k + \delta_{kj} X_i - \delta_{ik} X_j}{X^3} + 3 \frac{X_i X_k X_j}{X^5} \right] dx_{l'}, \quad (1.32)$$

such that Equation 1.31 becomes

$$\sigma_{ab}(\mathbf{x}) = \frac{\mu b_i}{8\pi(1-\nu)} \left[\frac{2\nu}{1-\nu} \delta_{ab} \zeta_{lkj} I_{ijkl} + \zeta_{lkb} I_{iakl} + \zeta_{lka} I_{ibkl} \right]. \quad (1.33)$$

To proceed further, we will need to make assumptions about the Burgers vector and the dislocation line, which will lead us to defining two specific types of crystalline dislocations as follows.

Edge Dislocations

If the dislocation line and the Burgers vector are perpendicular, we will get an edge dislocation. An edge dislocation occurs when a half-plane of atoms is added (removed) to (from) a crystalline lattice, imparting a strain into the material. If we assume we have an infinite dislocation along the z -axis, and that our Burgers vector is $\mathbf{b} = [0, b, 0]$ (which is consistent with our definition of an edge dislocation), then we can arrive at the stress tensor components by working through the following (only the working for the first stress tensor component, σ_{11} , will be shown; the rest follow by similar logic): we initially start with the full expression for the first stress tensor component,

$$\begin{aligned} \sigma_{11} = \frac{\mu b}{8\pi(1-\nu)} \left[\frac{2\nu}{1-2\nu} (\zeta_{123} I_{2321} + \zeta_{231} I_{2132} + \zeta_{312} I_{2213} + \zeta_{321} I_{2123} + \zeta_{132} I_{2231} + \zeta_{213} I_{2312}) \right] \\ + \frac{\mu b}{8\pi(1-\nu)} [\zeta_{231} I_{2132} + \zeta_{321} I_{2123} + \zeta_{231} I_{2132} + \zeta_{321} I_{2123}], \end{aligned} \quad (1.34)$$

where, because the integral occurs over the dislocation line, which here is the z -axis, integrals over x' and y' evaluate to zero as the upper and lower limits are identical (i.e. zero). This means the only non-zero terms left in the expression are

$$\sigma_{11} = \frac{\mu b}{8\pi(1-\nu)} \left[\frac{2\nu}{1-2\nu} (I_{2213} - I_{2123}) - 2I_{2123} \right]. \quad (1.35)$$

We can then evaluate these integrals,

$$I_{2213} = \int_{-\infty}^{\infty} \left[(1-2\nu) \frac{x}{(x^2 + y^2 + (z')^2)^{\frac{3}{2}}} + 3 \frac{xy^2}{(x^2 + y^2 + (z')^2)^{\frac{5}{2}}} \right] dz' \quad (1.36)$$

and

$$I_{2123} = \int_{-\infty}^{\infty} \left[(1 - 2\nu) \frac{-x}{(x^2 + y^2 + (z')^2)^{\frac{3}{2}}} + 3 \frac{xy^2}{(x^2 + y^2 + (z')^2)^{\frac{5}{2}}} \right] dz' \quad (1.37)$$

to get

$$I_{2213} = (1 - 2\nu) \frac{2x}{x^2 + y^2} + \frac{4xy^2}{(x^2 + y^2)^2} \quad (1.38)$$

and

$$I_{2123} = -(1 - 2\nu) \frac{2x}{x^2 + y^2} + \frac{4xy^2}{(x^2 + y^2)^2}. \quad (1.39)$$

We can then insert these evaluated integrals into Equation 1.35 to achieve the final form of the 11 component of the stress tensor,

$$\sigma_{11} = \frac{\mu bx}{2\pi(1 - \nu)} \left[\frac{x^2 - y^2}{(x^2 + y^2)^2} \right]. \quad (1.40)$$

The other non-zero stress tensor components ($\sigma_{13} = \sigma_{31} = 0 = \sigma_{23} = \sigma_{32}$) can then be calculated as

$$\sigma_{12} = \sigma_{21} = \frac{\mu by}{2\pi(1 - \nu)} \left[\frac{x^2 - y^2}{(x^2 + y^2)^2} \right], \quad (1.41)$$

$$\sigma_{22} = \frac{\mu bx}{2\pi(1 - \nu)} \left[\frac{x^2 + 3y^2}{(x^2 + y^2)^2} \right], \quad (1.42)$$

$$\sigma_{33} = \frac{\mu bx\nu}{\pi(1 - \nu)(x^2 + y^2)} = \nu(\sigma_{11} + \sigma_{22}). \quad (1.43)$$

To give an example of what these terms look like, we visualise these both in MOOSE (in the format that we will be using in our phase field model) in Figure 1.6, and using the software package Atomsk [8] in Figure 1.7 to give an impression of the effect that an edge dislocation has at the atomic level. Furthermore, we can deduce from Hooke's Law the corresponding strain tensor components (since the form of the stress tensor implies a plane strain formalism, this in turn restricts $\zeta_{33} = 0$),

$$\zeta_{11} = \frac{bx}{4\pi(1 - \nu)} \left[\frac{x^2(1 - 2\nu) - y^2(2\nu + 1)}{(x^2 + y^2)^2} \right], \quad (1.44)$$

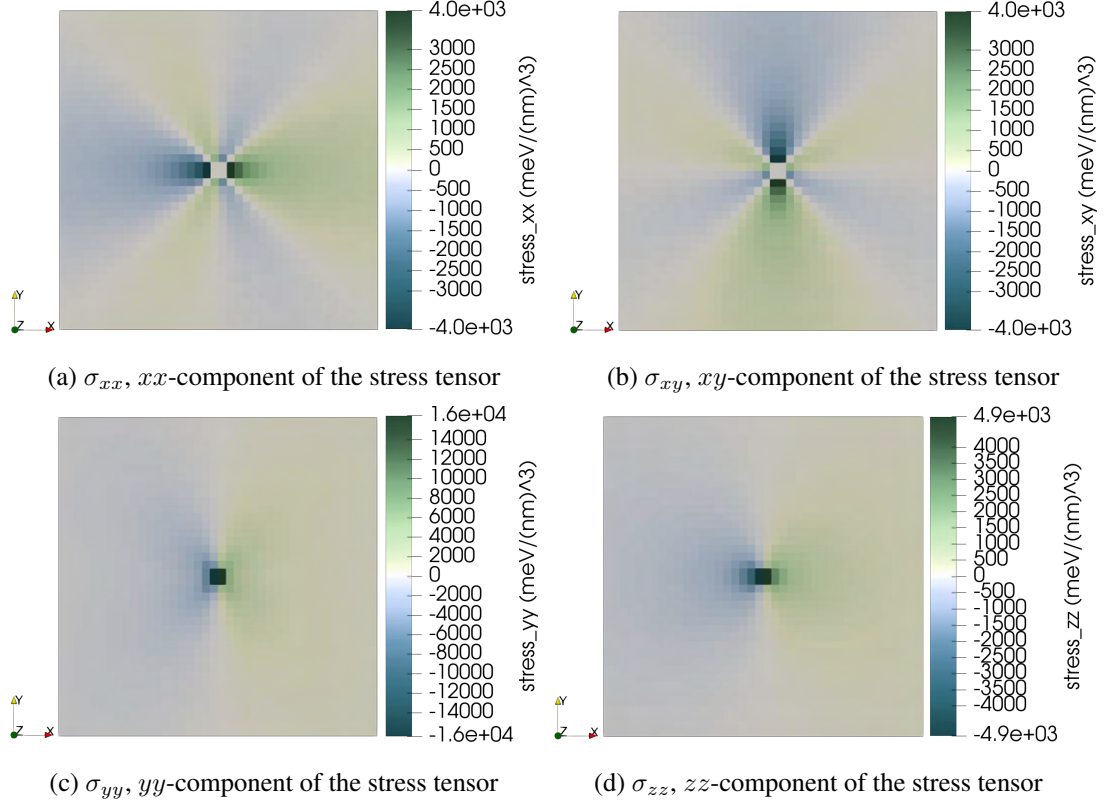


Figure 1.6: Stress tensor components resulting from an edge dislocation along the z -axis, with Burgers vector $\mathbf{b} = [0, 0.419, 0]$, implemented via initial conditions in MOOSE [7]. Visualised using Paraview [4].

$$\zeta_{12} = \zeta_{21} = \frac{by}{4\pi(1-\nu)} \left[\frac{x^2 - y^2}{(x^2 + y^2)^2} \right], \quad (1.45)$$

$$\zeta_{22} = \frac{bx}{4\pi(1-\nu)} \left[\frac{x^2(1-2\nu) + y^2(3-2\nu)}{(x^2 + y^2)^2} \right]. \quad (1.46)$$

We can now use the process described above to derive the stress tensor components for another type of dislocation; the screw dislocation.

Screw Dislocations

If the dislocation line and the Burgers vector are parallel, the configuration we arrive at is known as a “screw”-type dislocation or, more commonly, a screw dislocation, a scenario ori-

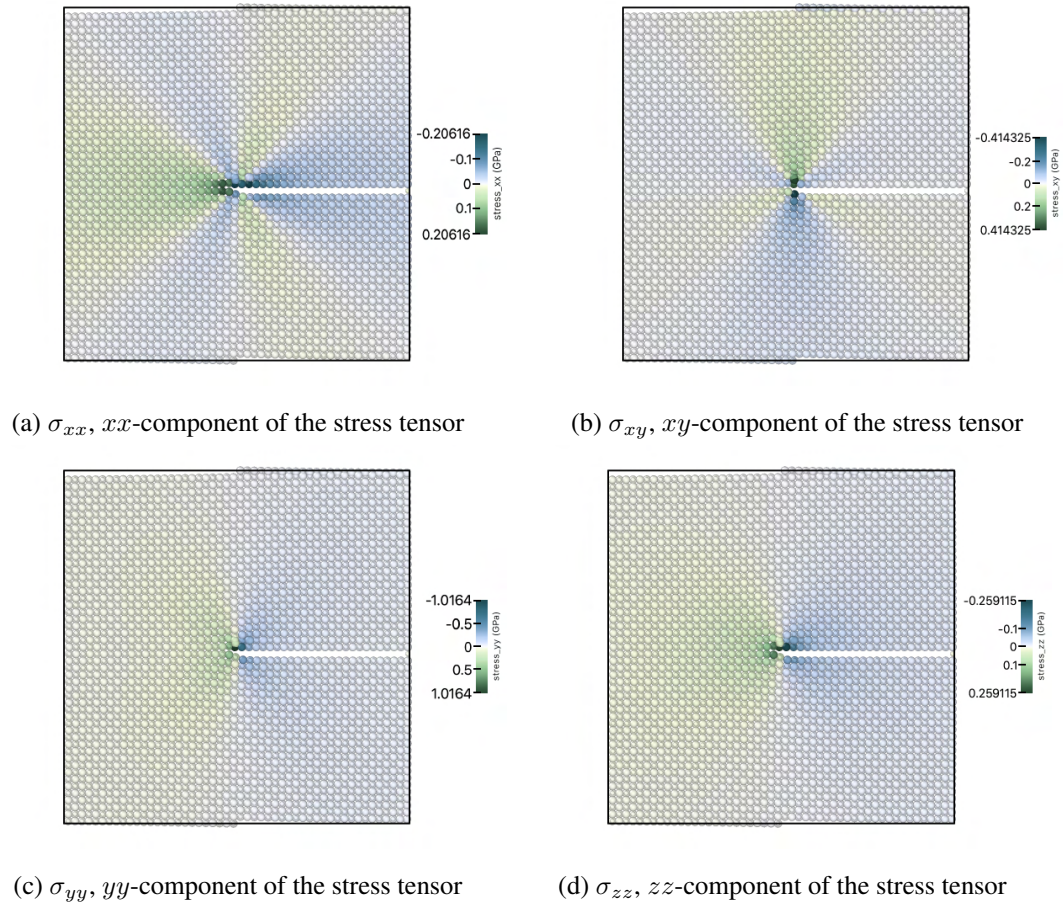


Figure 1.7: Stress tensor components resulting from an edge dislocation along the z -axis, with Burgers vector $\mathbf{b} = [0, 4.19, 0]$ (in units of \AA). As a contrast to Figure 1.6, these components are shown using a discrete, atomic supercell (where we visualise the top face) using the software package AtomsK [8], and therefore the atomic displacements resulting from the insertion of the half-plane of atoms are easily discernible. Visualised using OVITO [9].

ginally proposed by J. M. Burgers [56]. The reason for the name can be alluded to in Figure 1.10; the effect of the dislocation is to make the surface look like a section of a screw. If we assume that we have an infinite dislocation along the y -axis, and that Burgers vector is $\mathbf{b} = [0, b, 0]$ (which is consistent with our definition of a screw dislocation), we arrive at the following non-zero stress tensor components ($\sigma_{11} = \sigma_{22} = \sigma_{33} = 0 = \sigma_{13} = \sigma_{31}$), following the same method we deployed for the edge dislocation case:

$$\sigma_{12} = \sigma_{21} = \frac{\mu b z}{2\pi (x^2 + z^2)}, \quad (1.47)$$

$$\sigma_{23} = \sigma_{32} = -\frac{\mu b x}{2\pi (x^2 + z^2)}. \quad (1.48)$$

We can then visualise these stress tensor components in a similar fashion as we did for the edge dislocation, using MOOSE (Figure 1.8) and Atomsk (Figure 1.9), with Figure 1.10 being a zoomed-in view of Figure 1.9b to more clearly demonstrate the effect of the screw dislocation at the atomic level with respect to atomic displacements. We can again use Hooke's Law to derive the related strain tensor components,

$$\zeta_{12} = \zeta_{21} = \frac{b z}{4\pi (x^2 + z^2)}, \quad (1.49)$$

$$\zeta_{23} = \zeta_{32} = -\frac{b x}{4\pi (x^2 + z^2)}. \quad (1.50)$$

These stresses and strains, from both edge and screw dislocations, will be used in a later section of this work to examine their effect on the magnetic structure of materials with a significant magnetoelastic coupling. We will now discuss how we developed our model, with reference to specific kernels (and other features) specifically created during the course of this work, as well as repurposed functionalities already present in the MOOSE software [7].

1.5 Introduction to Phase Field Modelling

Phase field modelling is a method which solves the evolution of order parameters, so as to minimise the overall free energy density of the system. We define an order parameter as a field present throughout the material, the value of which describes the state present at that point, for example in a phase change, a value of 0 describes a state consisting entirely of one phase whereas a value of 1 describes a state consisting entirely of another phase. We make

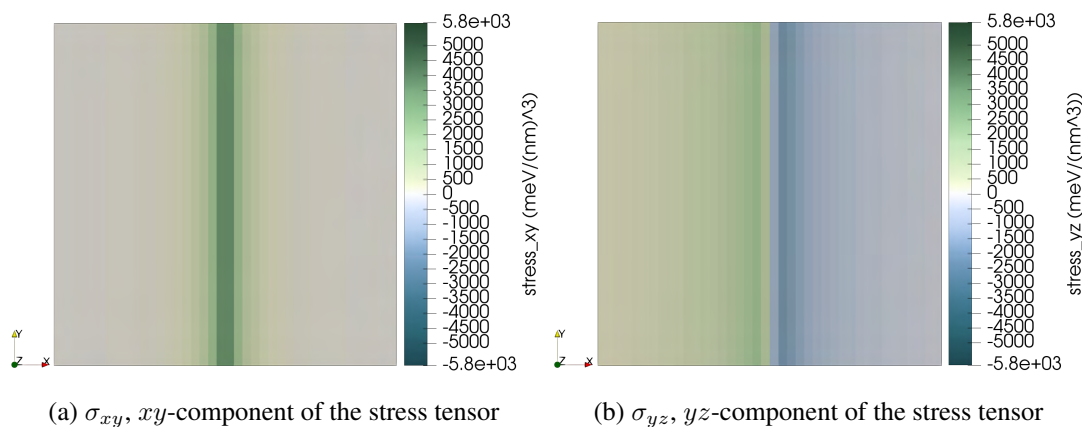


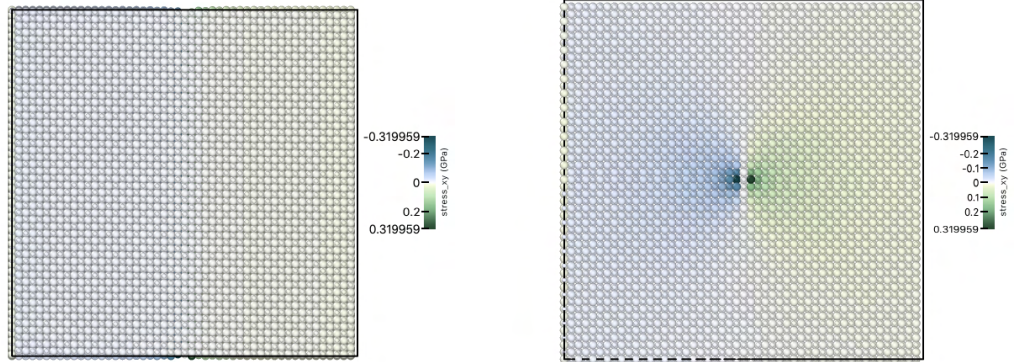
Figure 1.8: Stress tensor components resulting from a screw dislocation along the y -axis, with Burgers vector $\mathbf{b} = [0, 0.419, 0]$, implemented via initial conditions in MOOSE [7]. Note the absence of the σ_{11} , σ_{22} and σ_{33} as these terms are equal to zero, a key feature of screw dislocations. Visualised using Paraview [4].

an important assumption that the order parameter varies smoothly throughout the material. The phase field method has already been employed successfully to explore multiple areas of physics, for example spinodal decomposition [57], grain growth [58], and crack nucleation and expansion in solid oxide cells [59] amongst others. We will explore the use of the phase field method in spinodal decomposition, as this will give context to why we are using this for our investigation, before returning to the discussion about using this method on magnetic materials.

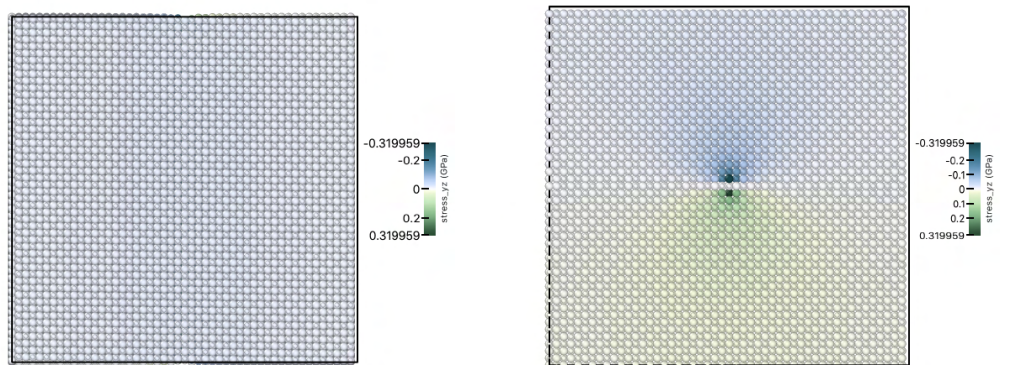
Spinodal decomposition occurs when a mixed-composition alloy breaks down into separate regions of material with a uniform composition. By describing regions of material being rich in one element as one phase and regions being rich in another element as being another phase, this becomes a situation where using a phase field model would be highly effective. Evolving under the Cahn-Hilliard regime (so as to preserve the overall amount of material present in the sample), with Cahn-Hilliard equation,

$$\frac{\partial c}{\partial t} = \nabla \cdot L \nabla \frac{\delta F}{\delta c}, \quad (1.51)$$

with appropriate initial conditions and free energy functional, we can achieve the steady state of the system where the decomposition has taken place. In Equation 1.51, c is a conserved order parameter (dimensionless), L is the mobility (in units of volume over the product of energy and time), F is the free energy functional (in units of energy), and t is (abstract) time (in units



(a) σ_{xy} , xy -component of the stress tensor, viewed from the top (b) σ_{xy} , xy -component of the stress tensor, viewed from the front



(c) σ_{yz} , yz -component of the stress tensor, viewed from the top (d) σ_{yz} , yz -component of the stress tensor, viewed from the front

Figure 1.9: Top and front faces of the crystalline lattice featuring a screw dislocation, with the dislocation line along the y -axis and the z -axis being the axis perpendicular to the dislocation line along which displaced atoms are allowed to move to relax the system. The magnitude of the Burgers vector is 4.19\AA . The xy and yz -components of stress are visualised (qualitatively) using a colour map (shown next to the lattice, where the blue regions indicate a negative component and green regions indicate a positive component). Created with AtomsK [8] and visualised using OVITO [9].



Figure 1.10: Perspective view of the front-face of the crystalline lattice with the screw dislocation shown in Figure 1.9. Created with Atomsk [8] and visualised using OVITO [9].

of time); this “abstract time” represents the evolution of the simulation towards convergence rather than any tangible variable (we will describe what we mean by abstract time in a later discussion). By using the phase field model in this way, we can get some idea of how the system would evolve under this phase change, and have a final steady state result which can be compared to experimental results. This model can be generalised to other materials which undergo this phase change (i.e. by shifting initial conditions and the free energy environment). This is an example of why phase field modelling is a highly effective modelling technique which can be applied to different scenarios and still produce results comparable to experiment. We will now look at how to apply this to a magnetic system in general, then specialise to discuss how it will be applied to our system specifically.

For a magnetic system, we describe the components of the magnetisation vector (itself a bulk descriptor of the collection of magnetic moments per volume) as non-conserved order parameters which contribute to the free energy of the system through terms such as the magnetocrystalline anisotropy and the magnetic exchange. This approach can be thought of as a numerical application of Landau Theory [60]; this will be explored further on in this section.

In our model the distribution of the non-conserved order parameters is found by minimising the free energy of the system towards a steady state via the Allen-Cahn [61] equation,

$$\frac{\partial m_i}{\partial t} = -L_i \frac{\delta F}{\delta m_i}, \quad (1.52)$$

where m_i is a non-conserved order parameter (dimensionless), L_i is the mobility (in units of volume over the product of energy and time) and F is the free energy functional (in units of energy), and t is (abstract) time (in units of time); so, similar to the Cahn-Hilliard system, this “time” represents the evolution of the simulation towards convergence. We use this description of “abstract time” for the purposes of generality; the Allen-Cahn equation ignores momenta and inertia, so whilst for some regimes this may be a good approximation, in which case evolution in this model will describe the dynamics of the system within approximation (and so

this “abstract time” ceases to be “abstract”), in general it is not and the true dynamics are not recovered under evolution in this model, but the local energy minimum of the system is always recovered, which is what we are interested in in this work. As a brief aside, this means we do not have to solve precessional dynamics, i.e. we do not solve the Landau-Lifshitz-Gilbert equation (commonly abbreviated to LLG),

$$\frac{\partial \mathbf{M}}{\partial t} = \frac{|\gamma|}{1 + \alpha^2} \left(\mathbf{H}_{\text{Eff}} \times \mathbf{M} + \alpha \frac{\mathbf{M}}{|\mathbf{M}|} \times (\mathbf{H}_{\text{Eff}} \times \mathbf{M}) \right), \quad (1.53)$$

which describes the evolution of the microscopic magnetisation \mathbf{M} for a ferromagnet, with gyromagnetic factor γ and damping coefficient α , below the Curie temperature (where the ferromagnetic ordering breaks down), by describing the environment of the magnetisation by an effective magnetic field \mathbf{H}_{Eff} ; an example of a numeric scheme to solve this equation is given in [62]. We do not have to solve the precessional dynamics as we are only interested in the lowest energy state of the system, and we are only conducting an energy minimisation.

Returning to Equation 1.52, $\nabla \cdot$ is the divergence operator, and ∇ is the gradient operator; the δ symbols on the numerator and denominator mean this is a functional derivative. The state of the system which is in the minimal free energy state is given by the Euler-Lagrange equations for the system,

$$\frac{\delta f}{\delta m_i} - \nabla \cdot \frac{\delta f}{\delta \nabla m_i} = 0, \quad (1.54)$$

where f is the free energy density function. The Allen-Cahn equation gives a method for us to approach this configuration, i.e. by repeated application of the Allen-Cahn method, where we evolve m_i in time so as to minimise the free energy of the system, we will arrive at a state described by

$$\frac{\delta f}{\delta m_i} - \nabla \cdot \frac{\delta f}{\delta \nabla m_i} = k, \quad (1.55)$$

where k is the convergence tolerance of our simulation. As k tends towards zero, it can be seen that we would recover the Euler-Lagrange relations. However, this inevitably would entail a perfect simulation which in turn would require an infinitely decreasing timestep and an infinite amount of computation time. Thus, we have to settle for an approximation where we set k to give us the best compromise between computational expense and precision of the resulting solution.

The difference between the Equations (1.52) and (1.51) is that the Allen-Cahn equation acts on

non-preserved order parameters, whereas the Cahn-Hilliard equation acts on conserved order parameters. This quality of the Cahn-Hilliard equation means it is particularly useful in situations where we wish to look at a closed system where there is no flux of the phase out of the system, i.e. like in the spinodal decomposition scenario mentioned before.

Since our magnetisation vector components cannot be conserved (so that they may be allowed to exchange between themselves, i.e. that the x -component of a vector may grow at the expense of the y -component) for our model to work, we will be working exclusively with the Allen-Cahn Equation, Equation (1.52). To give an example of how the Phase Field model works in practice, and its basis in Landau Theory, let us look at an example case. Using the Landau Theory approach [60], we assume that we can write the free energy density of a spatially uniform system, f_{sys} , as a power series in the order parameter η with a series of coefficients, i.e.

$$f_{\text{sys}} = \sum_{n=0}^{\infty} k(n)\eta^n. \quad (1.56)$$

Specifically this is only true around a certain temperature T_c i.e. the system cannot start directly on a critical point. The Landau formalism then explicitly states that the equilibrium state of our system is given by finding the minimum of f_{sys} with respect to η , in a fashion reminiscent of the Phase Field method, highlighting the similarity between the two. Taking this power series and truncating at the quadratic η^2 term, we can write our free energy density as

$$f_{\text{sys}} = a\eta^2 + b\eta + c, \quad (1.57)$$

for some $a, b, c \in \mathbb{R}$. Applying the Allen-Cahn Equation (1.52) to this, we achieve

$$\frac{\partial \eta}{\partial t} = -(2a\eta + b) \quad (1.58)$$

after setting the mobility L_i to unity. Setting $a = 1$, $b = 2$, and $c = 1$, where the resulting free energy is given by $\eta^2 + 2\eta + 1$, we can clearly see that this free energy is minimal when $\eta = -1$. Plotting (1.58) for this scenario in Figure 1.11, it can be observed that the steady-state solution (i.e. where η is not evolving) is achieved at $\eta = -1$ as expected, and the model will evolve the system towards this state. In this way, the Phase Field model can be thought of as “rolling a variable down a hill” with respect to the free energy landscape to arrive at the equilibrium solution, showing this to be an application of the Landau Theory formalism.

In the context of our magnetic model, let us now consider the example of the Zeeman energy, the free energy of the interaction of magnetic material with an applied magnetic field,

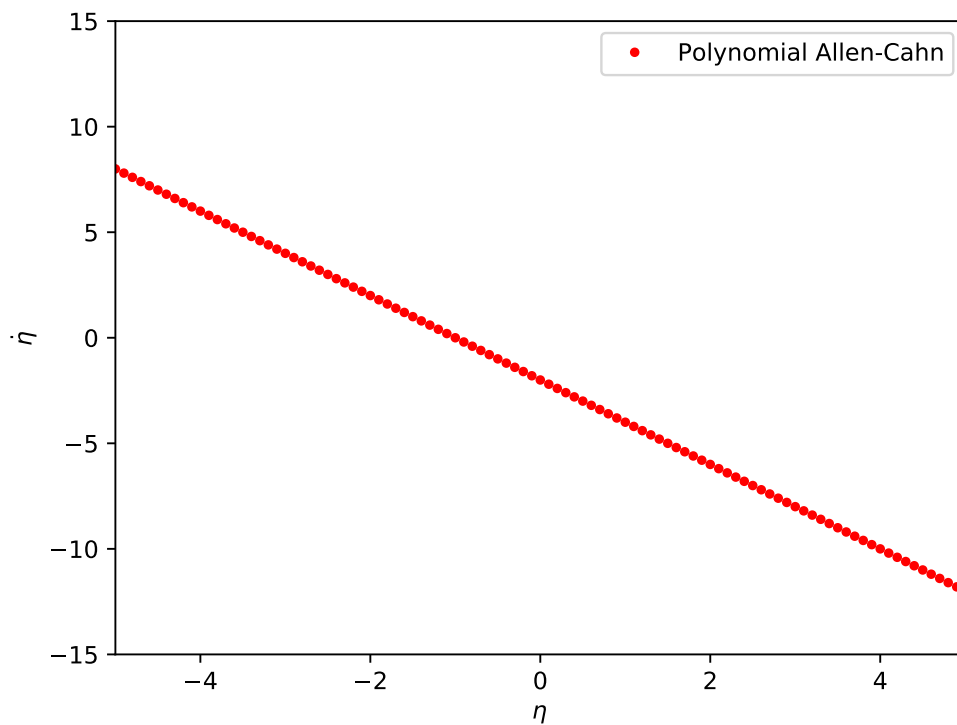


Figure 1.11: $\dot{\eta}$ with respect to η calculated by the input of the polynomial free energy system into the Allen-Cahn Equation (1.52). Note that $\dot{\eta}$ is only zero at $\eta = -1$, and has opposite sign on either side of this point, showing that the system will relax to the $\eta = -1$ point.

and find the effect this has on the components of the unit magnetisation vector. The free energy density of this effect is represented simply by

$$f_{\text{Zeeman}} = -\mu_0 \mathbf{H} \cdot \mathbf{M}, \quad (1.59)$$

where \mathbf{H} is the applied magnetic field vector ($\text{A}(\text{nm})^{-1}$), μ_0 is the permeability of free space ($\text{meV}(\text{nm})^{-1}\text{A}^{-2}$), and \mathbf{M} is the magnetisation of our material ($\text{A}(\text{nm})^{-1}$). Note that the magnetisation vector components can be represented in terms of their unit magnetisation vector counterparts by $M_i = M_s m_i$, where M_s is the saturation magnetisation in units of ($\text{A}(\text{nm})^{-1}$). Since our free energy density functional here only depends explicitly on m_i and not its time derivatives, its functional derivative takes the form of

$$\frac{\delta f_{\text{Zeeman}}}{\delta m_i} = \frac{\partial f_{\text{Zeeman}}}{\partial m_i} = -\mu_0 H_i, \quad (1.60)$$

and inserting this into the Allen-Cahn Equation (1.52) gives

$$\frac{\partial m_i}{\partial t} = \mu_0 H_i \quad (1.61)$$

assuming our mobility is unity, so our the evolution of our magnetisation unit vector component does not depend on the component itself, only on the corresponding component of the applied magnetic field. Using an example applied field of $\mathbf{H} = (0, 0, H_0)$, $H_0 > 0$, in Cartesian coordinates, we can see that the x, y components of magnetisation will not evolve under the influence of the Zeeman energy alone (although they should evolve indirectly to preserve the magnitude of the unit vector), and the z component will increase in value. This will result in the alignment of the magnetisation in the direction of the applied field, which is the expected outcome. A similar method can be applied to other magnetic phenomena, such as magnetic exchange, magnetocrystalline anisotropy, and (assuming the stress, strain and elasticity tensors are calculated correctly) magnetoelasticity, showing that we can successfully build up a working model of an antiferromagnet under applied strain using a phase field model. Of particular importance is the use of this method to constrain our magnetisation to be a unit vector.

As alluded to when the Zeeman energy was discussed, certain free energy terms, the Zeeman term included, will seek to continually increase/decrease the magnitude of the magnetisation vector as well as change its orientation. We wish to keep our magnetisation vector as a (dimensionless) unit vector (i.e. $\mathbf{m} = \frac{\mathbf{M}}{M_s}$, where \mathbf{m} is the unit magnetisation vector (dimensionless) and \mathbf{M}, M_s are the magnetisation vector and the saturation magnetisation respectively, both

in units of $(\text{A}(\text{nm})^{-1})$. To do this, we add a free energy density term into the model as a constraint,

$$f_{\text{Norm}} = \lambda \left(1 - \sqrt{m_x^2 + m_y^2 + m_z^2} \right)^2, \quad (1.62)$$

where λ is some parameter with units of energy density $(\text{meV}(\text{nm})^{-3})$ and the other symbols retain their previous definitions. We then evolve this with the Allen-Cahn Equation (1.52) to give

$$\frac{\partial m_x}{\partial t} = \frac{-2\lambda m_x \left(1 - \sqrt{m_x^2 + m_y^2 + m_z^2} \right)^2}{\sqrt{m_x^2 + m_y^2 + m_z^2}}, \quad (1.63)$$

where this follows for the other unit magnetisation vector components (m_y, m_z) . Thus the Phase Field model will evolve the unit magnetisation vector components in order to minimise the term inside the brackets (if the system trivially sets m_x, m_y, m_z to zero, this will result in the system tending towards 0/0 and hence numerical instability) and hence will enforce our constraint, where λ sets the “strength” of our constraint.

Summary

- We have laid out our motivation, which describes the context and objectives of our work.
- The quantum origin of ferromagnetic and antiferromagnetic exchange is discussed in brief, with the phenomenon of magnetocrystalline anisotropy also being discussed.
- Magnetic domains are defined, and we use simulation results to demonstrate the role magnetostatics have in forming and stabilising single domains in ferromagnetic materials.
- We outline the framework of linear elasticity theory, which will be used throughout this work.
- We derive the magnetoelastic coupling by two separate methods, a pseudo-elastic approach and a Taylor expansion method of the magnetocrystalline anisotropy. Given these arrive at the same results (within a coefficient shift), the veracity of this derivation is reinforced.
- We use linear elasticity theory to describe the strain and stress fields of Eshelby inclusion defects and crystalline dislocations (of edge and screw types).
- The mechanics and theoretical underpinnings of our phase field model are detailed, via its basis within Landau Theory. We also give specific examples of how the phase field model is used in this work.

CHAPTER 2

Development of MESMER

In the development of our software application, MESMER, it was prudent to make use of pre-existing features on the MOOSE platform, as well as create features of our own, as needed. This chapter will concern itself with describing the features that we implemented, as well as how we used pre-existing features to implement the scenarios that we will examine in the following chapters. We will begin this discussion by describing the MOOSE framework itself, before moving on to exploring the Finite Difference method, which, although this is not the method we used, is a relatively simple and intuitive method. This discussion of the Finite Difference method will then be built upon to outline the Finite Element method, which is the method we deployed in this work. We then advance our discussions to the Phase Field model proper, and how we implemented defects in our model to provide the necessary strain fields.

2.1 The MOOSE Framework

The MOOSE (Multiphysics Object Oriented Simulation Environment) framework is a partial differential equation (PDE) solver package [7], using a C++ based finite element method together with the libmesh [63] package (for finite element mesh creation and adaptation) and the PETSc solver package [64–66] (to perform the solution of the PDEs). The way MOOSE solves the PDEs supplied to it is by converting these to weak form, then calculating (and minimising) the residual; we give examples of this later in this chapter, like in Subsection 2.3.1. The MOOSE framework, as a multiphysics tool, has a multitude of different capabilities which are packaged as coupled modules, such as the phase field module [67] and the Navier-Stokes module [68], but there was no magnetism (solid state) functionality present, which we sought to implement. Having discussed the MOOSE framework itself, we will now discuss the finite element method which underpins it, by first exploring the finite difference method and expanding our discussion from there.

2.2 Finite Difference and Finite Element Methods

2.2.1 Finite Difference Method

As an example problem, we will select the one-dimensional heat equation,

$$\frac{\partial U}{\partial t} = \alpha \frac{\partial^2 u}{\partial x^2}. \quad (2.1)$$

2.2 Finite Difference and Finite Element Methods

where U is the temperature in K, x is the displacement in m, α is the thermal diffusivity of the medium in units of m^2s^{-1} and t is the time in s. To approximate this, we break the continuum of x and t into discrete, uniformly distributed steps (thus also ensuring $U(x, t)$ outputs discrete values), and doing so gives us the forward time, central space finite difference equation of

$$\frac{U_{i,\tau+1} - U_{i,\tau}}{\Delta t} = \alpha \frac{U_{i+1,\tau} - 2U_{i,\tau} + U_{i-1,\tau}}{(\Delta x)^2}. \quad (2.2)$$

Therefore,

$$U_{i,\tau+1} = U_{i,\tau} + \alpha \Delta t \frac{U_{i+1,\tau} - 2U_{i,\tau} + U_{i-1,\tau}}{(\Delta x)^2}, \quad (2.3)$$

which means we can approximate our solution for the heat equation at the next timestep, assuming that we know the values of $U_{i,\tau}$, $U_{i+1,\tau}$ and $U_{i-1,\tau}$, which form our initial conditions. Of course, this means for every three pieces of data, we gain one new one, which inevitably means we will run out of information to resolve our model at all points in the space we are interested in. This is where boundary conditions come in; these give the model sufficient information to allow us to keep our spatial resolution as we move forward in time. This method is known as the Euler method, and is the simplest example of a finite difference method. To give an example, we can assume we have a 5 metre long line of material, which we will heat to 373.15K at the point $x=2.6\text{m}$, and the rest of the sample is initially at room temperature 298.15K. The sides of the sample are also held at room temperature. We then evolve the system over time with respect to the heat equation, using timesteps of $\Delta t=1\text{s}$ up to a maximum time of $t=1000\text{s}$, with length elements of $\Delta x=0.2\text{m}$. The results are shown in Figure 2.1.

Of course, being the simplest approximation method comes with the highest error. The magnitude of this error can be calculated by looking at the exact solution of the PDE, performing a Taylor expansion, and comparing this to the approximate solution given by the Euler method. Simplifying the equation we solve to $\partial U/\partial t = f(x, t)$, we can expand this similarly in the fashion used previously, giving the approximation $U(x, t) + \Delta t f(x, t)$. Conducting a Taylor expansion on the exact solution $U(x, t)$, we get $U(x, t) + \Delta t U'(x, t) + ((\Delta t)^2/2)U''(x, t) + O(\Delta t)^3$. Considering that this is the exact solution, where $\partial U/\partial t = f(x, t)$, this evaluates to $U(x, t) + \Delta t f(x, t) + ((\Delta t)^2/2)U''(x, t) + O(\Delta t)^3$ [69]. Comparing these two equations, it can be observed that we have lost information about the terms of order $(\Delta t)^2$ and above during our truncation, which is why this is referred to as the truncation error. Hence, this comparatively large error is why the Euler method is usually not used in practice except for testing; superior methods, such as the Runge-Kutta methods, are preferred, giving a much improved balance

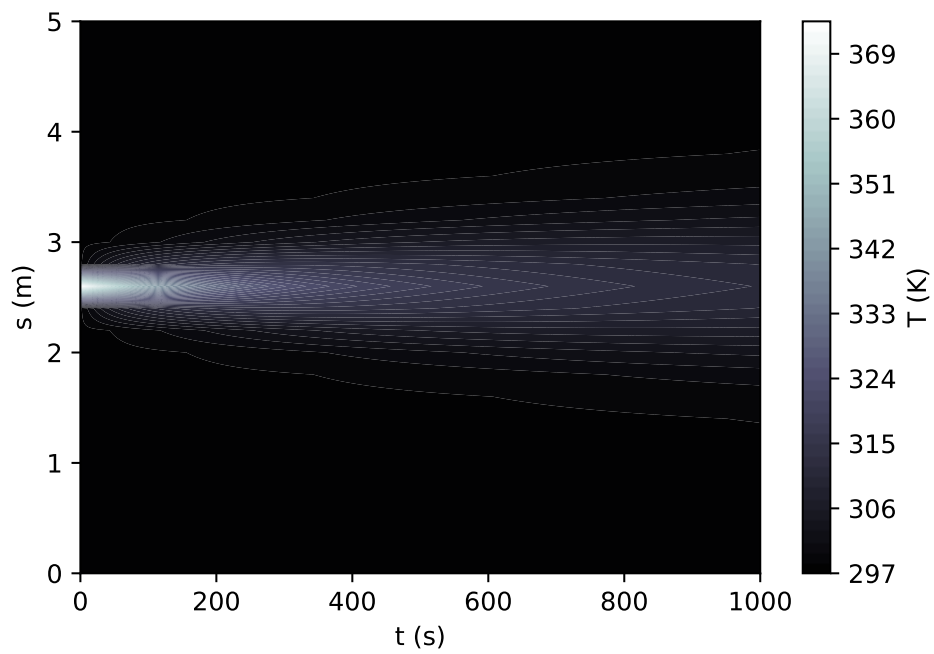


Figure 2.1: Temperature distribution throughout our material, evolved through time according to the one-dimensional heat equation.

between performance and accuracy [70]. The finite difference method has its advantages, key amongst them its simplicity (and therefore efficiency). However, the finite difference method comes with disadvantages also, including difficulty evaluating systems with non-regular domains and complicated sample geometries, and strict requirements on the functions involved to have a certain number of higher-order derivatives [71]. The difficulty regarding non-regular domains and complicated sample geometries in particular would place heavy restrictions on our model regarding magnet geometries and adaptive meshing which would, in turn, hamper generality. Given that we want our model to have the highest possible applicability, we decided to use a different model that could overcome these difficulties. That model was the finite element model, where we move from using the difference in function value between discrete points to solve a partial differential equation (which only gives solutions at those specific points), to using discrete elements of the sample combined with interpolation and integral formalism to give a solution to the equation at all points in the space. We will discuss the finite element model further in the following segment.

2.2.2 Finite Element Method

We start by describing the system we wish to simulate in terms of functionals, which we can then use to create a system of equations through the calculus of variations. This system of equations is then approximated and solved as part of the finite element method, or FEM for short. For simplicity, we will describe the finite element model operating on a 2D sample; other dimensionalities (and shapes) follow by analogy. We begin this process by expressing these PDEs in the weak form; an example for Poisson's equation $-\nabla^2 u(x, y) = f$ is

$$\int_A -\nabla^2 u(x, y)v(x, y)dA = \int_A f v(x, y)dA, \quad (2.4)$$

where u is the function we wish to solve for, f is some arbitrary function we define for the right-hand side of Poisson's equation, v is our test function (an arbitrary well-behaved function we multiply both sides of the PDE with, which relaxes the requirement for the PDE to hold at all points in the sample area, instead the requirement becomes that the PDE only has to hold on average over the area we are integrating over), and dA is an infinitesimal area element of the total area we are integrating over, A . This can be further simplified by vector calculus to remove or reduce derivative terms. We then approximate our system by splitting our sample into discrete, connected subsections, our elements, where this splitting is normally referred to as meshing. This meshing is governed by "conformity rules", which essentially state that any

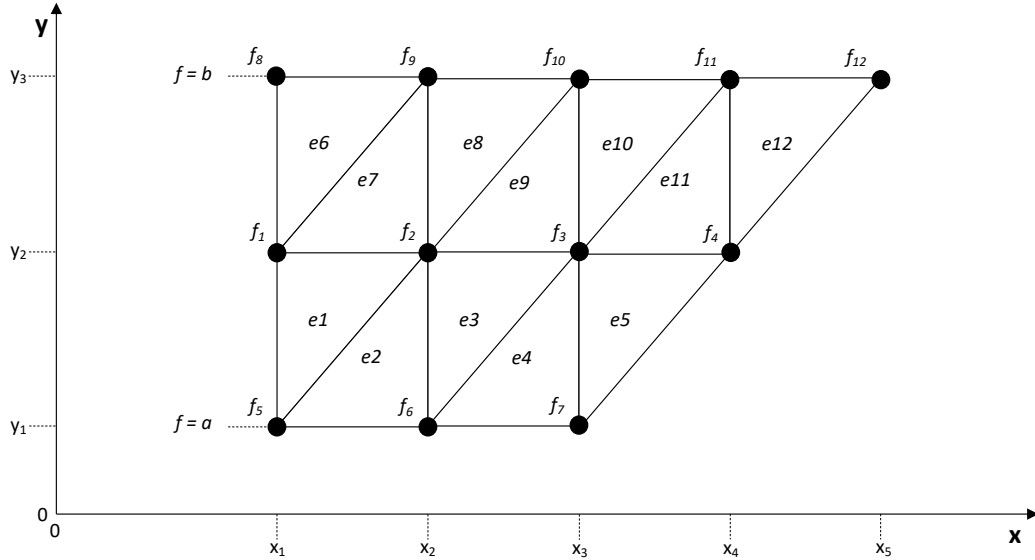


Figure 2.2: Example diagram of a sample being split into elements, for use in the FEM. We represent the nodal value of point i as f_i and the internal elemental function of element j as e_j . Boundary conditions at y_1 and y_3 give $f_5 = f_6 = f_7 = a$ and $f_8 = f_9 = f_{10} = f_{11} = f_{12} = b$ respectively. To find the values of the non-nodal points within each element, we will need to interpolate the solution function throughout the element. Adapted from [10].

two elements may not overlap, and that neighbouring elements must share at least one node between them or a common edge (between nodes); an example of this meshing is shown in Figure 2.2 [10].

We can then take the nodal values of the function and express our original function in terms of these, with our test function, which we can select (these test functions form the basis of our function space); following our Poisson's equation example, this would turn $u(x, y)$ into $\sum_{j=1}^N a_j \phi_j(x, y)$, with a_j being some coefficients, elements of a coefficient matrix, and $\phi_j(x, y)$ being the test functions we've selected as our basis. Given that we know the form and differential/integration behaviour of the test functions ϕ_j , these coefficients a_j can then be evaluated using the Ritz method [72] (after converting the system of equations to matrix form) to find the unknown nodal values not given by initial conditions or boundary conditions by approximating the eigenvalues of the resulting matrix equation; this is a much simpler (and hence quicker) solution than solving the original PDEs themselves, hence justifying the method. However, this only allows us to evaluate nodal values at the nodes where they are

unknown; this does not give us any information about function values between these nodal variables. To find the function values throughout the elements, we then employ interpolation, to evaluate the shape functions, which then allows us to express the value of our solution function at any point. To give an example of how we evaluate these shape functions, we will assume the simplest, non-trivial type; linear interpolation. Following the formalism outlined in [10], we will assume we are operating on our two-dimensional mesh, let us assume our solution function is f . For element one, we will have three nodal values; f_1 , f_2 and f_3 . According to linear interpolation, the function at each nodal value must be of form $f(x, y) = a + bx + cy$. Hence, we generate the following system of equations,

$$\begin{aligned} f_1 &= a + bx_1 + cy_1, \\ f_2 &= a + bx_2 + cy_2, \\ f_3 &= a + bx_3 + cy_3, \end{aligned} \tag{2.5}$$

which we can then summarise in matrix form,

$$\begin{bmatrix} f_1 \\ f_2 \\ f_3 \end{bmatrix} = \begin{bmatrix} 1 & x_1 & y_1 \\ 1 & x_2 & y_2 \\ 1 & x_3 & y_3 \end{bmatrix} \begin{bmatrix} a \\ b \\ c \end{bmatrix}, \tag{2.6}$$

we can then attempt to solve for a, b, c by inverting the central 3×3 matrix, yielding

$$\begin{bmatrix} 1 & x_1 & y_1 \\ 1 & x_2 & y_2 \\ 1 & x_3 & y_3 \end{bmatrix}^{-1} = \frac{1}{D} \begin{bmatrix} (x_2y_3 - y_2x_3) & -(x_1y_3 - y_1x_3) & (x_1y_2 - y_1x_2) \\ -(y_3 - y_2) & y_3 - y_1 & -(y_2 - y_1) \\ x_3 - x_2 & -(x_3 - x_1) & x_2 - x_1 \end{bmatrix}, \tag{2.7}$$

with D being the determinant of the initial matrix, $D = (x_2y_3 - x_3y_2) - (x_1y_3 - y_1x_3) + (x_1y_2 - y_1x_2)$. We can then insert this back into the initial general form of the interpolated function, $f(x, y) = a + bx + cy$, to yield a function of the form $f(x, y) = \psi_1 f_1 + \psi_2 f_2 + \psi_3 f_3$, where we describe the ψ functions as

$$\begin{aligned} \psi_1 &= \frac{1}{D} ((x_2y_3 - y_2x_3) - (y_3 - y_2)x + (x_3 - x_2)y), \\ \psi_2 &= \frac{1}{D} (-(x_1y_3 - y_1x_3) + (y_3 - y_1)x - (x_3 - x_1)y), \\ \psi_3 &= \frac{1}{D} ((x_1y_2 - y_1x_2) - (y_2 - y_1)x + (x_2 - x_1)y). \end{aligned} \tag{2.8}$$

These functions are called the shape functions, ψ_i , and have the following properties within each element:

$$\begin{aligned}\psi_i(x_i, y_i) &= 1, \\ \psi_{j \neq i}(x_i, y_i) &= 0, \\ \sum_{n=1}^3 \psi_n(x, y) &= 1.\end{aligned}\tag{2.9}$$

These shape functions act as weights in our interpolation function [10], allowing us to describe our solution function at any point, completing our description of the FEM. In the following section, we will derive the relevant system of equations we wish to solve, according to the Phase Field model, and how these equations will be solved in MOOSE [7] using the FEM.

2.3 Phase Field Model

2.3.1 Ferromagnetic Exchange

To implement the ferromagnetic exchange, we start by stating the corresponding free energy, Equation 1.1. MOOSE's Phase Field module [7, 67] contains a kernel, *ACInterface*, which applies the Allen-Cahn equation 1.52 to energy terms of the form $\frac{\kappa_i}{2} (\nabla m_i)^2$, i.e.

$$\frac{\partial m_i}{\partial t} = -L_i \frac{\delta \frac{\kappa_i}{2} (\nabla m_i)^2}{\delta m_i}.\tag{2.10}$$

which evaluates to

$$\frac{\partial m_i}{\partial t} = L_i \kappa_i \nabla^2 m_i.\tag{2.11}$$

by using the Euler-Lagrange relation. Converting this into MOOSE formalism by transforming it into a weak form PDE, we multiply both sides by a test function ϕ_i and subtract one side from the other to leave the residual R ,

$$\int_{\Omega} \frac{\partial m_i}{\partial t} \phi_i dV - L_i \int_{\Omega} \kappa_i \nabla^2 m_i \phi_i dV = R.\tag{2.12}$$

using the relation $\nabla \cdot (\phi_i \nabla m_i) = \nabla \phi_i \nabla m_i + \phi_i \nabla^2 m_i$ and applying the divergence theorem, we achieve

$$\left(\frac{\partial m_i}{\partial t}, \phi_i \right)_V + (\kappa_i \nabla m_i, L_i \nabla \phi_i)_V - \langle L_i \kappa_i \nabla m_i \cdot \hat{\mathbf{n}}, \phi_i \rangle_S = R, \quad (2.13)$$

where the brackets \langle, \rangle_S indicate a surface integral over the product of the two variables separated by the comma, which represents a boundary condition, and the brackets $(,)_V$ which similarly represent a volume integral over the same product. Minimising the residual R whilst evolving the magnetisation components m_i , means that we are pushing the magnetisation components along their respective gradients, with the end result being the minimisation of the overall magnetisation gradient. Hence, this term will act to reduce the magnetisation gradient throughout the sample, implementing our ferromagnetic coupling, where the exchange stiffness A is equal to $\frac{\kappa_i}{2}$. Now that we have looked at how we added the ferromagnetic coupling to our model, we can now look to how we performed the more difficult task of implementing the antiferromagnetic coupling.

2.3.2 Antiferromagnetic Exchange (*ADImprovedAFM*)

We will start by applying the Allen-Cahn Equation 1.52 to the energy density functional, Equation 1.2. We have taken the mobility L , in units of $(\text{nm})^3(\text{meV})^{-1}\text{s}^{-1}$, to be unity for simplicity. J is positive for an antiferromagnet. This gives us

$$\frac{\partial m_{1x}}{\partial t} = -Jm_{2x} \quad (2.14)$$

when taking the x -component of the first magnetic sublattice as an example (the other components, including for the second sublattice, follow). Converting this into MOOSE form, we obtain

$$\left(\frac{\partial m_{1x}}{\partial t}, \phi_x \right)_V + (Jm_{2x}, \phi_x)_V = R \quad (2.15)$$

where all symbols retain their previously defined meanings. For the residual to be minimised, the magnetisation vector component of the sublattice in question will evolve to be of opposite sign to the same magnetisation vector component on the opposite sublattice, in the absence of other influences such as the magnetoelastic coupling which may break perfect antiferromagnetic alignment. This form of antiferromagnetic coupling, when coded, gave the expected results (in absence of other influences, magnetisation vectors of the different sublattices are antiparallel). Our implementation was tested and verified using the spin-flop and spin-flip transition (see Chapter 3). Having discussed the implementations of the magnetic exchange

types along with their FEM/MOOSE forms, we can now look at the implementations of other magnetic phenomena such as the magnetocrystalline anisotropy and non-magnetic phenomena, the elastic energy minimisation.

2.3.3 Magnetocrystalline Anisotropy

Here, we will discuss the types of anisotropy relevant to us, the uniaxial anisotropy and cubic anisotropy, starting with the former. Substituting our equation for the uniaxial anisotropy (Equation 1.3) in the Allen-Cahn equation (Equation 1.52), we get

$$\frac{\partial m_z}{\partial t} = 2K_{\text{Uni}}m_z, \quad (2.16)$$

and converting this to the weak form, we achieve

$$\left(\frac{\partial m_z}{\partial t}, \phi_z \right)_V - (2K_{\text{Uni}}m_z, \phi_z)_V = R. \quad (2.17)$$

It can be observed that, depending on the sign of K_{Uni} , we expect different behaviour. When $K_{\text{Uni}} > 0$, to minimise the residual R , m_z will evolve to be maximal along either $+z$ or $-z$ (limited only by our constraint term, described in Chapter 1), as expected from information in Chapter 1, giving an easy-axis anisotropy. Alternatively, if $K_{\text{Uni}} < 0$, the same logic implies we must minimise m_z to minimise R (i.e. if m_z is positive, the derivative is negative and vice-versa), giving us an easy-plane anisotropy, here on the $x - y$ -plane. Having looked at the uniaxial anisotropy, we can now turn our attention to the cubic anisotropy, Equation 1.4, given that we will be looking at cubic antiferromagnets in this work (though this can be generalised to other crystal symmetries and associated anisotropies, by altering the free energy densities and elasticity tensor accordingly, however this will not be conducted here). Applying our now familiar treatment to this for the m_x component, we firstly achieve

$$\frac{\partial m_x}{\partial t} = -L_x \left(2K_1m_x (m_y^2 + m_z^2) + 2K_2m_xm_y^2m_z^2 \right), \quad (2.18)$$

and then,

$$\left(\frac{\partial m_x}{\partial t}, \phi_x \right)_V + \left(2K_1m_x (m_y^2 + m_z^2) + 2K_2m_xm_y^2m_z^2, L_x\phi_x \right)_V = R. \quad (2.19)$$

Explaining the expected magnetic behaviour as a result of this kernel is more complicated than doing so for the previously discussed kernels. To begin with, we will look at the first term of Equation 1.4. It can be demonstrated that, for a positive K_1 , this would lead to energetically

favoured easy- axis directions along the x -, y - and z - directions, i.e. the simple cubic lattice vectors. If, instead, we assume we have a negative K_1 , the former easy-axis directions are now hard-axes; the new easy-axes for this scenario are now the $(1/\sqrt{3}, 1/\sqrt{3}, 1/\sqrt{3})$ direction and its associated counterpart directions from symmetry.

Having looked at the effect of this first term, it is now prudent to examine the second term in Equation 1.4. We have expected easy directions of x , y and z , and indeed any directions pertaining to the $x - y$, $x - z$ and $y - z$ planes, in the case of a positive K_2 . Conversely, for a negative K_2 , the $(1/\sqrt{3}, 1/\sqrt{3}, 1/\sqrt{3})$ direction and its associated counterpart directions from symmetry are the easy-axes.

Of course, to get further insight into this, we should look at both terms together. Firstly, let's assume that we have a positive K_1 . In this scenario, we have three different regimes, depending on the relative magnitude (and sign) of K_2 with respect to K_1 . The first regime occurs between $K_2 = \infty$ and $K_2 = -9\|K_1\|/4$ (negative value non-inclusive), where we have the established status quo for a positive K_1 . Once we reach the value of $K_2 = -9\|K_1\|/4$, the previously established “medium” and “hard” directions switch places. When the value of $K_2 = -9K_1$ is reached, the $(1/\sqrt{3}, 1/\sqrt{3}, 1/\sqrt{3})$ axis and its symmetric counterparts become the new easy axes, the Cartesian axes become the medium axes, and the axes along the Cartesian planes remain the new hard axes. We can now consider the case where K_1 is negative, where we once again end up with three regimes depending on the relative sign and magnitude of K_2 with respect to K_1 . For values of K_2 from $-\infty$ up to but not including $9\|K_1\|/4$, we have that the easy axes are those axes symmetric to $(1/\sqrt{3}, 1/\sqrt{3}, 1/\sqrt{3})$, the medium axes are those along the Cartesian planes, and the hard axes are the Cartesian axes. Once the value of $K_2 = 9\|K_1\|/4$ is reached, we have that the easy and medium axes swap places once this value is surpassed. When the value of $K_2 = 9\|K_1\|$ is reached, where the axes symmetric to $(1/\sqrt{3}, 1/\sqrt{3}, 1/\sqrt{3})$ become the hard axes and the Cartesian axes become the new medium axes. To demonstrate the variation of easy, medium and hard axes with these anisotropy constants, a diagram is provided (Figure 2.3). Now that we have discussed the purely magnetic terms that we will use with MESMER, we will now move to the discussion of the elastic energy and conclude with the description of the magnetoelastic term.

2.3.4 Elasticity

The majority of our treatment of elastic strains and stresses, particularly those arising purely from the effect of defects or distortions in the samples crystalline structure, is conducted via

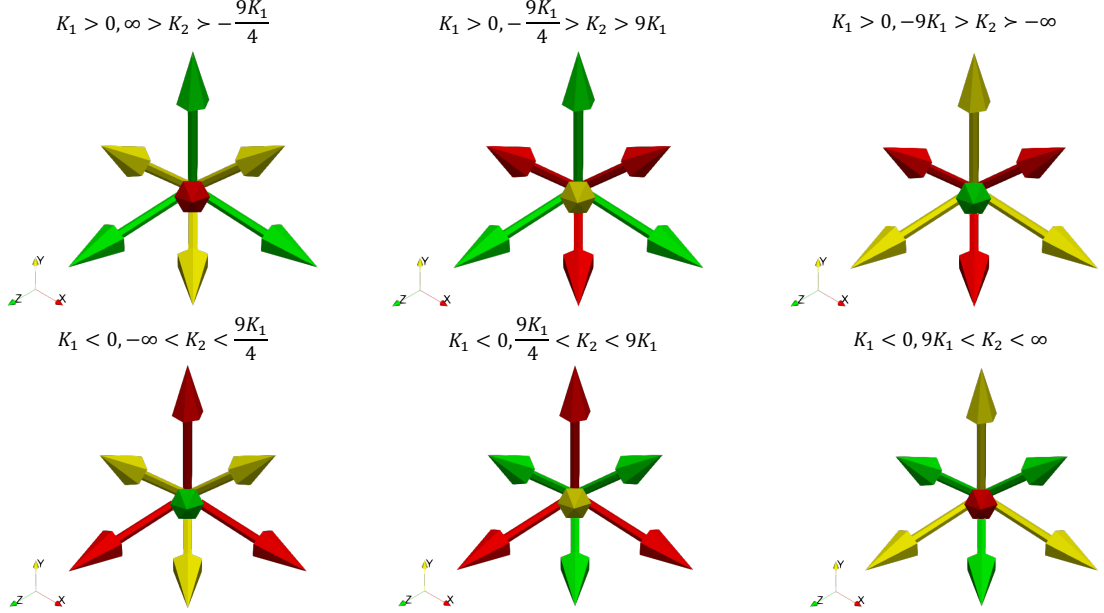


Figure 2.3: Easy (green), medium (yellow) and hard (red) axes for regions of values of the two cubic anisotropy constants, from an isometric perspective of the positive octant.

the Tensor Mechanics module in MOOSE. However, the “spontaneous” stress-free strains, ξ , arising from the magnetoelastic coupling, are treated via the Phase Field module. This treatment of the “spontaneous” strains via the Allen-Cahn equation 1.52 can be split into two parts; the minimisation of the elastic energy and the magnetoelastic energy. Firstly, for the elastic energy treatment, we start by expanding the elastic energy density, Equation 1.7, for an isotropic material (this will be assumed as an example; other material symmetries follow by analogy), which results in

$$f_{\text{el}} = \frac{C_{11}}{2} (\xi_{xx}^2 + \xi_{yy}^2 + \xi_{zz}^2) + C_{12} (\xi_{xx}\xi_{yy} + \xi_{xx}\xi_{zz} + \xi_{yy}\xi_{zz}) + 2C_{44} (\xi_{xy}^2 + \xi_{xz}^2 + \xi_{yz}^2). \quad (2.20)$$

Taking the xx component of the (“spontaneous”) strain, ξ_{xx} , as an example of the diagonal components, we can use the Allen-Cahn Equation 1.52 and convert into MOOSE form, resulting in

$$\left(\frac{\partial \xi_{xx}}{\partial t}, \psi_i \right)_V + \left(C_{11}\xi_{xx} + C_{12} (\xi_{yy} + \xi_{zz}), L\psi_i \right)_V = R, \quad (2.21)$$

and performing the same on an example of the cross components, ξ_{xy} , we also achieve

$$\left(\frac{\partial \xi_{xy}}{\partial t}, \psi_i \right)_V + (4C_{44} \xi_{xy}, L\psi_i)_V = R. \quad (2.22)$$

Now that we have looked at the PDEs we will have to solve to minimise the elastic energy, we can now finally look at the magnetoelastic coupling, which will use these spontaneous strains also.

2.3.5 Magnetoelasticity

Using the magnetoelastic energy density, Equation 1.19, we can look at the PDEs that are derived from this that will be solved using MOOSE. Firstly, we can look at the PDEs relating to the magnetisation. Taking the x -component of magnetisation, we achieve the MOOSE form of

$$\left(\frac{\partial m_x}{\partial t}, \psi_i \right)_V - \left((C_{11} - C_{12}) \lambda_{100} m_x \epsilon_{xx} + 2C_{44} \lambda_{111} (m_y \epsilon_{xy} + m_z \epsilon_{xz}), 3L\psi_i \right)_V = R, \quad (2.23)$$

where ϵ is the total strain tensor, $\epsilon = \zeta + \xi$. Secondly, we can follow the same logic for the spontaneous strain tensor components,

$$\left(\frac{\partial \xi_{xx}}{\partial t}, \psi_i \right)_V - \left((C_{11} - C_{12}) \lambda_{100} m_x^2, \frac{3}{2} L\psi_i \right)_V = R. \quad (2.24)$$

This concludes the discussion on the PDEs we will solve using the FEM. We will now move to discussing how the elastic strain tensor components, used in the magnetoelastic coupling, are derived in MESMER, in the case of an Eshelby Inclusion defect.

2.4 Defect Modelling

To model the Eshelby Inclusion defects discussed in Chapter 1, we will make use of the Tensor Mechanics module in the MOOSE framework.

$$\hat{\zeta} = p \hat{\zeta}_{\text{Eigen}} \quad (2.25)$$

where p is the pre-factor, and ζ_{Eigen} is the eigenstrain base tensor that we will supply in the input file. The eigenstrain tensor ζ_{Eigen} we supplied consisted only of the volumetric terms applicable to the dimensionality of the mesh, i.e.

$$\hat{\zeta}_{\text{Eigen}} = \begin{bmatrix} \zeta_{\text{Eigen},xx} \\ \zeta_{\text{Eigen},yy} \\ \zeta_{\text{Eigen},zz} \\ 0 \\ 0 \\ 0 \end{bmatrix} \quad (2.26)$$

for a three-dimensional mesh, where the zero terms are the off-diagonal components, $\zeta_{\text{Eigen},xy}$, $\zeta_{\text{Eigen},xz}$ and $\zeta_{\text{Eigen},yz}$. The pre-factor we applied was of the form $p = kc^2$, where k is a dimensionless constant, which is the percentage the defect would expand along any of the axial directions if the surrounding material was not present, and c is the concentration of defective material in that element. On a pragmatic level, the c variable acts as a flag, so that the eigenstrain is only present where inclusion defects are present, and this is squared to ensure a quick drop off in the interpolation with surrounding material such that it is not counted as defective. The Tensor Mechanics module then calculates the strain configuration in the surrounding material so as to accommodate the defective material, according to the Eshelby formalism discussed in Chapter 1. To give an example in 2D, if we assume that we would have a 5% expansion in the defective material outside of the surrounding material, such that $p = 0.05$, and that we have a $10\text{nm} \times 10\text{nm}$ defect in the centre of a $100\text{nm} \times 100\text{nm}$ sample with Poisson's ratio $\nu = 0.3$, we achieve the strain configuration shown in Figure 2.4, where the eigenstrain is observable in the centre of the strain component diagrams. By adjusting c throughout the sample, we are able to implement multiple defects in a variety of geometrical configurations. Additionally, by adding a sign variable s to our pre-factor p , such that $p = skc^2$, we can implement defects which have the opposite polarity, i.e. the defect material seeks to contract rather than expand. An example of this kind of configuration is shown in Figure 2.5; the strain structure shown appears to have a dipolar characteristic, which may lead to interesting magnetisation configurations through the magnetoelastic coupling, which we will explore in a later chapter.

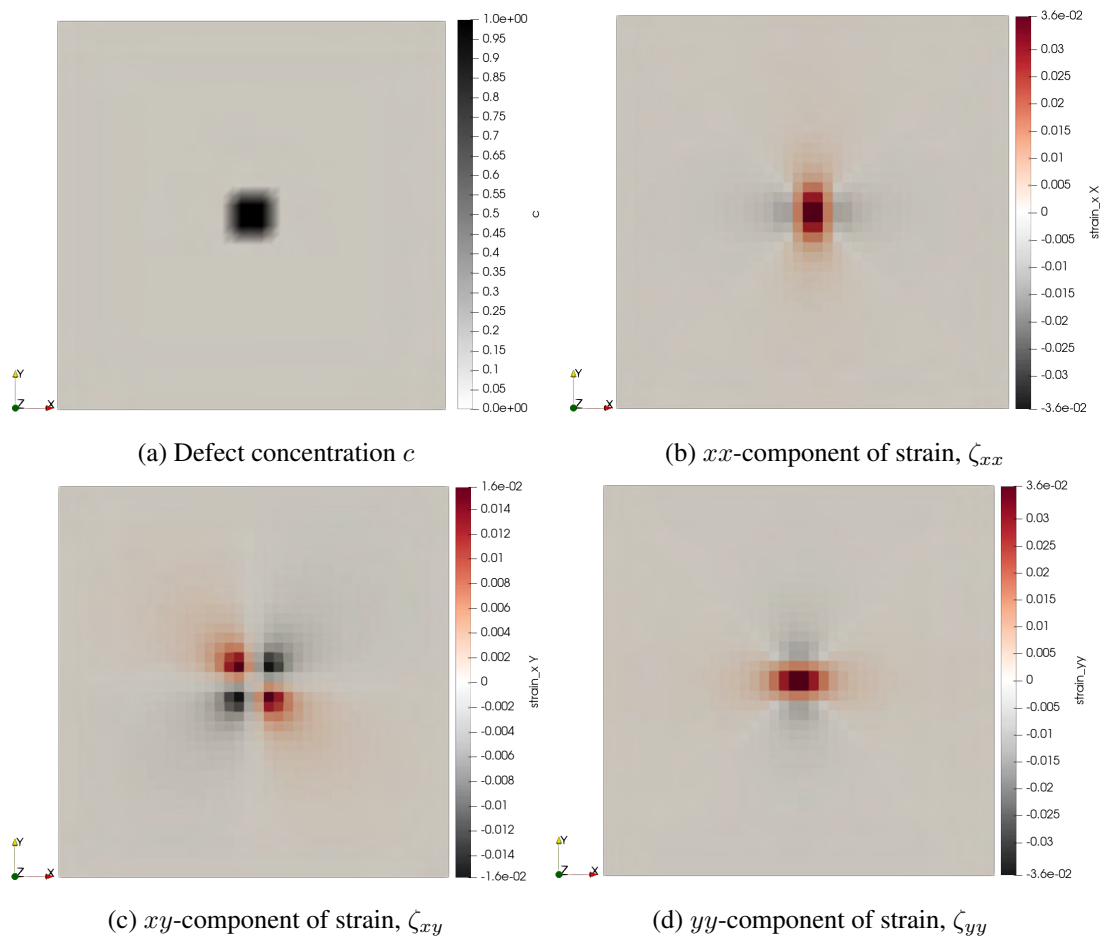


Figure 2.4: An example of an Eshelby inclusion defect, as implemented in our simulations. The defect concentration c , in Figure 2.4a, is directly related to the eigenstrain, observable in the centre in Figures 2.4b and 2.4d.

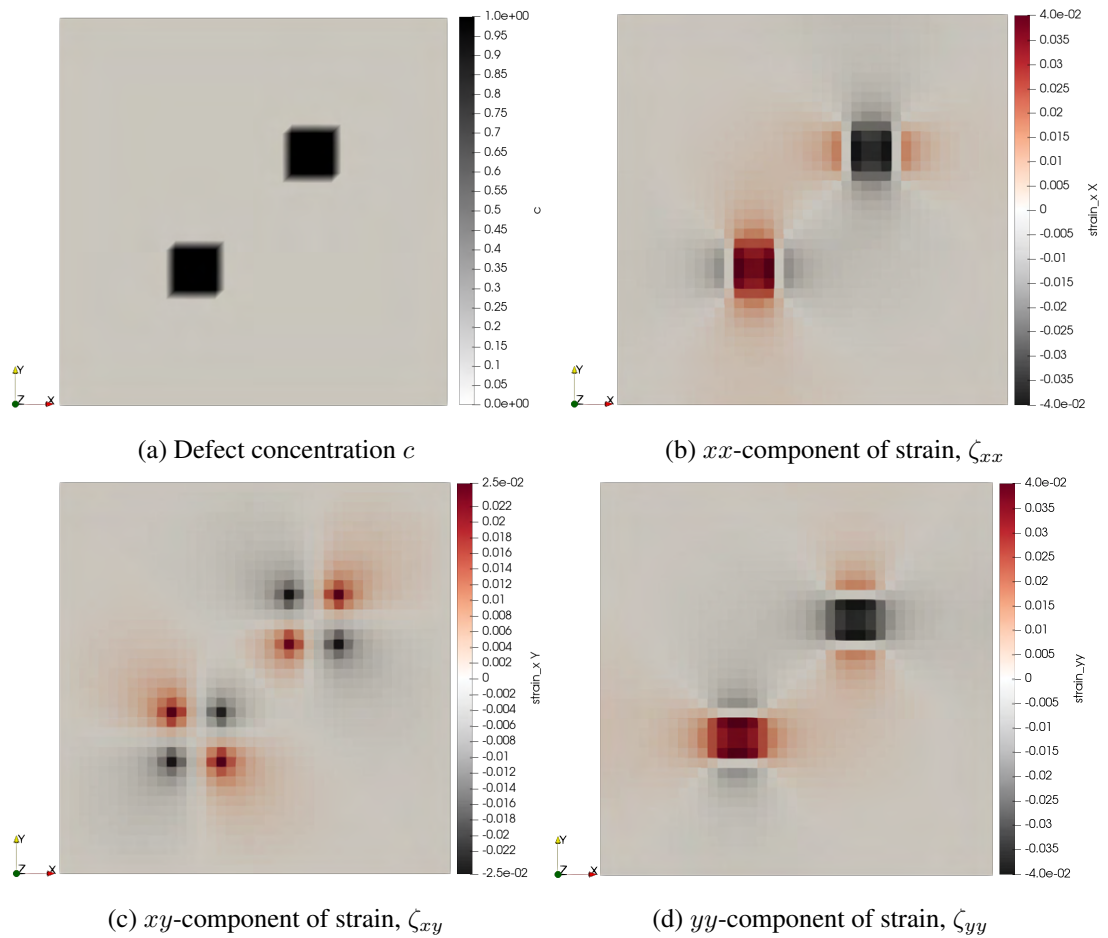


Figure 2.5: Example of an inverted defect configuration, where the top-right defect is inverted (the sign variable s is set to -1) and the bottom-left defect is not inverted (the sign variable s is set to 1).

Summary

- The finite difference method is described, and a simple example using the heat equation is given.
- We discuss the finite element method, which will be used extensively in this work. In particular, we examine closely the mechanics of meshing and interpolating over individual elements.
- Implementation of the phenomena described Chapter 1 in our phase field model is detailed. We outline this process for each term, where we go from the initial free energy density to the final form of the resulting partial differential equation.
- We demonstrate how we use our model to implement Eschelby inclusions, along with the calculation of their associated strain fields. We further provide diagrams to illustrate the calculated strain fields, along with the defect locations and geometries.

CHAPTER 3

Verification of MESMER

3.1 Using Domain Wall Width Analysis to Verify Exchange and Anisotropy Implementation

In the previous chapter we described how we implemented various phenomena in our model, including the magnetocrystalline anisotropy and the antiferromagnetic exchange. However, before we proceed further with our analysis, it is important to verify that these implementations produce the correct results. We resolved to do this by testing our model against analytic results and doing a detailed comparison. In this chapter, we will describe how we used a domain wall width analysis and the spin-flop and spin-flip transitions to test and verify our implementation of the magnetocrystalline anisotropy, the ferromagnetic exchange and the antiferromagnetic exchange in our model.

3.1 Using Domain Wall Width Analysis to Verify Exchange and Anisotropy Implementation

In a co-linear cubic antiferromagnet like NiO, there are two components of exchange; the ferromagnetic-like intralattice exchange, and the antiferromagnetic interlattice exchange. Before encoding the antiferromagnetic exchange, it was prudent to look at the implementation of the ferromagnetic coupling first, as this would be important to the model as a whole and would inform the implementation of the antiferromagnetic coupling at a later time. We decided to use the *ACInterface* kernel to implement the ferromagnetic coupling (see Subsection 2.3.1). This, together with the *AllenCahn* kernel itself (with the associated free energy densities applicable) needed to be verified to be giving the correct results before moving on to magnetoelasticity and antiferromagnetism. The way we sought to do this was by performing a simple domain wall analysis.

The reasoning behind the selection of a domain wall analysis as the verification for these features was that the domain wall width δ (in units of nm) has an analytical form directly related to the exchange stiffness constant A (in units of $\text{meV}(\text{nm})^{-1}$) and the first order anisotropy coefficient K (in units of $\text{meV}(\text{nm})^{-3}$),

$$\delta = \pi \sqrt{\frac{A}{K}}, \quad (3.1)$$

and by evolving an appropriate scenario using our phase field model, we can fit the magnetisation profile along the magnet (using an appropriate axis) to extract the domain wall width δ , which can then be compared to the analytical value to verify our implementation of the ferromagnetic coupling, uniaxial anisotropy and the magnetisation vector normalisation. We will go on to discuss the initial conditions of the system we wish to model, the mechanics that will

3.1 Using Domain Wall Width Analysis to Verify Exchange and Anisotropy Implementation

be active in our model, and the results obtained as well as their interpretation.

The system we wished to simulate was set up as follows. A mesh of uniform rectangular elements was created for a long, thin bar magnet, with unit micrometre length in the x -direction, and a square-cross section in the $y - z$ -plane of dimensions 10nm by 10nm. The initial conditions of the magnetisation components were

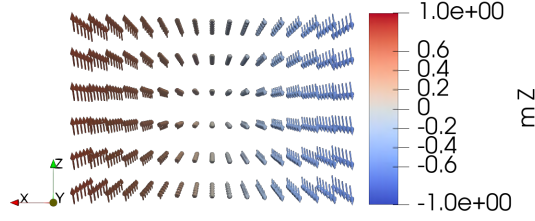
$$m_x = 0, m_y = \left(\cosh \frac{\pi (x - 500)}{\delta_{\text{seed}}} \right)^{-1}, m_z = \tanh \frac{\pi (x - 500)}{\delta_{\text{seed}}}, \quad (3.2)$$

respectively, where x is the x -coordinate of that given element (in nm), and seed is our initial value of the initial domain wall (in order for the test to be useful, this has to be sufficiently different to the expected final value of the domain wall). It can be easily proven that this initial condition satisfies our unit length magnetisation requirement. For this simulation, we included free energy density terms for the uniaxial anisotropy (Equation 3.8), ferromagnetic exchange (Equation 3.5) and the unit length magnetisation constraint (Equation 1.62). Additionally, Dirichlet boundary conditions (*DirichletBC* in MOOSE) were applied at the ends of the magnet along the x -direction to constrain the magnetisation, so as to keep the domain wall stable. This constraint sets the magnetisation vector (anti-)parallel to the z -axis at the face furthest along the x -axis in the (negative) positive direction. Our focus then turned to the selection of appropriate parameters. For this simulation, we selected the exchange stiffness coefficient A and the first order anisotropy constant K_1 to be comparable with the observed values for iron (Fe) [73] [74]. These values are $A = 125\text{meV (nm)}^{-1}$, $K_1 = 0.3\text{meV (nm)}^{-3}$, and we use a constraint coefficient of $\lambda = 1000\text{meV (nm)}^{-3}$. Using the first two of these values together with Equation 3.1, we can calculate that the steady-state domain wall width δ is 64.13nm. Knowing this, we selected the “seed” value of the domain wall width δ_{seed} to be 40nm, so as to give a meaningful test for the situation, to allow it to relax to the correct steady-state domain wall width value. The system was then allowed to evolve under this setup, and the domain wall was visually observed to expand under this regime, giving a steady-state magnetisation profile such as that shown in Figure 3.1. After the simulation successfully converged, the variable data was extracted. This variable data was then processed using a Python fitting script, to extract the domain wall width δ , the height h (dimensionless) of the magnetisation profile and the centre C (in nm) from the magnetisation profile, an example of which can be seen in Figure 3.2. The equations fitted are outlined in Equation 3.3,

3.1 Using Domain Wall Width Analysis to Verify Exchange and Anisotropy Implementation



(a) Diagram showing the magnetisation vector throughout a truncated section of the bar magnet. The area highlighted by the red rectangle is shown in further detail in Fig. 3.1b. The ends of the magnet are pinned, by boundary conditions, to be aligned along opposite directions along the z -axis, and the domain wall can be clearly observed in the centre.



(b) The section highlighted by the red rectangle in Fig. 3.1a. The domain wall is initially implanted to be of width $\delta = 40nm$, and is allowed to relax, and by extracting the magnetisation profile we can get the steady-state (shown here in Fig. 3.1) domain wall width, which can be compared to the analytical value.

Figure 3.1: Steady-state solution of our domain wall simulation, which we can use to verify the implementation of ferromagnetic coupling, uniaxial anisotropy and the unit magnetisation vector constraint by fitting the magnetisation profile.

$$m_x = 0 \cdot x, m_y = h \cdot \left(\cosh \frac{\pi(x-c)}{\delta} \right)^{-1}, m_z = h \cdot \tanh \frac{\pi(x-c)}{\delta}, \quad (3.3)$$

where h is the height of the domain wall profile (i.e. the magnetisation magnitude, which should be 1 here), c is the centre of the domain wall profile, and δ is the domain wall width. The values for the domain wall width δ were then plotted against the simulation time. If our model is functional, and the free energy terms used correct, then as the simulation progresses, it would be expected that the fitted domain wall width would converge towards the analytically expected domain wall width value. This was indeed the case and can be observed in Figure 3.3, showing that our model, and the free energy density terms used in it, are accurate, and this sets the basis for our further use of the model. We then sought to implement and verify other features, the antiferromagnetic exchange and magnetoelastic coupling.

3.1 Using Domain Wall Width Analysis to Verify Exchange and Anisotropy Implementation

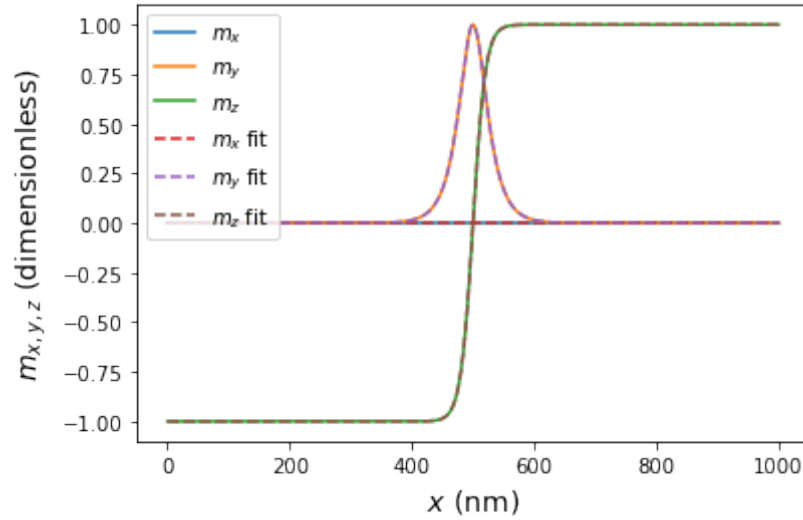


Figure 3.2: An example of the fitting profiles used to ascertain the domain wall width δ . The value of 64.13, in units of nm, is the exact domain wall width; the value we obtain by fitting is 64.17 in the same units, which is a convincing match, verifying our implementation of the magnetocrystalline anisotropy and the ferromagnetic exchange in our model. The domain wall is centered at $x = 500\text{nm}$ and has a magnitude of 1.

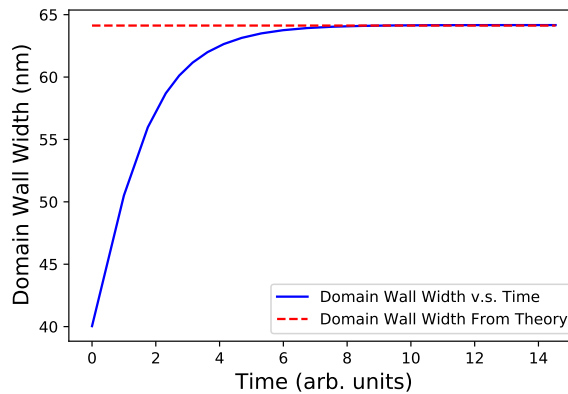


Figure 3.3: Graph of domain wall width δ (in nm) versus time (in arbitrary units), showing the convergence of the model towards the correct analytic result. This result verifies that the exchange interaction, the uniaxial anisotropy and the magnetisation vector normalisation are working correctly. The values used in this plot were obtained from the fitting profiles, an example of which can be observed in Fig. 3.2.

3.2 Using the Spin-Flop and Spin-Flip Transition to Verify the Antiferromagnetic Exchange

Despite the high resistance antiferromagnets have to magnetic fields, if an applied magnetic field is sufficiently strong, it may affect the antiferromagnetic ordering of the material. Specifically, at two critical field strengths, the following will occur: at the first critical field strength, the Néel vector will align itself to be perpendicular to the applied field direction (the spin-flop transition), and at the second critical field strength, the antiferromagnetic ordering breaks down completely i.e. the Néel vector drops to magnitude zero as the magnetisation vectors of the two sublattices align along the field direction (the spin-flip transition). These critical field strengths can be found analytically, and by comparing these analytical values to numerical values obtained from our simulation of this situation, we can verify that our antiferromagnetic coupling, as implemented here (using *ADImprovedAFM*), is accurate.

For the spin-flip point analytical calculation, we will follow the scheme given by [75]. We will start by defining the exchange magnetic induction, \mathbf{B}_E , as being

$$\mathbf{B}_E = -\frac{\partial U_E}{\partial \mathbf{M}}, \quad (3.4)$$

where

$$f_E = J\mathbf{m}_1 \cdot \mathbf{m}_2. \quad (3.5)$$

Combining Eq. 3.4 and Eq. 3.5, we get that \mathbf{B}_E is given by

$$\mathbf{B}_E = -\frac{J\mathbf{m}_2}{M_s}. \quad (3.6)$$

Using our values of the exchange constant J and saturation magnetisation M_s of $2.00 \cdot 10^7 \text{Jm}^{-3}$ and $8.60 \cdot 10^5 \text{Am}^{-1}$, this gives us a value of 23.3T for \mathbf{B}_E . We can now use a similar strategy for the anisotropy magnetic flux density \mathbf{B}_A , where

$$\mathbf{B}_A = -\frac{\partial U_A}{\partial \mathbf{M}}, \quad (3.7)$$

$$U_A = K_1 (1 - (\mathbf{z} \cdot \mathbf{m})^2) = K_1 (1 - m_z^2), \quad (3.8)$$

and, therefore,

$$\mathbf{B}_A = \frac{2K_1 \mathbf{m}_z}{M_s}. \quad (3.9)$$

Inserting our value of the first order anisotropy constant K_1 of $4.81 \cdot 10^4 \text{Jm}^{-3}$ and using the saturation magnetisation from the previous calculation, we achieve a value of $1.12 \cdot 10^{-1} \text{T}$ for

3.2 Using the Spin-Flop and Spin-Flip Transition to Verify the Antiferromagnetic Exchange

the anisotropy magnetic flux density.

Now that we have the values for the exchange and anisotropy magnetic flux densities, we can calculate the critical flux densities for the spin-flop and spin-flip critical points. Using formulae from [75], we get that the magnitude of the spin-flop and spin-flip fields are, respectively,

$$B_{\text{Flop}} = \sqrt{2(\mathbf{B}_E \cdot \mathbf{B}_A)} \quad (3.10)$$

and

$$B_{\text{Flip}} = 2\|\mathbf{B}_E\|. \quad (3.11)$$

Inputting our obtained flux densities from earlier, we obtain values of $B_{\text{Flop}} = 2.28\text{T}$ and $B_{\text{Flip}} = 46.5\text{T}$. These can now be used to compare with the values obtained from our simulations.

Firstly, we will look at the spin-flop transition. We will firstly start in the (highly unstable) initial configuration where the first sublattice magnetisation vector is pointing parallel to the z -axis and the second sublattice magnetisation vector is pointing parallel to the x -axis. We add the antiferromagnetic coupling term and uniaxial anisotropy term (along z , first order anisotropy constant $K_1 = 4.81 \cdot 10^4 \text{Jm}^{-3}$, along with the magnetisation length constraint. We then added an applied field term (Zeeman term), with the magnetic flux density being applied along the z -axis with magnitude $\|\mathbf{B}\| = 2\text{T}$. This system was then allowed to relax under the phase field model, then the magnitude of the applied magnetic flux density was increased in increments of 0.1T and the simulation repeated until $\|\mathbf{B}\| = 3\text{T}$ was reached. The separation angle along the x -axis, ϕ , was then obtained from the simulation by comparing the x -component of magnetisation of the two sublattices. The results were then tabulated and graphed as shown in Fig. 3.4a, where the analytic spin-flop induction is shown. Finite size effects were considered, but the relative error magnitudes involved were insignificant (sub-1%) and the transition value is the only value of interest to us rather than the absolute values of the angles, so we did not include these in the diagram. The cliff-edge in the data points coincides with the analytic spin-flop point, which confirms that our antiferromagnetic coupling is working correctly.

We can now look to the spin-flip transition point. Taking the same initial conditions from before and ramping up the applied magnetic flux density from 40T to 50T , we can determine the spin-flip point in our model by examining the interval in which the separation angle between the magnetisation vectors of the first and second sublattices drops to zero. The results of this process can be seen in Figure 3.4b. The interval in which the separation angle drops to zero is the region between 46T and 47T , which when compared to the analytically calculated value

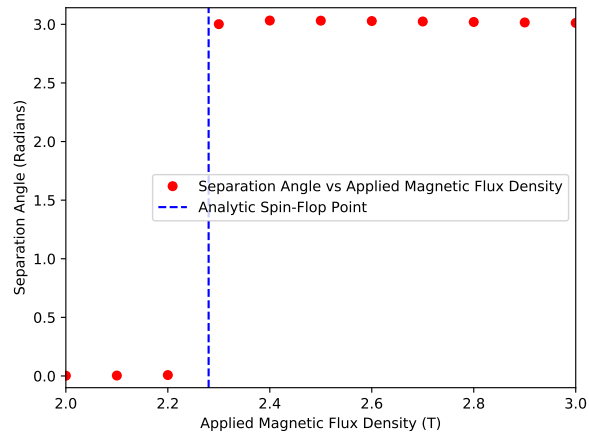
3.2 Using the Spin-Flop and Spin-Flip Transition to Verify the Antiferromagnetic Exchange

of 46.5T, is entirely consistent with theory, and when combined with our earlier spin-flop analysis, verifies that our antiferromagnetic coupling is working correctly, and can now be used in combination with the other components to our model. Like the spin-flop case, we considered finite size effects, but found that these were a small source of error and did not hinder the finding of the transition point, so these errors were not included in the graph.

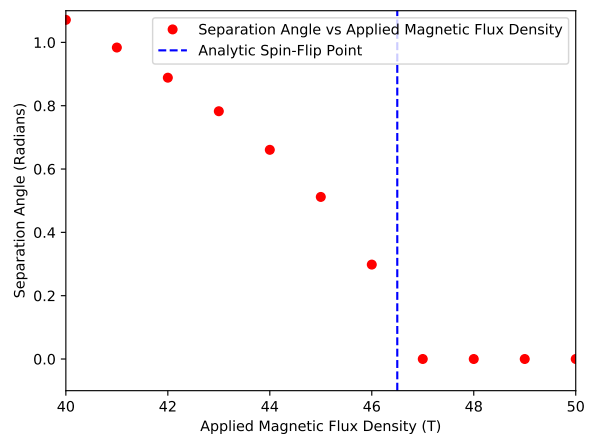
Summary

- We use a simulation, including a ferromagnetic exchange and a uniaxial anisotropy, to measure the width of the resulting domain wall. Given that we can find the width of the domain wall analytically, we used this to verify both the ferromagnetic coupling and the uniaxial anisotropy implementation in our model. The analytic and numerical results compared well, justifying our implementation.
- The strength of applied magnetic field necessary to effect the spin-flop and spin-flip transitions in an antiferromagnet are analytically calculable. Hence, we ran simulations where we applied an increasingly strong magnetic field to an antiferromagnet, to find the spin-flip and spin-flop points. The spin-flop and spin-flip points found in the simulations compared favourably to the analytic values, demonstrating the accuracy of our implementation of the antiferromagnetic coupling.

3.2 Using the Spin-Flop and Spin-Flip Transition to Verify the Antiferromagnetic Exchange



(a) Graph of separation angle (here along the x -axis) between magnetisation vectors of the two magnetic sublattices vs the magnetic induction applied to the antiferromagnet.



(b) Graph of separation angle (here along the z -axis) between magnetisation vectors of the two magnetic sublattices vs the magnetic induction applied to the antiferromagnet.

Figure 3.4: Graphs showing magnetisation vectors of the two magnetic sublattices vs the magnetic induction applied to the antiferromagnet for different ranges of applied magnetic induction. The analytic flop/flip points are illustrated on Fig. 3.4a/3.4b respectively with blue dotted lines. The results obtained from our simulation match very well with the analytic results, which is particularly obvious in the spin flop case. This verifies that antiferromagnetic coupling is working correctly.

CHAPTER 4

Nucleation of Magnetic Domains in
Antiferromagnets by the Magnetoelastic
Coupling

4.1 Nucleation of Magnetic Domains in Antiferromagnets by the Magnetoelastic Coupling

Term	Equation	Parameter Values
Intra-lattice Exchange	Equation 1.1	$A = 3.97017 \text{ meV}(\text{nm})^{-1}$
Inter-lattice Exchange	Equation 1.2	$J = 57.61979 \text{ meV}(\text{nm})^{-3}$
Cubic Anisotropy	Equation 1.4	$K_1 = 0.24532 \text{ meV}(\text{nm})^{-3}$, $K_2 = 0.12266 \text{ meV}(\text{nm})^{-3}$
Magnetisation Constraint	Equation 1.62	$\lambda = 1.00 \cdot 10^5 \text{ meV}(\text{nm})^{-3}$

Table 4.1: Terms used in the simulation of an antiferromagnet without magnetoelastic coupling, together with the relevant equations and parameter values.

4.1 Nucleation of Magnetic Domains in Antiferromagnets by the Magnetoelastic Coupling

Using the Eshelby Inclusion, discussed in the Background Information chapter, we can produce a strain field in our material, which is analytically verifiable. These inclusion defects, which are regions of defective material (as opposed to point defects), can arise naturally in a material, such as precipitates like in Fe-Cr alloys [76], or as a result, intentional or otherwise, of processes which alter the structure of the sample, such as ion implantation [77]. This strain field will elicit a magnetic effect due to the magnetoelastic coupling, particularly if the magnetoelastic coupling is strong in the material. We will investigate this effect in this chapter for antiferromagnetic materials, using it to nucleate magnetic domains, and investigating how it alters preexisting domain structures (i.e. an implanted magnetic domain wall), as well as how the alteration of important parameters affects both of the former.

4.1.1 Antiferromagnet without Magnetoelastic Coupling - 2D

In order for us to accurately assess the effect of the magnetoelastic coupling on our two dimensional antiferromagnet, we should first look at the result of a simulation where the magnetoelastic coupling is not present. This simulation included the following terms, shown in tabular format in Table 4.1.

We initialise the magnetisation vectors of the sublattices along the $(0.8, 0.6, 0)$ direction for the first sublattice and the $(-0.8, -0.6, 0)$ direction for the second sublattice. This is to avoid being in an unstable equilibrium with respect to the magnetocrystalline anisotropy; other than this, this selection is arbitrary. The result of this simulation, for a $100\text{nm} \times 100\text{nm}$ sample, is

4.1 Nucleation of Magnetic Domains in Antiferromagnets by the Magnetoelastic Coupling

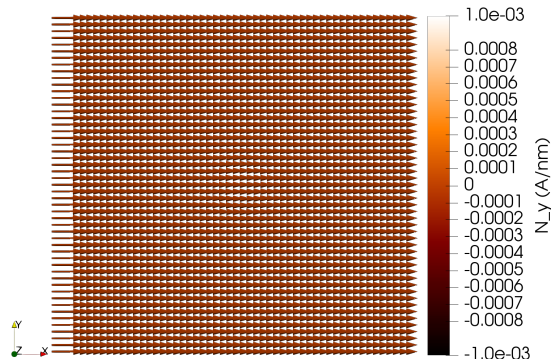


Figure 4.1: Néel vector profile for a 2D antiferromagnet simulation, where the magnetoelastic coupling is not present.

shown in Figure 4.1. We get that the Néel vector aligns along the x -axis as a result of the cubic anisotropy, as the x -axis is the closest easy axis to the initial condition. Now that we have the results of the simulation with no magnetoelastic coupling, we can examine the effect of adding an inclusion defect, together with the magnetoelastic coupling, has on the magnetic structure of the antiferromagnet.

4.1.2 Domain Nucleation by a Single Defect with Magnetoelastic Coupling

We implant a defect ($10\text{nm} \times 10\text{nm}$) in size, which would seek to expand up to 5% of its original dimensions in the absence of the surrounding material) in the centre of our sample, as shown in Chapter 2. Using [78], we select the values of the Young's modulus and Poisson's ratio as $1.58 \cdot 10^{11} \text{Jm}^{-3}$ and 0.38 respectively, values consistent with NiO [78]. We use NiO here as it is an archetypal collinear cubic antiferromagnet; generalisation to other crystal types is possible by modifying the elasticity tensor, however to generalise this to non-collinear antiferromagnets is not possible in our model, due to the manner in which we implemented the antiferromagnetic coupling (i.e. by coupled sublattices). We then add, in addition to the terms outlined in the previous subsection, the magnetoelastic coupling and the elastic energy minimisation (relevant to the spontaneous strain), with initial magnetostriction coefficients of $\lambda_{100} = -5.71 \cdot 10^{-5}$ and $\lambda_{111} = -2.86 \cdot 10^{-5}$. We run the simulation until we reach a point where the total residual changes by less than $10^{-6}\%$ between steps, the value of our steady state tolerance parameter. We then vary λ_{100} , in increments of $(2.86 \cdot 10^{-6}, 5\%$ of the original value) from $\lambda_{100} = 1.43 \cdot 10^{-5}$ to $\lambda_{100} = 1.14 \cdot 10^{-4}$, whilst keeping λ_{111} constant at its original value, rerunning the simulation for each increment.

4.1 Nucleation of Magnetic Domains in Antiferromagnets by the Magnetoelastic Coupling

For the weakest λ_{100} , we observe the Néel vector profile given in Figure 4.2. Here, we only see a small divergence from the pattern observed where no defect and magnetoelastic coupling is present (Figure 4.1). The magnetoelastic coupling combined with the defect only acts as a perturbation to the surrounding magnetic structure; the perturbation is insufficient to be stabilised by the magnetocrystalline anisotropy to create domains along the y -direction. Additionally, note that the pattern here has its maximum extent along the $(1, 1, 0)$, $(-1, 1, 0)$, $(-1, -1, 0)$ and $(1, -1, 0)$ directions, a result of the λ_{111} term becoming larger than the λ_{100} term.

For the strongest λ_{100} , we obtain the Néel vector profile observed in Figure 4.3. Here, we obtain an hourglass-shaped domain profile, with two large magnetic domains with Néel vectors along the y -direction emanating from the centre (where the defect is present) towards the top and bottom sides of the sample. Given that there is no other reason that these domains should be forming other than the magnetoelastic coupling, this is clear evidence of domain nucleation by the effect of the magnetoelastic coupling. To examine the effect that varying both of the magnetostriction coefficients has on the domain formation, we will perform two parameter sweeps (as outlined previously). To give a quantitative description of the extent of the domains, we will calculate the total area of material which contains magnetic domains along the y -direction for each simulation, then we will plot this against the relevant magnetostriction coefficient for that simulation. The way we will measure the domain area is by setting a threshold for the y -component of the Néel vector, after which it is considered to be belonging to the y -domain. The minimum requirement for this threshold would be that the normalised vector has to have a larger magnitude y -component than the other components, i.e. $|n_y| > |n_x|$ and $|n_y| > |n_z|$. Since all of the Néel vectors remain in the $x - y$ plane, we need only concern ourselves here with the former. This essentially gives us a minimum condition for the threshold of $1/\sqrt{2}$. For our purposes, we select a threshold of $|n_y| \geq 0.8$, after which this cell is considered to be part of the y -domain. To give an estimate in the error, we will also select thresholds of $|n_y| \geq 0.85$ (lower bound) and $|n_y| \geq 0.75$ (upper bound). Using Paraview [4], we then select the cells which fulfil this criteria, note the number of these cells, and multiply by the area per cell to find the total domain area.

We plot these values as shown in Figure 4.5. From this plot, we can notice multiple trends. Firstly, from the λ_{100} data, we have two critical points; the first, which we will call λ_n , occurs when nucleation of magnetic domains begins. The second, which we will call λ_c , occurs when the size of the domains skyrockets. After this point, the size of the domains steadily increases with increasing λ_{100} . Secondly, we have that altering the λ_{111} coefficient does not significantly

4.1 Nucleation of Magnetic Domains in Antiferromagnets by the Magnetoelastic Coupling

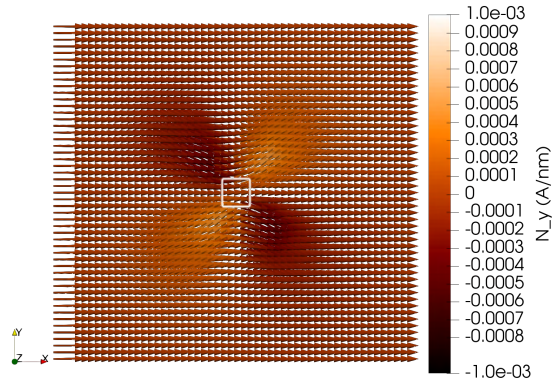


Figure 4.2: Néel vector profile of the 2D antiferromagnet with an inclusion defect located in the centre of the material and a magnetoelastic coupling is present, where we have a weaker λ_{100} term. The defect location is highlighted with a white outline.

alter the area of the domains. However, we observe from Figures 4.2 and 4.4, that whilst the primary domain behaviour is dictated by the λ_{100} term, if the λ_{111} is sufficiently strong it can rotate the orientation of the domains created. After demonstrating this, it was prudent to examine how breaking the centrosymmetry of the strain structure changes the shape of the domains and the ease of which they are nucleated. We will first do this by changing the position of the defect, to be closer to one of the edges, then by changing the geometry to the central defect such that the centrosymmetry of the strain is removed.

Domain Nucleation by a Single Defect Located at the Sample's Edge

We shifted the location of the single defect to be near the edge of the sample to remove the centrosymmetry of the strain, in this case we select the top-right edge (selected arbitrarily; the case for the other edges follows by symmetry). We expect that, by removing the centrosymmetry of the strain, this will make it easier to nucleate domains, requiring less magnetoelastic coupling strength. We then repeat the parameter sweep we conducted previously for the λ_{100} magnetostriction coefficient. Plotting this along with the previous case of a central defect, we get the plot shown in Figure 4.8. Firstly, we note that we do not appear to have a λ_c value for the offset defect curve, and the domains created are thus an order of magnitude smaller than the case for the central defect at all data points taken. Secondly, we have that the two values of λ_n are not inconsistent with each other. That is to say that having the defect present near the edge of the sample does not significantly make it easier to nucleate magnetic domains using

4.1 Nucleation of Magnetic Domains in Antiferromagnets by the Magnetoelastic Coupling

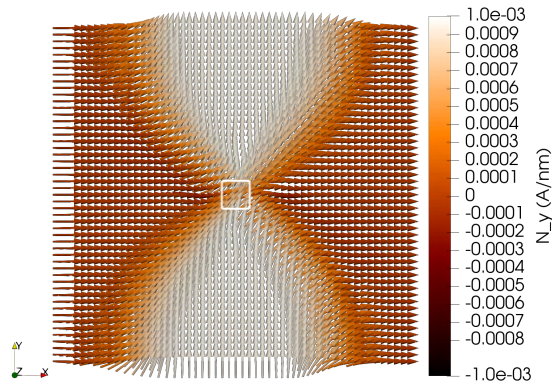


Figure 4.3: Néel vector profile of the 2D antiferromagnet with an inclusion defect located in the centre of the material and a magnetoelastic coupling is present, where we have a very strong λ_{100} term. The defect location is highlighted with a white outline.

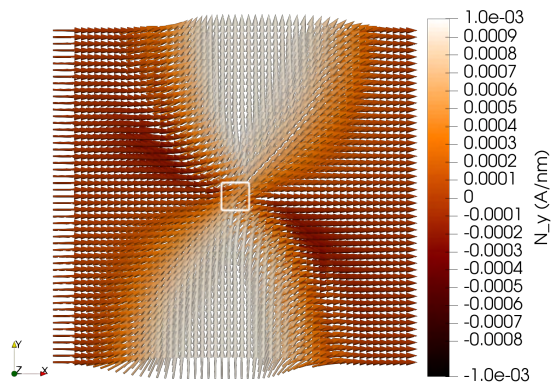


Figure 4.4: Néel vector profile of the 2D antiferromagnet with an inclusion defect located in the centre of the material and a magnetoelastic coupling is present, where we have a very strong λ_{111} term. The defect location is highlighted with a white outline.

4.1 Nucleation of Magnetic Domains in Antiferromagnets by the Magnetoelastic Coupling

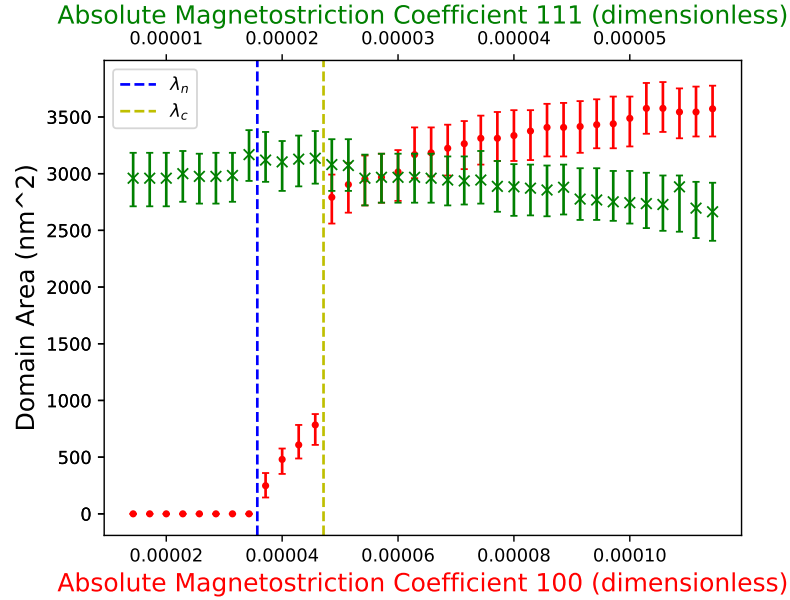


Figure 4.5: Graph of domain area versus both of the magnetostriction coefficients.

the magnetoelastic coupling, contrary to what we initially speculated. We will instead try to investigate if breaking the centrosymmetry by another method (by changing the geometry of the central defect) will make domain nucleation easier.

Domain Nucleation by a Single Rectangular Defect

To examine the effect changing the geometry of the central defect has on the nucleated domain structure, we will change the dimensions of the central defect from a square $10\text{nm} \times 10\text{nm}$ to the rectangular $25\text{nm} \times 4\text{nm}$. We then re-run the parameter sweep of the λ_{100} coefficient. The results of this sweep are depicted in graph form in Figure 4.11, with the Néel vector profiles output for the case of a rectangular defect shown in Figures 4.10 and 4.9 for a strong and weak magnetoelastic coupling respectively. From Figure 4.11, we can observe that we achieve a lower value of λ_n , hence it is easier to nucleate a magnetic domain with a rectangular defect, with respect to the magnetoelastic coupling strength required. The value of λ_c has also substantially decreased, showing large domain nucleation is easier with a rectangular defect compared to a square defect. Larger domains may also be achieved, as evidenced by the increase in maximal domain area achieved. These considerations, combined with the significant change in shape of the domains (evidenced by comparing Figure 4.10 with Figure 4.9), show that the

4.1 Nucleation of Magnetic Domains in Antiferromagnets by the Magnetoelastic Coupling

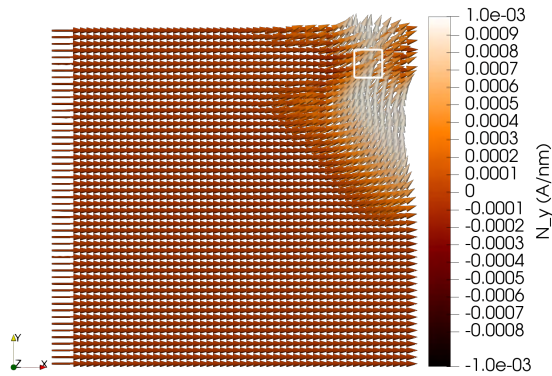


Figure 4.6: Néel vector profile for the offset defect case, where the defect is located at the top-right, where we have a very strong λ_{100} term. The defect location is highlighted with a white outline.

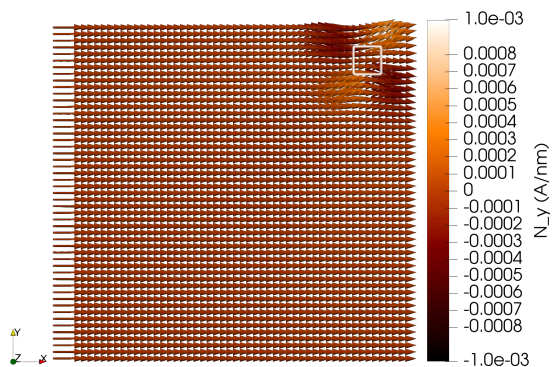


Figure 4.7: Néel vector profile for the offset defect case, where the defect is located at the top-right, where we have a weaker λ_{100} term. The defect location is highlighted with a white outline.

4.1 Nucleation of Magnetic Domains in Antiferromagnets by the Magnetoelastic Coupling

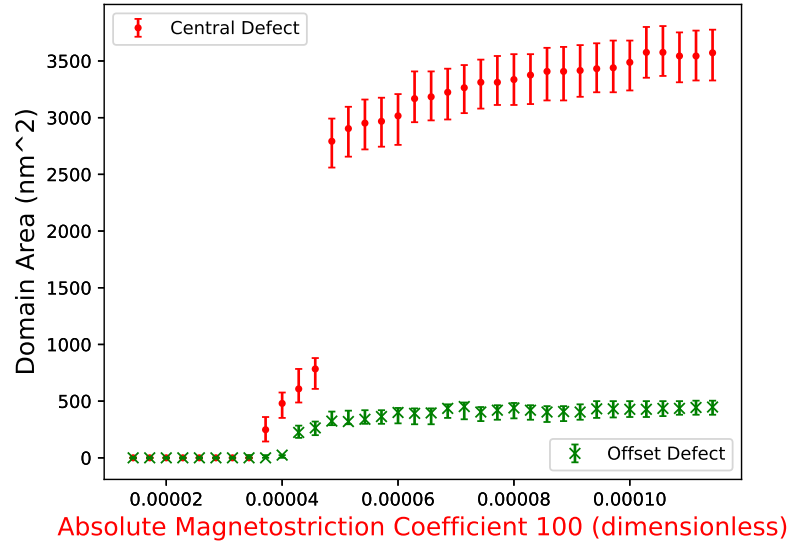


Figure 4.8: Graph of domain area versus the λ_{100} magnetostriction coefficient, for the case of a defect located at the centre of the material and the case of a defect located near the top-right of the material.

geometry of the defect can have major implications on the resultant domain formation. Another potentially important consideration is the defect's size; whether altering the size of the defect affects how easily they are nucleated (with respect to the magnetoelastic coupling strength) and the shape of the domains created, which we will examine in the following subsection.

Domain Nucleation by a Smaller Single Defect

We can also look at how the size of the central defects affects the magnetostriction necessary to nucleate the domains, and if they are able to reach the same extent as previous. We change the size of the central defect from $10\text{nm} \times 10\text{nm}$ to $8\text{nm} \times 8\text{nm}$ and $6\text{nm} \times 6\text{nm}$ separately. We then again re-run the parameter sweep of the λ_{100} coefficient. We plot these results, shown in Figure 4.12. From this, we can observe that, for the $6\text{nm} \times 6\text{nm}$ defect case, we have a significant increase in the values for λ_n , hence a large increase in the strength of magnetostriction necessary to nucleate domains. The $8\text{nm} \times 8\text{nm}$ case has the same approximate critical values, however the domain area of the nucleated domains is smaller for each λ_{100} value when compared to the $10\text{nm} \times 10\text{nm}$. This variance of the defect size with the magnetostriction coefficients necessary

4.1 Nucleation of Magnetic Domains in Antiferromagnets by the Magnetoelastic Coupling

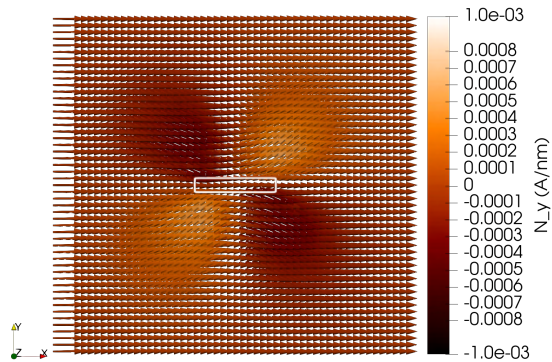


Figure 4.9: Néel vector profile result from the simulation where we have a single rectangular defect in the centre, where we have magnetoelastic coupling with a weak λ_{100} term. The defect location is highlighted with a white outline.

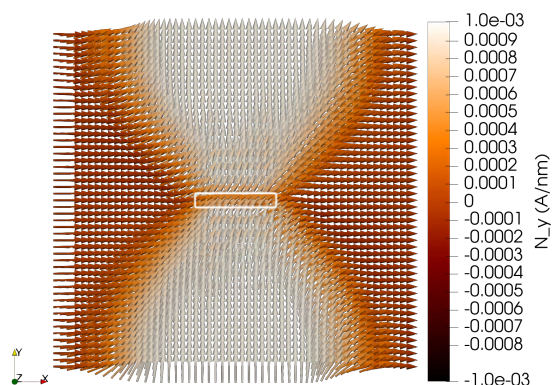


Figure 4.10: Néel vector profile result from the simulation where we have a single rectangular defect in the centre, where we have magnetoelastic coupling with a strong λ_{100} term. The defect location is highlighted with a white outline.

4.1 Nucleation of Magnetic Domains in Antiferromagnets by the Magnetoelastic Coupling

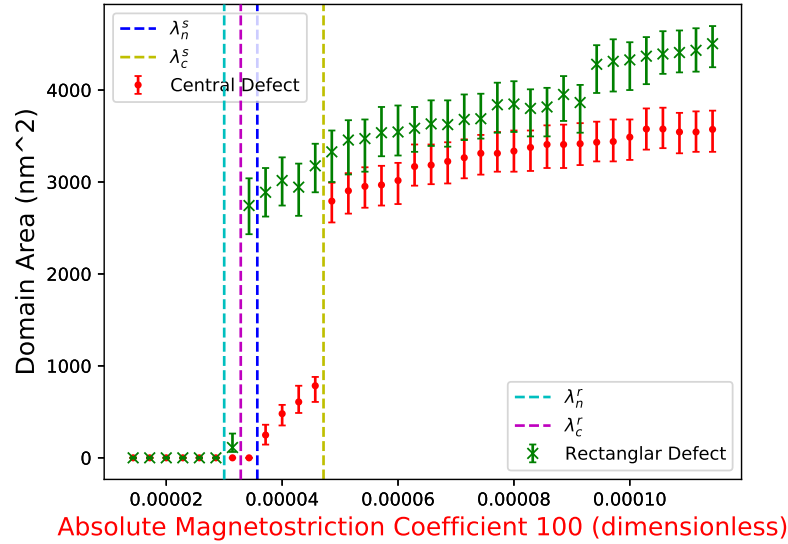


Figure 4.11: Graph of the domain area versus λ_{100} for the original square defect and for a rectangular defect.

to nucleate a domain and/or the size of the domains nucleated, combined with the fact we can impose defects and hence dictate the size of the defects, gives a potential pathway to measuring the magnetostriction λ_{100} coefficient, though this would require further investigation to exploit successfully. Given that we have conclusively proven that a single inclusion defect has when combined with a magnetoelastic coupling can nucleate magnetic domains in antiferromagnets, it would be interesting to see how multiple magnetic domains interact when created in this way, and how it would relate to the underlying strain structure. To this end, we implemented this in our software package, and recorded the results in the following.

4.1.3 Interaction of Domains Nucleated by Two or More Defects

To examine how domains created by defects in antiferromagnets interact with each other, we will vary the type of defects interacting (defects which would seek to expand or contract if surrounding material was not present; we will refer to these in shorthand by tensile and compressive defects respectively) as well as the distance they are separated by. We will start this analysis by considering two tensile defects.

4.1 Nucleation of Magnetic Domains in Antiferromagnets by the Magnetoelastic Coupling

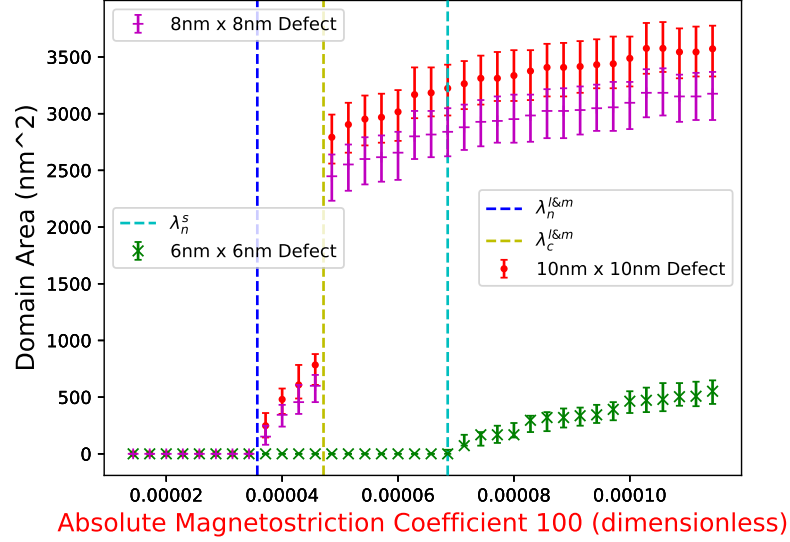
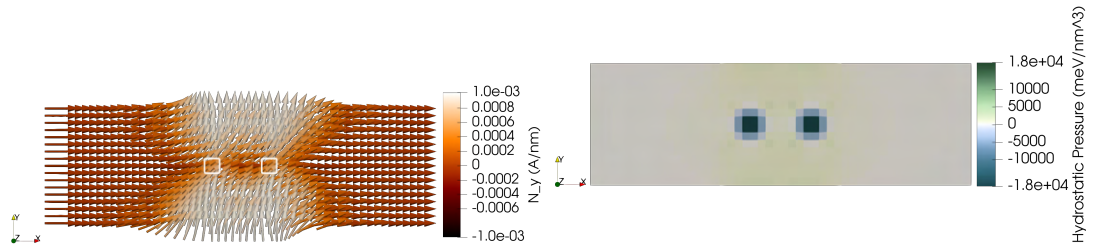


Figure 4.12: λ_{100} parameter sweep for a $10\text{nm} \times 10\text{nm}$ defect, a $8\text{nm} \times 8\text{nm}$ defect and a $6\text{nm} \times 6\text{nm}$ defect, all located at the centre of the material.

Interaction of Domains Created by Two Separate Tensile Defects

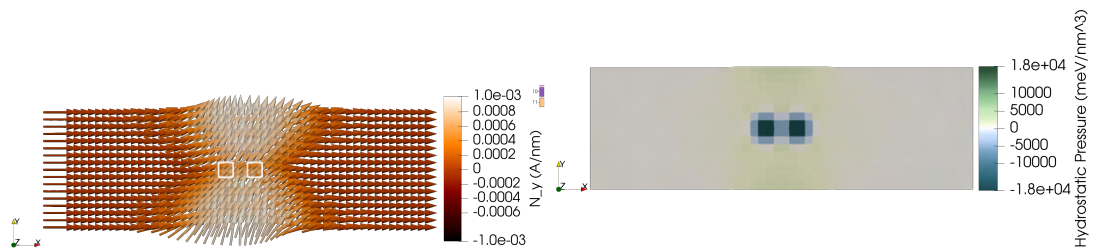
We select a rectangular sample for our analysis, of dimensions $125\text{nm} \times 40\text{nm}$, and select a uniform mesh of 50×16 cells, for cells of uniform area of 6.25 square nanometres. We then implant two defects at a distance from each other (measured from defect centres), and vary this between simulations, from 10nm to 100nm , in increments of 5nm . We include the intra- and inter-lattice exchanges (Equations 1.1 and respectively 1.2), cubic anisotropy (Equation 1.4), and elastic energy minimisation (Equation 2.20) as before, with the same parameter values, aswell as the magnetoelastic coupling (Equation 1.19). We conduct two separate runs of simulations for comparison, one with $\lambda_{100} = -5.71 \cdot 10^{-5}$ and the other with $\lambda_{100} = -1.14 \cdot 10^{-4}$. The areas of the domains are calculated by setting a threshold value for the y -component of the Néel vector, then calculating the total area of the cells within this threshold; this will give us an idea of the degree to which the domains are interacting. The results of this are plotted in Figure 4.17, together with the values of the domain areas of two non-interacting domains (obtained by finding the domain area nucleated by a single central defect, then doubling it). The domains created appear to interact weakly; the domains, when very close ($10\text{nm} - 35\text{nm}$), combine to form two distinct domains at the top and bottom (observable in Figure 4.13).

4.1 Nucleation of Magnetic Domains in Antiferromagnets by the Magnetoelastic Coupling



(a) Néel vector profile for the case of two tensile defects, for a separation distance of 20nm. (b) Hydrostatic pressure for the case of two tensile defects, for a separation distance of 20nm.

Figure 4.13: Néel vector profile and hydrostatic pressure values for the case of two tensile defects, for a separation distance of 20nm. The defect locations are highlighted with a white outline.



(a) Néel vector profile for the case of two tensile defects, for a separation distance of 10nm. (b) Hydrostatic pressure for the case of two tensile defects, for a separation distance of 10nm.

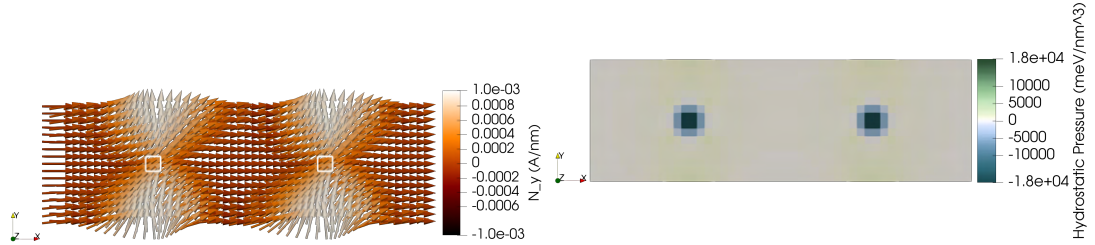
Figure 4.14: Néel vector profile and hydrostatic pressure values for the case of two tensile defects, for a separation distance of 10nm. The defect locations are highlighted with a white outline.

This as opposed to four distinct domains for the non-interacting defect case; initially, this is likely due to direct overlap of domains (hence the perceivable reduction in domain area at around 10nm separation, shown in Figure 4.14).

Then, the strain field caused by both defects expands the width of the domains to the point where the neighbouring domains along the x -direction combine to form one larger domain, giving a larger total domain area. Above this separation distance, from around 40nm to 85nm the domains act, to a large degree, independently; there is little interaction between them, as seen in Figure 4.15.

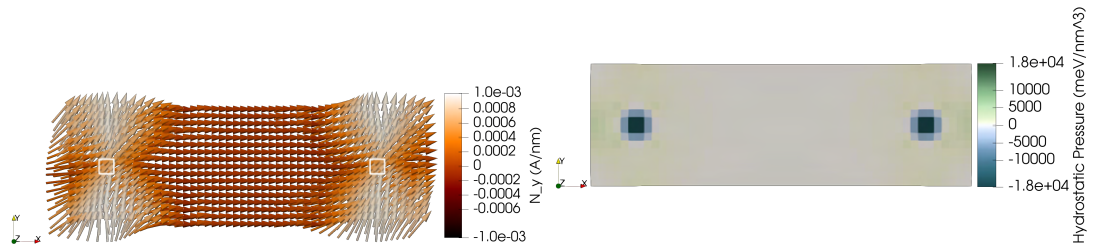
Once we reach a separation distance of 90nm and above, we start to observe edge effects, as the defects are sufficiently close to the edge that we observe truncation in the domains formed,

4.1 Nucleation of Magnetic Domains in Antiferromagnets by the Magnetoelastic Coupling



(a) Néel vector profile for the case of two tensile defects, for a separation distance of 60nm. (b) Hydrostatic pressure for the case of two tensile defects, for a separation distance of 60nm.

Figure 4.15: Néel vector profile and hydrostatic pressure values for the case of two tensile defects, for a separation distance of 60nm. The defect locations are highlighted with a white outline.



(a) Néel vector profile for the case of two tensile defects, for a separation distance of 95nm. (b) Hydrostatic pressure for the case of two tensile defects, for a separation distance of 95nm.

Figure 4.16: Néel vector profile and hydrostatic pressure values for the case of two tensile defects, for a separation distance of 95nm. The defect locations are highlighted with a white outline.

giving a reduced total domain area, like in Figure 4.16.

We observe similar behaviour for the case where the λ_{100} coefficient is doubled. Given that we observed that a compressive defect leads to domain “lobes” along the x -direction, we expect that we will observe increased interaction between domains caused by these defects, so we will investigate this in the following.

Interaction of Domains Created by Two Separate Compressive Defects

We then conducted the same analysis as outlined previously for the case of two compressive defects. We can define certain regions of interest in the plot in Figure 4.22, as we did for the previous case, beginning with the case of the initial value of λ_{100} . Firstly, we from 10nm –

4.1 Nucleation of Magnetic Domains in Antiferromagnets by the Magnetoelastic Coupling

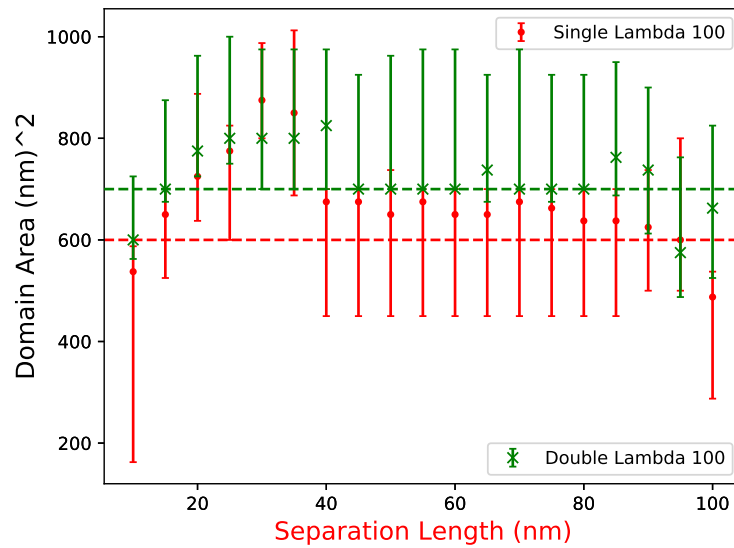
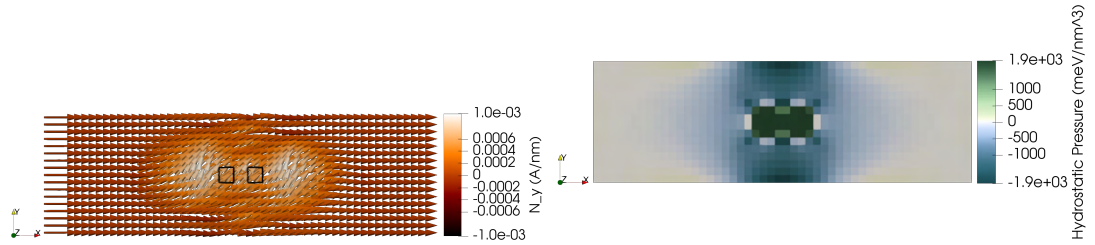


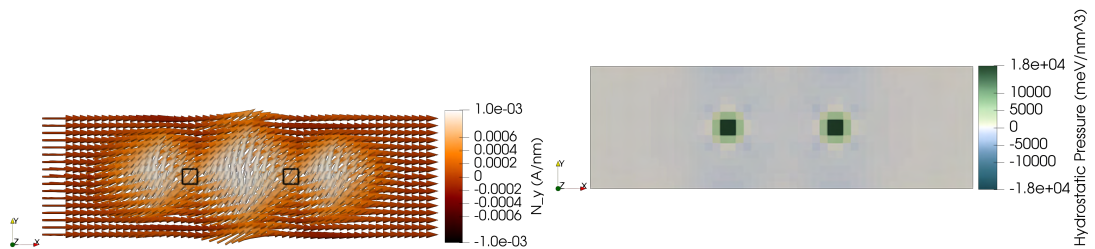
Figure 4.17: Plot of domain area versus the separation distance of the two tensile defects, for two different values of λ_{100} . The error bars are given by varying the threshold by which we verify if a domain is present. The horizontal bars are given by the expected domain area of two non-interacting defects; the red bar represents the domain area of two non-interacting defects for the original value of λ_{100} , and the green bar represents the same for the doubled value of λ_{100} .

4.1 Nucleation of Magnetic Domains in Antiferromagnets by the Magnetoelastic Coupling



(a) Néel vector profile for the case of two compressive defects, for a separation distance of 10nm. (b) Hydrostatic pressure for the case of two compressive defects, for a separation distance of 10nm.

Figure 4.18: Néel vector profile and hydrostatic pressure values for the case of two compressive defects, for a separation distance of 10nm. The defect locations are highlighted with a black outline.



(a) Néel vector profile for the case of two compressive defects, for a separation distance of 35nm. (b) Hydrostatic pressure for the case of two compressive defects, for a separation distance of 35nm.

Figure 4.19: Néel vector profile and hydrostatic pressure values for the case of two compressive defects, for a separation distance of 35nm. The defect locations are highlighted with a black outline.

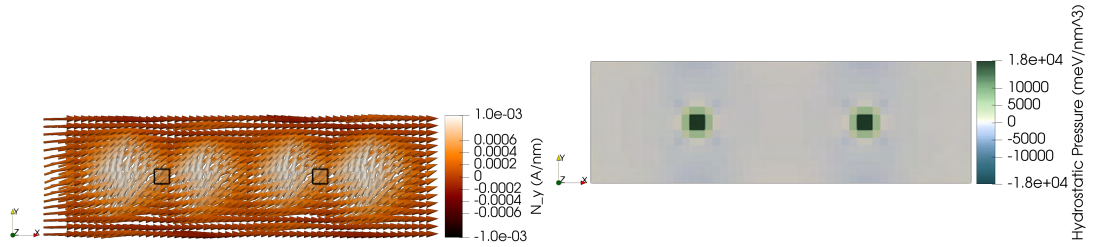
15nm we have the domains interacting by neutralising the lobes nearest to each other, forming a single dual-lobed domain structure reminiscent of a domain expected by a single larger defect, like in Figure 4.18.

Moving further apart, from 20nm – 50nm these nearest-lobes instead interfere constructively, forming a tri-lobe structure, with the central lobe eventually becoming large enough to compensate and more for the loss of the previous two individual lobes, shown in Figure 4.19.

Then, from 55nm – 60nm, the domains become near non-interacting, with domain areas only slightly above non-interacting values, like in Figure 4.20.

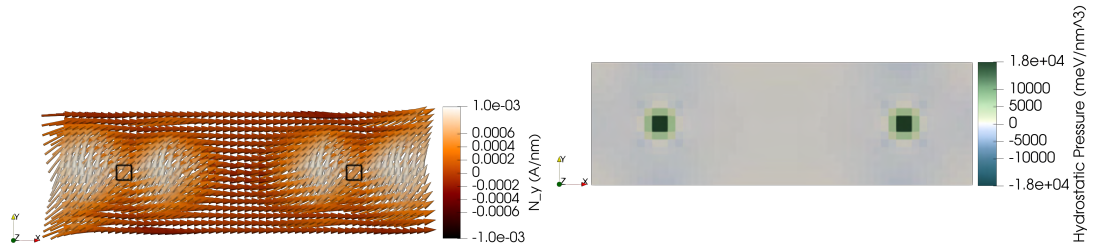
Finally, from 65nm onwards, we start to observe increased edge effects, initially aiding domain nucleation but as material becomes more scarce at one side of both defects, we see a decrease

4.1 Nucleation of Magnetic Domains in Antiferromagnets by the Magnetoelastic Coupling



(a) Néel vector profile for the case of two compressive defects, for a separation distance of 55nm. (b) Hydrostatic pressure for the case of two compressive defects, for a separation distance of 55nm.

Figure 4.20: Néel vector profile and hydrostatic pressure values for the case of two compressive defects, for a separation distance of 55nm. The defect locations are highlighted with a black outline.



(a) Néel vector profile for the case of two compressive defects, for a separation distance of 80nm. (b) Hydrostatic pressure for the case of two compressive defects, for a separation distance of 80nm.

Figure 4.21: Néel vector profile and hydrostatic pressure values for the case of two compressive defects, for a separation distance of 80nm. The defect locations are highlighted with a black outline.

in overall domain area, such as in Figure 4.21.

As opposed to the previous analysis with two tensile defects, here we observe significantly different behaviour for an increased value of the λ_{100} . Instead of the domains becoming near non-interacting around the separation distance of 60nm, we get a massive shift in the domain structure, with the y -domains expanding to take up more than a third of the whole sample, as observed in Figure 4.23. This large increase shows the domains created by the defects are interacting very strongly, as opposed to the more marginal changes experienced when using two tensile defects. Given we have a large constructive interaction observed here (and to a lesser degree, for the case of two tensile defects), we expect that having a compressive and tensile defect interact will exhibit destructive, or elimination, behaviour when interacting. We will now

4.1 Nucleation of Magnetic Domains in Antiferromagnets by the Magnetoelastic Coupling

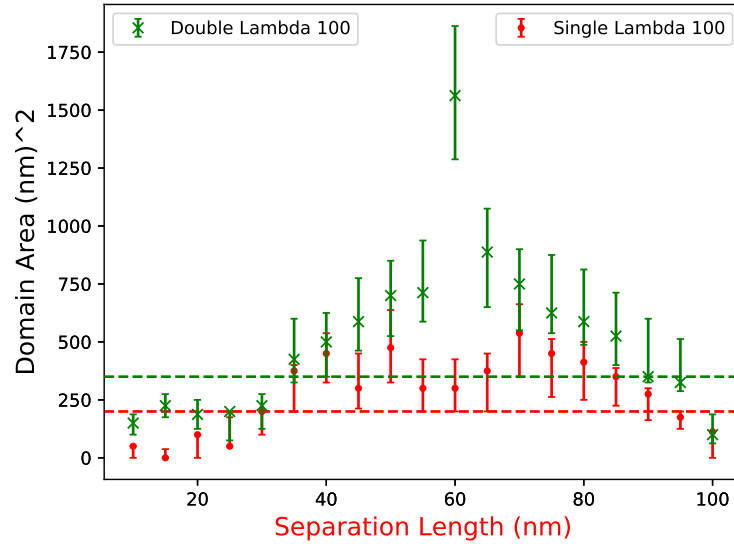


Figure 4.22: Graph of domain area versus separation distance of two compressive defects, for the cases of our standard magnetostriction coefficient and the case where it is doubled. The horizontal lines represent the total domain area which would be represented by two non-interacting defects, for both of the magnetostriction coefficient cases. The bars represent the same as described in Figure 4.17.

test this hypothesis, as well as examining the asymmetry of this interaction (by exchanging the location of the compressive and tensile defect).

Interaction of Domains Created by a Separate Tensile Defect and a Compressive Defect

We repeat our previous analysis for the case where we have both a compressive and tensile defect. We predict we will observe some elimination behaviour between the domains created by these two defects. The results of this analysis are plotted in Figure 4.27. We find that below 70nm separation in the $\lambda_{100} = -5.71 \cdot 10^{-5}$ case, we observe elimination behaviour, like in Figure 4.24.

The domains then become near non-interacting for a separation of 70nm, shown in Figure 4.25. After this separation distance, we start to observe our now-familiar edge effects, like in Figure 4.26.

Curiously, for the case where $\lambda_{100} = -1.14 \cdot 10^{-4}$, 60nm, we have that this “critical” separation

4.1 Nucleation of Magnetic Domains in Antiferromagnets by the Magnetoelastic Coupling

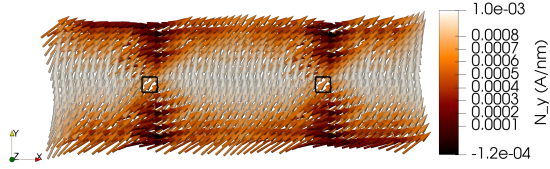
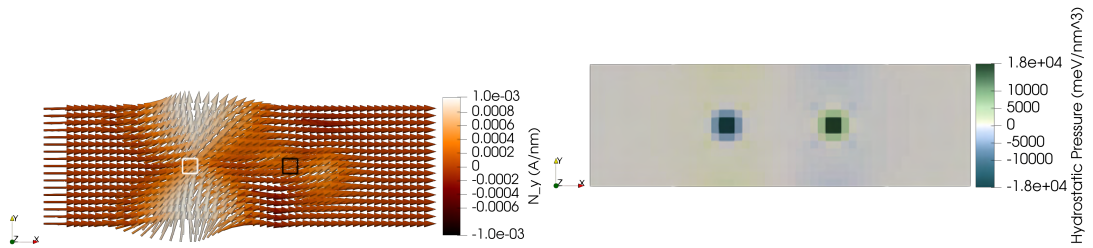
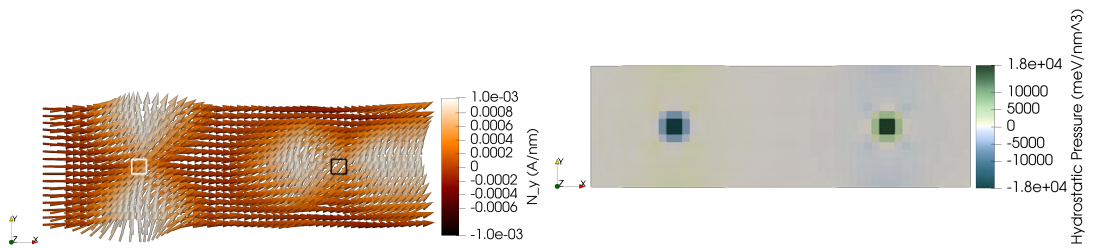


Figure 4.23: Néel vector profile, for the case of two compressive defects separated by 60nm, and a λ_{100} value of $1.14 \cdot 10^{-4}$. The defect locations are highlighted with a black outline.



(a) Néel vector profile for the case of a tensile and a compressive defect, for a separation distance of 35nm. (b) Hydrostatic pressure for the the case of a tensile and a compressive defect, for a separation distance of 35nm.

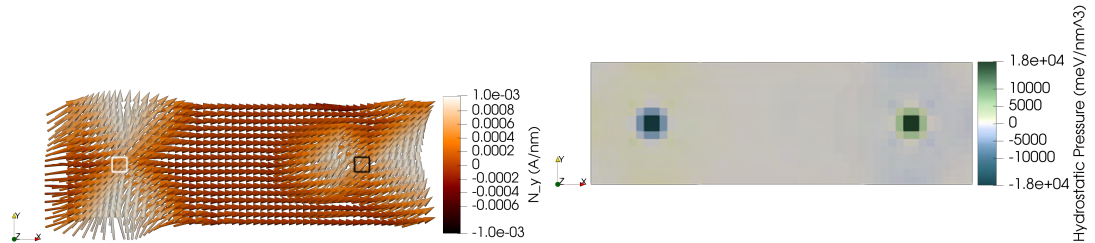
Figure 4.24: Néel vector profile and hydrostatic pressure values for the case of a tensile and a compressive defect, for a separation distance of 35nm. The defect locations are highlighted with a white outline for the tensile defect and a black outline for the compressive defect.



(a) Néel vector profile for the case of a tensile and a compressive defect, for a separation distance of 70nm. (b) Hydrostatic pressure for the the case of a tensile and a compressive defect, for a separation distance of 70nm.

Figure 4.25: Néel vector profile and hydrostatic pressure values for the case of a tensile and a compressive defect, for a separation distance of 70nm. The defect locations are highlighted with a white outline for the tensile defect and a black outline for the compressive defect.

4.1 Nucleation of Magnetic Domains in Antiferromagnets by the Magnetoelastic Coupling



(a) Néel vector profile for the case of a tensile and (b) Hydrostatic pressure for the the case of a tensile a compressive defect, for a separation distance of and a compressive defect, for a separation distance 85nm. of 85nm.

Figure 4.26: Néel vector profile and hydrostatic pressure values for the case of a tensile and a compressive defect, for a separation distance of 85nm. The defect locations are highlighted with a white outline for the tensile defect and a black outline for the compressive defect.

distance, where the domains become near non-interacting , is now 60nm; this variance of this “critical” distance of the defects with the λ_{100} magnetostriction coefficient has the potential to be used for the measurement of this magnetostriction coefficient, a process that hitherto has been a difficult and not necessarily accurate process.

Given these findings, it is important to look at the symmetry of this elimination interaction. By repeating our previous analysis for the case where the positions of the compressive and tensile defects are switched, this will allow us to assess the symmetry of the elimination interaction between domains caused by these defects, with respect to the interchanging of defect types. The results of this analysis are plotted in Figure 4.28. Comparing to Figure 4.27, we see minimal difference in the observed curves, especially for the $\lambda_{100} = -5.71 \cdot 10^{-5}$ case. This demonstrates that this interaction is relatively symmetric, hence a theoretical evaluation of the magnetostriction coefficient λ_{100} could be undertaken for either scenario. After looking in detail at the interaction of the domains caused by two inclusion defects, it is worth examining how multiple domains caused by defects interact more generally.

Domain Patterns Created by Arrays of Defects

In order to investigate how domains nucleated by these inclusion defects interact more generally, we decided to implement patterns of defects inspired by the sides of a six-sided dice (D6). This is not intended as a qualitative or quantitative analysis of how the arrangement and type of

4.1 Nucleation of Magnetic Domains in Antiferromagnets by the Magnetoelastic Coupling

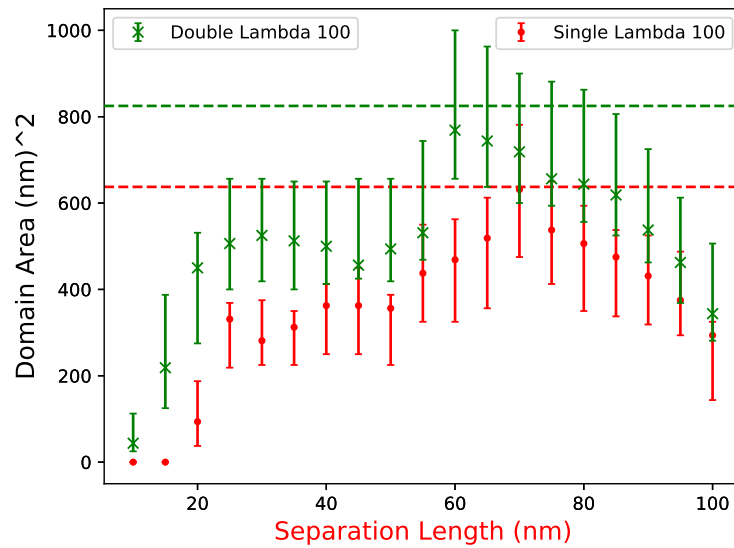


Figure 4.27: Graph of domain area versus separation distance of the tensile defect and the compressive defect, for the cases of our standard magnetostriction coefficient and the case where it is doubled. The horizontal lines represent the total domain area which would be represented by two non-interacting defects, for both of the magnetostriction coefficient cases.

4.1 Nucleation of Magnetic Domains in Antiferromagnets by the Magnetoelastic Coupling

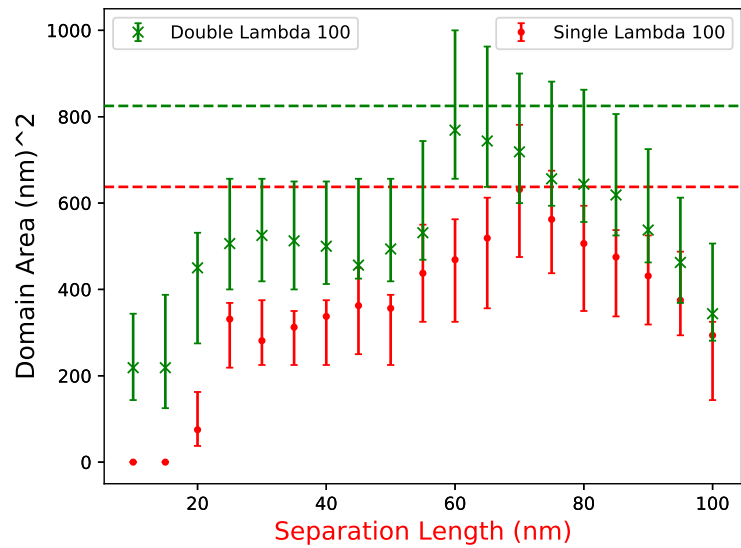
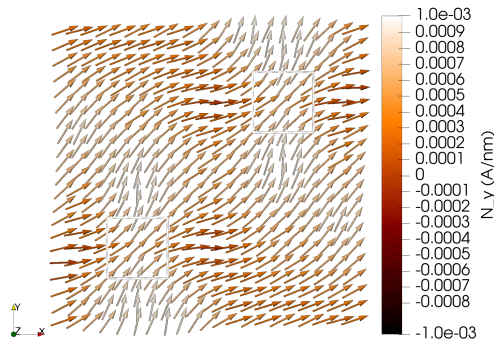


Figure 4.28: Graph of domain area versus separation distance of the tensile defect and the compressive defect, for the cases of our standard magnetostriction coefficient and the case where it is doubled. Here, we have switched the positions of the tensile and compressive defects relative to Figure 4.27.

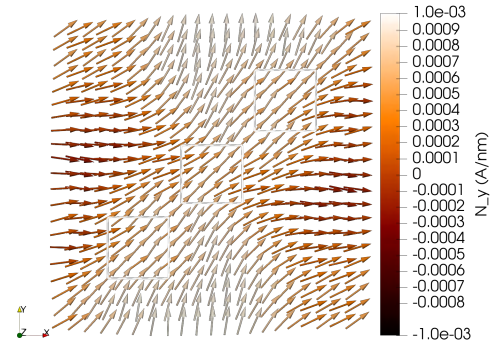
4.1 Nucleation of Magnetic Domains in Antiferromagnets by the Magnetoelastic Coupling

defects present in the material affects the domain structure, rather as an exhibition of the variety of domain structures you can obtain by changing these variables. The size of the samples used is $50\text{nm} \times 50\text{nm}$, with individual defects measuring $10\text{nm} \times 10\text{nm}$. $\lambda_{100} = -5.71 \cdot 10^{-5}$; all other parameters are as they were for previous subsections. The Néel vector patterns we observed for the dice faces 2 through 6, for the case where all defects are tensile, are pictured in Figure 4.29. For comparison, we also have the case for the same defect patterns, where some defects have been converted to compressive defects, shown in Figure 4.30 (the defects converted are specified by the relevant caption). We obtain a wide variety of domain patterns depending on the underlying defect structure, demonstrating that a desired domain pattern for our antiferromagnet is likely achievable by the selection of an appropriate defect structure. Given that these defects are able to be implanted to materials (for example by ion implantation [77]), we have demonstrated in this chapter not only that defects are the key to understanding the antiferromagnetic domain structure, but that antiferromagnetic domains can be selectively created by utilising said mechanism. This chapter has explored how the defect structure in an antiferromagnet is responsible for the formation of antiferromagnetic domains, and how these domains interact with one another. It is our hope that this work will inspire future experiments on the effect of the magnetoelastic effect of inclusion defects and dislocations on the antiferromagnetic domain structure, which will in turn verify the accuracy of our model. However, what we have not explored is how the defect structure, when present, affects an already-present non-trivial domain structure. We will explore this in the following chapter.

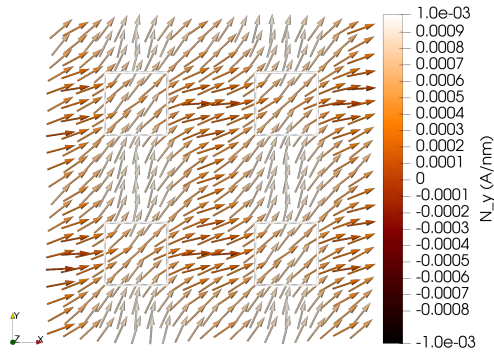
4.1 Nucleation of Magnetic Domains in Antiferromagnets by the Magnetoelastic Coupling



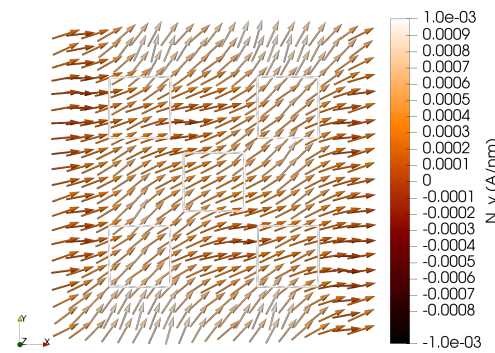
(a) Néel vector profile for the “2” side dice defect profile.



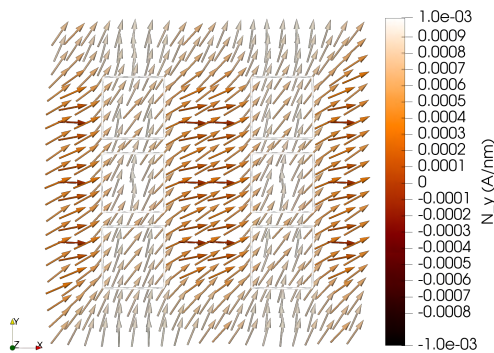
(b) Néel vector profile for the “3” side dice defect profile.



(c) Néel vector profile for the “4” side dice defect profile.



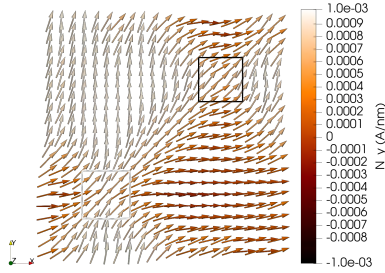
(d) Néel vector profile for the “5” side dice defect profile.



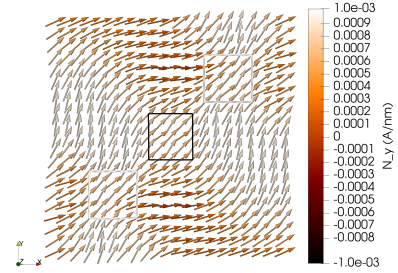
(e) Néel vector profile for the “6” side dice defect profile.

Figure 4.29: Néel vector profiles for corresponding defect patterns resembling those of a standard six-sided dice (D6). The defect locations are highlighted with a white outline.

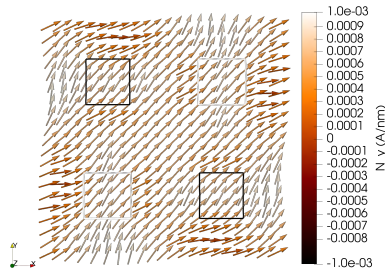
4.1 Nucleation of Magnetic Domains in Antiferromagnets by the Magnetoelastic Coupling



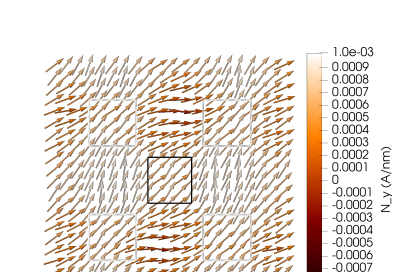
(a) Néel vector profile for the “2” side dice defect profile, where the top-right defect is compressive.



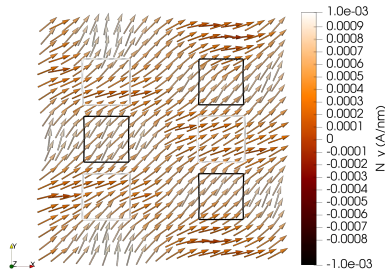
(b) Néel vector profile for the “3” side dice defect profile, where the central defect is compressive.



(c) Néel vector profile for the “4” side dice defect profile, where the top-left and bottom-right are compressive.



(d) Néel vector profile for the “5” side dice defect profile, where the central defect is compressive.



(e) Néel vector profile for the “6” side dice defect profile, where the top-right, bottom-right and centre-left defects are compressive.

Figure 4.30: Néel vector profiles for corresponding defect patterns resembling those of a standard six-sided dice (D6), where we switch certain defects to be compressive, as specified in the individual captions. The defect locations are highlighted with a white outline for tensile defects and a black outline for compressive defect.

4.1 Nucleation of Magnetic Domains in Antiferromagnets by the Magnetoelastic Coupling

Summary

- We implant an inclusion defect into a cubic antiferromagnet which has a magnetoelastic coupling. We then run our phase field magnetic simulation on this sample, yielding clear evidence of magnetic domain formation.
- By calculating the area of the domains nucleated, we were able to assess the impact on domain nucleation from altering the shape, size and location of the defect. We found that domain nucleation required less magnetoelastic coupling strength for a rectangular versus square defect, that domain nucleation was made more difficult by having a smaller defect, and that domain nucleation was not made easier by having a defect located closer to the edge.
- Having observed the effect a single defect has on the domain structure, we look at the interaction between domains caused by two defects, and how their separation distance affects this interaction. We observe domain elimination when a compressive and a tensile defect interact; for two of either type, with increasing separation distance, we get domain overlap, before constructive interference, after which the domains become near non-interacting, indicating that using multiple defects can help us pattern domain patterns that are desired.
- We further express the interaction between the domains caused by these defects by providing an array of defect patterns and providing the resulting Néel vector profiles.

CHAPTER 5

Magnetoelastic Interaction of Inclusion Defects
with Domain Walls

5.1 Interaction of Multiple Inclusion Defects and Their Interaction with Domain Walls

Term	Equation	Parameter Values
Intra-lattice Exchange	Equation 1.1	$A = 3.97 \text{ meV}(\text{nm})^{-1}$
Inter-lattice Exchange	Equation 1.2	$J = 57.62 \text{ meV}(\text{nm})^{-3}$
Cubic Anisotropy	Equation 1.4	$K_1 = 0.25 \text{ meV}(\text{nm})^{-3}$, $K_2 = 0.12 \text{ meV}(\text{nm})^{-3}$
Magnetisation Constraint	Equation 1.62	$\lambda = 1.00 \cdot 10^6 \text{ meV}(\text{nm})^{-3}$
Elastic Energy Minimisation	Equation 2.20	$Y = 1.58 \cdot 10^{11} \text{ Jm}^{-3}$, $\nu = 0.38$
Magnetoelastic Coupling	Equation 1.19	$\lambda_{100} = -5.71 \cdot 10^{-5}$, $\lambda_{111} = -2.86 \cdot 10^{-5}$

Table 5.1: Terms used in the simulation of an antiferromagnet with magnetoelastic coupling, together with the relevant equations and parameter values.

5.1 Interaction of Multiple Inclusion Defects and Their Interaction with Domain Walls

Since we have established that the magnetoelastic coupling can have a large impact on the domain structure of antiferromagnets by nucleating magnetic domains, it is prudent to examine how the magnetoelastic coupling affects a pre-existing domain structure, i.e. a domain wall. We will examine the influence a single defect has on a domain wall, how the magnetostriction coefficients affect this influence, how multiple defects affect the domain wall, and finally how varying the location of the defect relative to the domain wall affects its magnetic structure. We will begin by looking at the foremost two of these.

5.1.1 Interaction of a Single Defect with Magnetoelastic Coupling with a Domain Wall

We begin by establishing our $100\text{nm} \times 100\text{nm}$ antiferromagnetic sample, with a 50×50 cell mesh. We include the terms shown in Table 5.1 in our simulations. We apply Dirichlet boundary conditions at the left and right side of the material. These conditions were $m_{1y} = 1$, $m_{2y} = -1$ and $m_{1x} = 0$, $m_{2x} = 0$ on the left side of the material, such that $n_y = 1$, $n_x = 0$, and for the right side of the material, we have the conditions $m_{1y} = 0$, $m_{2y} = 0$ and $m_{1x} = 1$, $m_{2x} = -1$, such that $n_y = 0$, $n_x = 1$. This will lead to the formation of a domain wall along the sample's central y -axis, with two rectangular domains on either side. We then impose a central inclu-

5.1 Interaction of Multiple Inclusion Defects and Their Interaction with Domain Walls

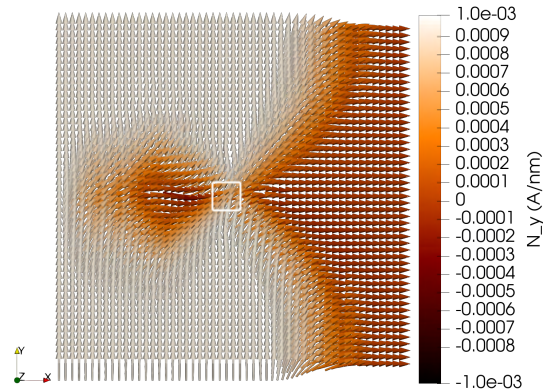
sion defect of dimensions $10\text{nm} \times 10\text{nm}$, in the same fashion as we did for Subsection 4.1.2 for Chapter 4. For a λ_{100} value of $-1.14 \cdot 10^{-4}$ and λ_{111} value of $-2.86 \cdot 10^{-5}$, we get the Néel vector profiles observed in Figure 5.1, for a tensile defect (Figure 5.1a) and a compressive defect (Figure 5.1b). We see that the domain wall has significantly changed shape; as opposed to the two rectangular domains separated by a domain wall that would naïvely be expected, we have an expansion of one domain at the expense of the other and a penetration of one domain into the other. This strong interaction represents something that needs to be taken into account when making devices with these materials; here a relatively small fraction of defective material is enough to completely disfigure the domain wall profile. Given this fact, it is prudent for us to explore how this disfigurement is affected by the strength of the magnetostriction coefficients.

Firstly, we look at the case for a higher λ_{111} coefficient. We select the values of $\lambda_{100} = \lambda_{111} = -5.71 \cdot 10^{-5}$ for this. The other material parameters remain unchanged. The results of this is shown in Figure 5.2. We can observe highly asymmetric behaviour, when comparing to the profiles observed in Figure 5.1; the domain enclave is offset with respect to the centre compared to previous, and the domain travels to different extents either vertical side of this enclave. We can thus deduce the asymmetric part of the domain wall disfigurement likely stems from the λ_{111} term of the magnetoelastic coupling. To examine this, and to get an idea of the strength of magnetoelastic coupling required to cause this domain wall deformation, we will look at much lower values of the λ_{100} and λ_{111} magnetostriction coefficients.

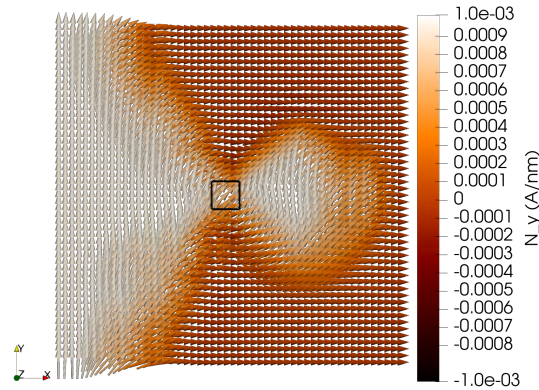
Firstly, we will begin by lowering the λ_{111} value to $-7.14 \cdot 10^{-6}$ and keeping $\lambda_{100} = -5.71 \cdot 10^{-5}$, we re-run the simulations and get the Néel vector profiles shown in Figure 5.4. We observe that we get the penetration of one domain into the other, similar to Figure 5.1, showing this is the influence of the λ_{100} term. Additionally, the domain expansion/contraction along the top and bottom is much more symmetric, providing additional evidence that it is the influence of the λ_{111} term that causes the asymmetry. We can further verify both of these points by looking at the scenario where the λ_{100} coefficient has been reduced in magnitude.

We will now continue this analysis by reducing the value of the λ_{100} coefficient, such as to evaluate if a lower value will significantly alter the disfigurement of the domain wall. The results of this are shown in Figure 5.3. Firstly, we notice the lack of either domain penetrating into the other; this gives us the indication that this part of the behaviour is governed by the

5.1 Interaction of Multiple Inclusion Defects and Their Interaction with Domain Walls



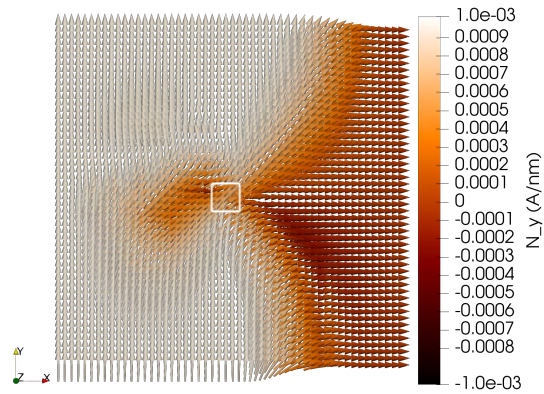
(a) Néel vector profile for a domain wall interacting with a central tensile defect, for the case of $\lambda_{100} = -1.14 \cdot 10^{-4}$.



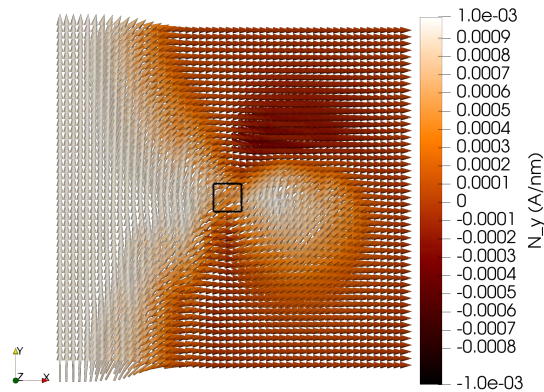
(b) Néel vector profile for a domain wall interacting with a central compressive defect, for the case of $\lambda_{100} = -1.14 \cdot 10^{-4}$.

Figure 5.1: Néel vector profiles for a central defect (of different types) interacting with a domain wall, with a strong magnetoelastic coupling, with $\lambda_{100} = -1.14 \cdot 10^{-4}$. The defect locations are highlighted with a white outline for the tensile defect and a black outline for the compressive defect.

5.1 Interaction of Multiple Inclusion Defects and Their Interaction with Domain Walls



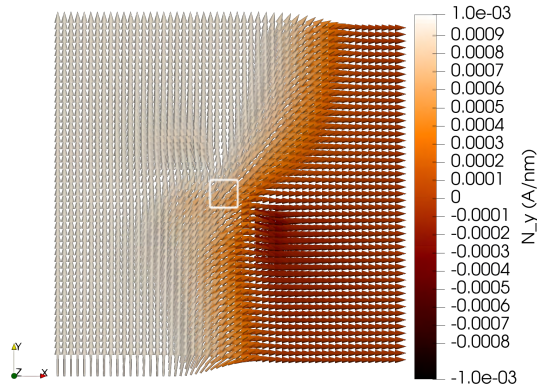
(a) Néel vector profile for a domain wall interacting with a central tensile defect, for the case of $\lambda_{111} = -5.71 \cdot 10^{-5}$.



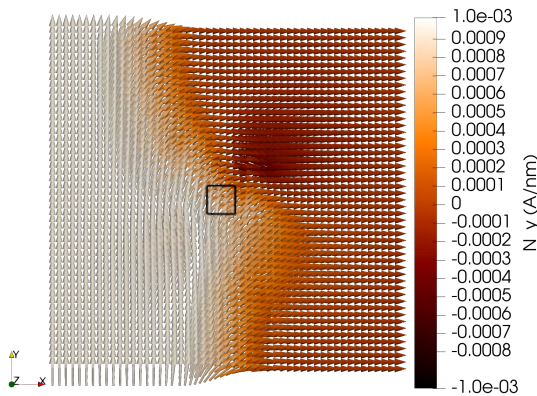
(b) Néel vector profile for a domain wall interacting with a central compressive defect, for the case of $\lambda_{111} = -5.71 \cdot 10^{-5}$.

Figure 5.2: Néel vector profiles for a central defect (of different types) interacting with a domain wall, with a strong magnetoelastic coupling, with $\lambda_{111} = -5.71 \cdot 10^{-5}$. The defect locations are highlighted with a white outline for the tensile defect and a black outline for the compressive defect.

5.1 Interaction of Multiple Inclusion Defects and Their Interaction with Domain Walls



(a) Néel vector profile for a domain wall interacting with a central tensile defect, for the case of $\lambda_{100} = -1.43 \cdot 10^{-5}$.



(b) Néel vector profile for a domain wall interacting with a central compressive defect, for the case of $\lambda_{100} = -1.43 \cdot 10^{-5}$.

Figure 5.3: Néel vector profiles for a central defect (of different types) interacting with a domain wall with $\lambda_{100} = -1.43 \cdot 10^{-5}$. The defect locations are highlighted with a white outline for the tensile defect and a black outline for the compressive defect.

5.1 Interaction of Multiple Inclusion Defects and Their Interaction with Domain Walls

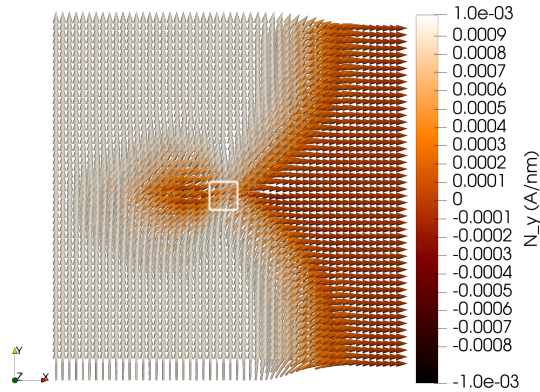
λ_{100} term. Secondly, we observe asymmetric lengthwise growth/decay of the domains along the top and bottom of the sample, as well as perceivable perturbations in the domains near the centre of the material, indicating that the λ_{111} term is responsible for the asymmetric part of the magnetic behaviour (as it has a greater relative influence here due to the reduction in the λ_{100} coefficient). Given that we have observed such strong behaviour for a single defect, we wished to investigate whether, and how, these effects are affected by having multiple defects present.

5.1.2 Interaction of Multiple Defects with Magnetoelastic Coupling with a Domain Wall

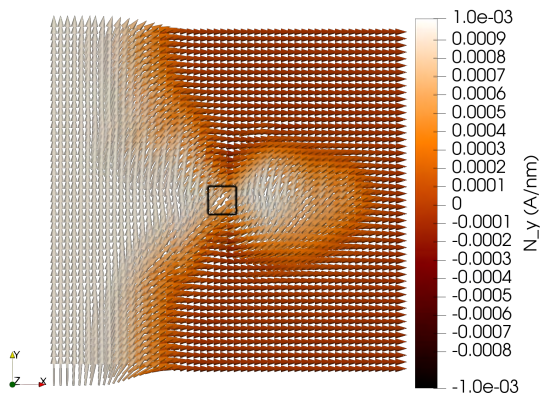
To begin this analysis, we will consider the case of one tensile defect and one compressive defect, with their centres located 20nm from the centre of the sample to the left and right respectively. We retain the phase field model terms used previously in this chapter. With this setup, the simulation outputs the Néel vector profiles shown in Figure 5.5, where we have used a λ_{100} coefficient of $-1.43 \cdot 10^{-5}$ for Figure 5.5a and $-1.14 \cdot 10^{-4}$ for Figure 5.5b respectively. Additionally, the penetration of one domain into the other observed in Figure 5.5b is more extensive than that observed for the single defect simulations. Contrary to the expected elimination behaviour we might naïvely expect given what we observed in Figure 4.27, we have that the interaction of these two defects has more of an effect on the domain wall than an individual defect, not less. This indicates that, where a domain wall is present, we cannot rely on elimination behaviour between defects to mitigate their impact on the magnetic behaviour. To investigate further, we can vary the types of defect present and their order, similar to the analysis conducted in the Subsection 4.1.3 of Chapter 4.

We can, first of all, reverse the location of the tensile and compressive defect to be on the right and left of the sample, respectively. All other terms, parameters and distances remain unchanged. The Néel vector profiles from these simulations are shown in Figure 5.6, for the case of $\lambda_{100} = -1.43 \cdot 10^{-5}$ and $\lambda_{100} = -1.14 \cdot 10^{-4}$. The case for Figure 5.5a is a near mirror-image of the previously found profile in Figure 5.5a, which would indicate this interaction has some symmetry with respect to the arrangement of the inclusion defects included in the sample. However, the profile we find in Figure 5.6b casts this implication into doubt; whilst the central domain pattern is not dissimilar, we have almost wave-like behaviour of the Néel vector profile

5.1 Interaction of Multiple Inclusion Defects and Their Interaction with Domain Walls



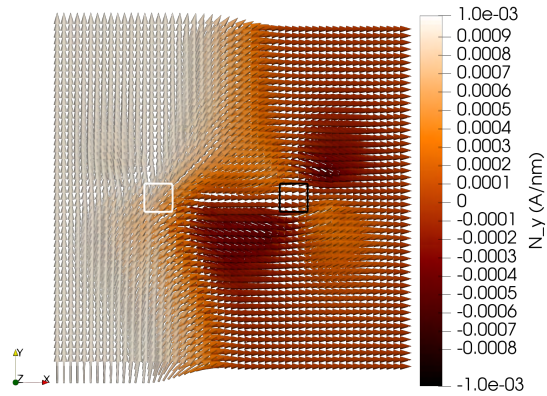
(a) Néel vector profile for a domain wall interacting with a central tensile defect, for the case of $\lambda_{111} = -7.14 \cdot 10^{-6}$.



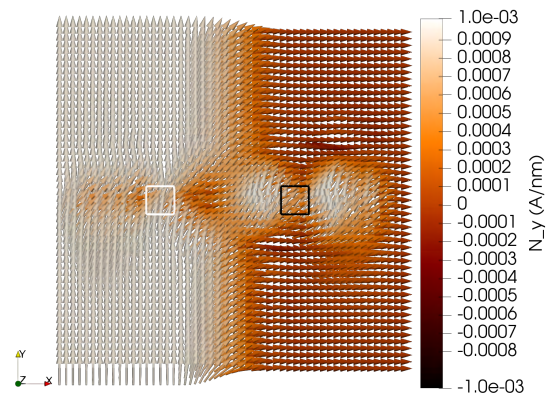
(b) Néel vector profile for a domain wall interacting with a central compressive defect, for the case of $\lambda_{111} = -7.14 \cdot 10^{-6}$.

Figure 5.4: Néel vector profiles for a central defect (of different types) interacting with a domain wall with $\lambda_{111} = -7.14 \cdot 10^{-6}$. The defect locations are highlighted with a white outline for the tensile defect and a black outline for the compressive defect.

5.1 Interaction of Multiple Inclusion Defects and Their Interaction with Domain Walls



(a) Néel vector profile for a domain wall interacting with a tensile defect on the left and a compressive defect on the right, for the case of $\lambda_{100} = -1.43 \cdot 10^{-5}$.



(b) Néel vector profile for a domain wall interacting with a tensile defect on the left and a compressive defect on the right, for the case of $\lambda_{100} = -1.14 \cdot 10^{-4}$.

Figure 5.5: Néel vector profiles for a tensile defect and a compressive defect interacting with a domain wall, with differing λ_{100} coefficients. The defect locations are highlighted with a white outline for a tensile defect and a black outline for a compressive defect.

5.1 Interaction of Multiple Inclusion Defects and Their Interaction with Domain Walls

along the lengthwise direction, a departure from what we observed before. This highlights that the arrangement of the defects can have a radical impact on the domain structure, as well as the type. Furthermore, we can look to the cases where we have the same type of defect present to see if the previous behaviour for the single defect case is enhanced or reduced by this.

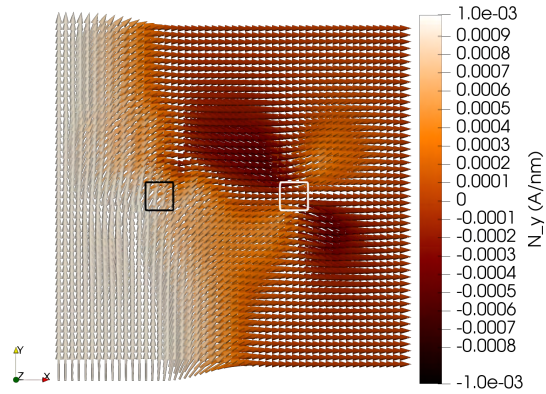
Firstly, let us look at the case for two tensile defects. The Néel vector profiles for these simulations can be viewed in Figure 5.7. The penetration behaviour, first observed in Figure 5.1, has been significantly extended here in Figure 5.7b; simultaneously, the y -domain has expanded, whilst the x -domain has penetrated deeper into it. This interesting behaviour confirms our earlier hypothesis, whereby having more than one defect may amplify their effects. The case for a weaker magnetoelastic coupling, shown in Figure 5.7a, shows similar, but significant, alteration to the domain wall profile as with previous iterations with defect arrays using this coupling strength. We will now look to the final case, that of two compressive defects causing domains that interact with the domain wall.

The Néel vector profiles we obtain in the simulations with two compressive defects are shown in Figure 5.8. We observe, for the stronger magnetoelastic coupling, the same expanded penetration behaviour as for the two tensile defect simulation, but here the x -domain is significantly expanded, and the penetration behaviour goes from right to left rather than vice-versa, indicating this interaction is symmetric with respect to the type of defect present. For a weaker magnetoelastic coupling, we still observe a strong interaction with the domain wall, albeit not as pronounced. We can now look to how altering the location of a single defect changes the shape and position of the domain wall, which may be useful for tailoring the magnetic structure in antiferromagnets to our liking.

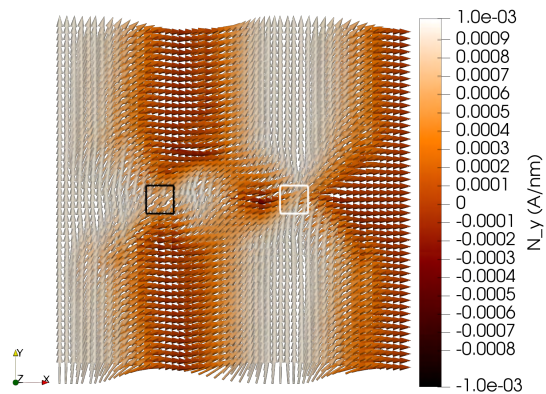
5.1.3 Interaction of a Domain Wall with a Single Defect at Variable Distance

Our sample dimensions are $200\text{nm} \times 100\text{nm}$, with our defect being $10\text{nm} \times 10\text{nm}$. We implant a domain wall by imposing initial conditions of $m_{1x} = \tanh(\pi(x + 100)/100)$ and $m_{1y} = 1/\cosh(\pi(x + 100)/100)$ for the magnetisation vector of the first sublattice, and $m_{2x} = -\tanh(\pi(x + 100)/100)$ and $m_{2y} = -1/\cosh(\pi(x + 100)/100)$ for the magnetisation vector of the second sublattice. We chose these initial conditions because not only would these give a 90° degree domain wall as required, but the unit magnetisation constraint is also adhered to. The phase field model terms are the same as used previously in this chapter.

5.1 Interaction of Multiple Inclusion Defects and Their Interaction with Domain Walls



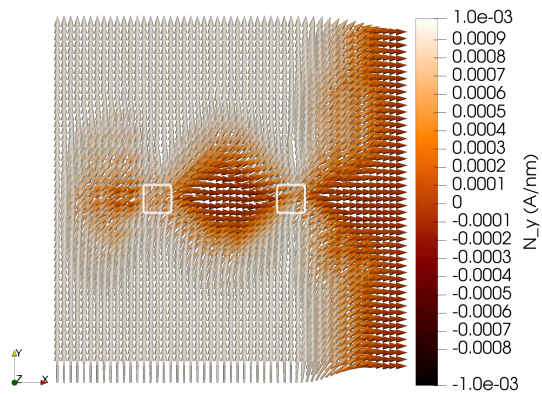
(a) Néel vector profile for a domain wall interacting with a tensile defect on the right and a compressive defect on the left, for the case of $\lambda_{100} = -1.43 \cdot 10^{-5}$.



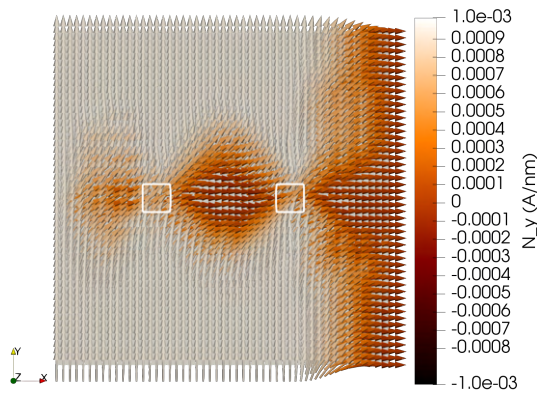
(b) Néel vector profile for a domain wall interacting with a tensile defect on the right and a compressive defect on the left, for the case of $\lambda_{100} = -1.14 \cdot 10^{-4}$.

Figure 5.6: Néel vector profiles for a compressive defect and a tensile defect interacting with a domain wall, with differing λ_{100} coefficients. The defect locations are highlighted with a white outline for a tensile defect and a black outline for a compressive defect.

5.1 Interaction of Multiple Inclusion Defects and Their Interaction with Domain Walls



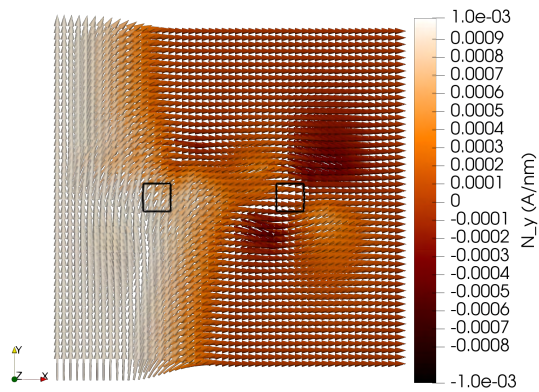
(a) Néel vector profile for a domain wall interacting with a tensile defect on the left and right, for the case of $\lambda_{100} = -1.43 \cdot 10^{-5}$.



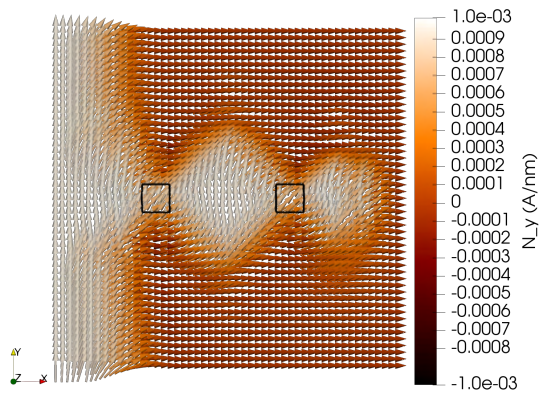
(b) Néel vector profile for a domain wall interacting with a tensile defect on the left and right, for the case of $\lambda_{100} = -1.14 \cdot 10^{-4}$.

Figure 5.7: Néel vector profiles for two tensile defects interacting with a domain wall, with differing λ_{100} coefficients. The defect locations are highlighted with a white outline.

5.1 Interaction of Multiple Inclusion Defects and Their Interaction with Domain Walls



(a) Néel vector profile for a domain wall interacting with an compressive defect on the left and right, for the case of $\lambda_{100} = -1.43 \cdot 10^{-5}$.



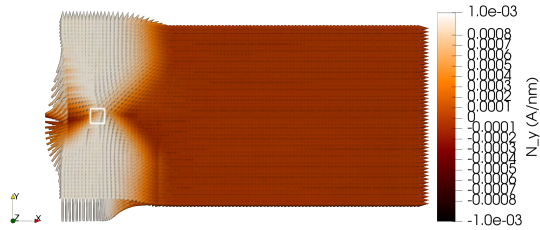
(b) Néel vector profile for a domain wall interacting with an compressive defect on the left and right, for the case of $\lambda_{100} = -1.14 \cdot 10^{-4}$.

Figure 5.8: Néel vector profiles for two compressive defects interacting with a domain wall, with differing λ_{100} coefficients. The defect locations are highlighted with a black outline.

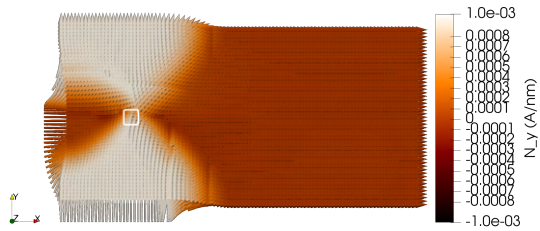
5.1 Interaction of Multiple Inclusion Defects and Their Interaction with Domain Walls

The distance of the defect, measured from the centre of the sample to the centre of the defects, is then altered between simulations, from -80nm to 80nm , in increments of 20nm . The Néel vector patterns from these simulations are displayed in Figures 5.9, 5.10 and 5.11. We can see that, where the defect is close to the domain wall, we observe a significant deformation of the domain wall, with the defect acting to increase the size of the left-most domain, before, where the defect is 40nm to the left of centre, the domain is split almost in two, where the top-half (approximate) of the left-most domain is lost. Eventually, the domains caused by the defects cease to interact so obviously with the domain wall, instead merely distorting the edges at best, before becoming near non-interacting at worst, when the defect is furthest to the right. This demonstrates that, if a domain wall expansion is desired, a defect can be placed near the domain wall to achieve this effect. Conversely, the effect can be mitigated by ensuring no defects are near the domain wall. This must then be taken into consideration when engineering such devices with antiferromagnets, something which we hope our work can assist with along with future experimental work.

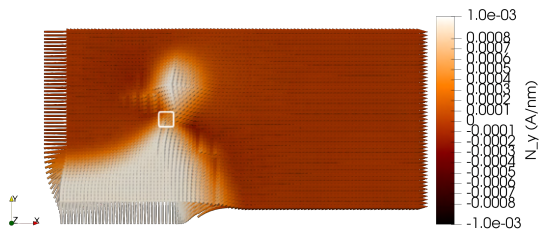
5.1 Interaction of Multiple Inclusion Defects and Their Interaction with Domain Walls



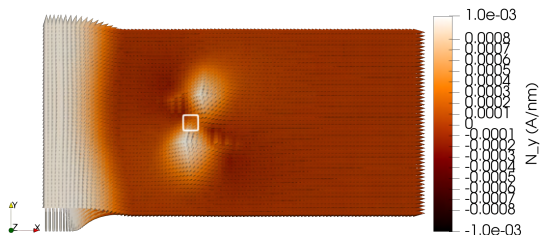
(a) Néel vector profile for a domain wall with a defect at $x = -80\text{nm}$ with respect to the center of the sample.



(b) Néel vector profile for a domain wall with a defect at $x = -60\text{nm}$ with respect to the center of the sample.



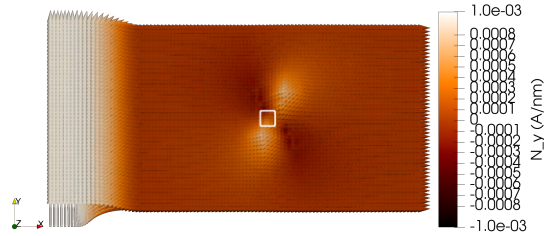
(c) Néel vector profile for a domain wall with a defect at $x = -40\text{nm}$ with respect to the center of the sample.



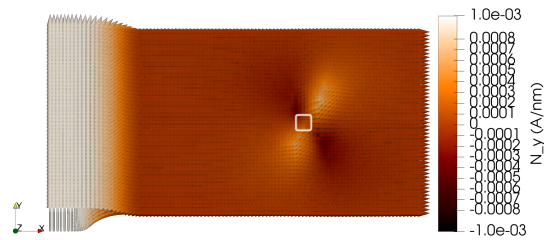
(d) Néel vector profile for a domain wall with a defect at $x = -20\text{nm}$ with respect to the center of the sample.

Figure 5.9: Néel vector profiles for defects in the negative x half of the material with respect to the centre, where a domain wall is already present in the sample. The defect locations are highlighted with a white outline.

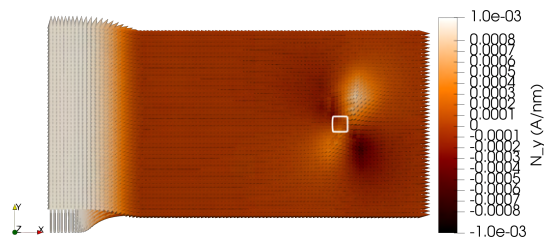
5.1 Interaction of Multiple Inclusion Defects and Their Interaction with Domain Walls



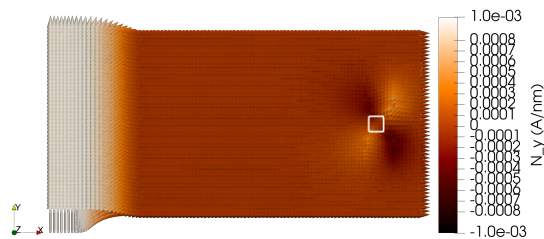
(a) Néel vector profile for a domain wall with a defect at $x = 20$ nm with respect to the center of the sample.



(b) Néel vector profile for a domain wall with a defect at $x = 40$ nm with respect to the center of the sample.



(c) Néel vector profile for a domain wall with a defect at $x = 60$ nm with respect to the center of the sample.



(d) Néel vector profile for a domain wall with a defect at $x = 80$ nm with respect to the center of the sample.

Figure 5.10: Néel vector profiles for defects in the negative x half of the material with respect to the centre, where a domain wall already exists in the sample (by initial conditions). The defect locations are highlighted with a white outline.

5.1 Interaction of Multiple Inclusion Defects and Their Interaction with Domain Walls

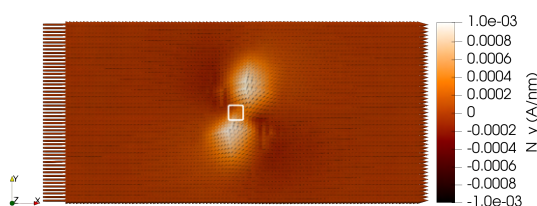


Figure 5.11: The missing case from Figures 5.9 and 5.10, that of a central defect with a domain wall (initial condition). The defect location is highlighted with a white outline.

Summary

- Having examined the magnetic effect of inclusion defects on uniformly magnetised antiferromagnets with magnetoelastic coupling in the previous chapter, we then examined this effect in antiferromagnets which are non-uniformly magnetised. We did this by encouraging a domain wall to form by using boundary conditions, then investigating how having a defect(s) present affects this.
- We started by looking at the case of a single defect; for a strong magnetoelastic coupling, and for both defect types, we observe one domain expanding into the other along the top or bottom (with some asymmetry), whilst also being penetrated along the centre. The λ_{100} appears to govern the domain growth along the top and bottom, as well as the penetration behaviour, and the λ_{111} governs the asymmetry of the interaction. The interaction appears to be symmetric with regards to the defect type changing.
- The effects of multiple defects on a domain wall can then be considered. We found that, contrary to what we found in the previous chapter, there was no elimination behaviour between the two different types of domains; there was a significant effect on the domain wall even in this case. Having more than one of the same type of defect, the domains expand further, and the penetration goes deeper.
- Another important consideration is with regards to the location of the defect with regards to the domain wall. Initialising a domain wall in the sample using initial conditions, we altered the location of the defect, and observed the results. Far from the domain wall, the effects are relatively minimal; getting closer to the domain wall, we first notice a small asymmetry in the domain wall, before the domain wall completely changes shape, the domain wall then reforms and is nearly split in two, and then the domains return to near original position but retaining this changed shape.

CHAPTER 6

Conclusions

6.1 Conclusions

We started this work with the objective of creating a software package to examine the magnetic effect of magnetoelasticity on antiferromagnets. Via the use of phase field modelling, we have achieved this aim. In this thesis, we have described how the phase field model operates at a basic level and the basics of magnetism theory, including the origination of ferromagnetism and antiferromagnetism. We discussed the theory of linear elasticity, and its expansion to explain the origin of the magnetoelastic coupling. Using the theory of linear elasticity, we explained and derived the strain and stress fields of inclusion defects and crystalline dislocations. Applying this knowledge, we implemented magnetic simulations with our software package using the ferromagnetic coupling and magnetocrystalline anisotropy, with verification coming from domain wall length analysis. Using the spin-flop and spin-flip transitions as verification, we then built on this to implement the antiferromagnetic coupling. Using the partial differential equation solver MOOSE's preexisting functionality, we then added inclusion defects into antiferromagnetic samples and calculated the strain/stress fields they produced.

We can then combined this with the magnetoelastic coupling to assess whether this combination is capable of nucleating a magnetic domain(s). This is indeed the case, demonstrating the critical role the magnetoelastic coupling has on domain formation. We then took this analysis further, examining how the nucleated domains are affected by changes in the magnetostriction coefficients, the geometry of the defect, its size, and where the defect is located in the sample. Altering the magnetostriction coefficients, increasing λ_{100} gives two critical values: λ_n , where domains first begin to be nucleated, and λ_c , where the nucleated domains massively increase in area. Altering λ_{111} yields little change in the domain area, but does alter the domain orientations. Altering the defects shape from square to rectangle (breaking the previous symmetry), found it required less magnetoelastic coupling strength to nucleate a magnetic domain, and have it expand. Contrary to what was expected, having the domain closer to the edge of the sample (thus breaking the previous symmetry again) did not make domain nucleation require less of a strong magnetoelastic coupling. Having a smaller defect entails having a larger magnetoelastic coupling in order to nucleate domains, as expected. We can then look to how domains caused by multiple defects interact with each other. Interestingly, we observe elimination behaviour between domains caused by different types of defect (expanding and contracting). For two expanding defects, we have an interaction between their created domains also, with the two initially overlapping, then constructively interfering, before becoming non-interacting with increasing separation distance. We see the same case with two contracting

defects; however, for a very strong magnetoelastic coupling, we get that at a critical separation distance, the y -domain (nucleated by our defects) becomes the dominant domain in the sample. To further illustrate the close ties between the defects and the nucleated domains, and the diversity of Néel vector profiles we can obtain, we also applied varying arrays and types of defect and observe their effect on the magnetic behaviour.

Having observed the effect that defects have combined with the magnetoelastic coupling on uniformly magnetised antiferromagnets, we then proceeded to examine how it affects an already-present non-trivial domain structure. We did this by encouraging a domain wall by using boundary conditions, then examining how this domain wall is altered by the presence of an inclusion defect. The effects we observed were large and certainly non-trivial; from deformation of the domain wall, to a massive reduction in sizes of individual domains and penetration effects of one domain into another. We also examined how altering the defects location with respect to the domain wall affected this interaction; we achieved interesting results indicating the domains could be stunted/expanded due to the influence of the defect depending on its location. These findings highlight the importance of examining the mechanical structure of these materials when considering their usefulness in data storage devices.

By using a phase field model, we successfully created a software package capable of numerically simulating the magnetic effect of magnetoelasticity on antiferromagnets. The use of the phase field model enabled us to avoid the considerations of precession dynamics, enabling us to explore this effect on larger samples (100nm upwards) without massively increased computational cost. Our package, drawing on inspiration from analytical work in the field, provides a never-before-seen way of numerically modelling magnetoelasticity in antiferromagnets in an accessible plug-in-and-play way, with a modular model based on a pre-existing mechanical underpinning. Using our model, we have produced results which assert that the magnetoelastic coupling is the driving force behind the formation of magnetic domains in antiferromagnets, and demonstrated the massive effect defects can have on the magnetic structure of antiferromagnets, particularly with respect to the deformation of domain walls. Furthermore, we gave results that indicate how we could use inclusion defects to pattern the domain structure we require into an antiferromagnetic material. We believe that, going forward, we have provided a platform on which to explore the rich nature of the magnetoelastic interaction in future works, and help provide information with regards to any future manufacture of data storage devices utilising these materials.

6.2 Future Work

Even though our work makes the numerical examination of magnetoelasticity in antiferromagnets, it is also important to acknowledge its shortcomings. In this work, we only considered the case of colinear cubic antiferromagnets. Of course, this does not encompass all antiferromagnets, hence our model lacks generality in this way. If we were to look to expanding the functionality to non-cubic, non-colinear systems, four main issues would arise; changes to the magnetocrystalline anisotropy, the elastic behaviour, the magnetoelastic coupling and the antiferromagnetic exchange. The elasticity consideration of having a non-cubic structure would not be a major issue for our package; the elasticity tensor only needs to be modified and the appropriate coefficients entered, which is trivial. As long as there is an applicable free energy density expression for the magnetocrystalline anisotropy, inserting this into the phase field model is also trivial. The relevant magnetoelastic coupling free energy density expression can then be derived from either pseudo-elasticity considerations or from the magnetocrystalline anisotropy, as outlined in Chapter 1. The main issue would more likely come from the adaptation to non-colinear antiferromagnets, from implementing the antiferromagnetic coupling, which we believe is possible but would require further work.

Additionally, in this work the case for a perfect antiferromagnet is the only one considered. In reality, we may encounter other antiferromagnets which have a non-zero net magnetisation, such as those affected by the Dzyaloshinskii-Moriya interaction, which causes a "parasitic" net magnetisation to occur [79]. This leads to a magnetostatic interaction, which cannot be implemented in our model as of yet. By adding a magnetostatic functionality into our model, these antiferromagnetic materials with "parasitic" magnetisation would be able to be accurately modelled, as well as ferrimagnetic and ferromagnetic materials. The pathway to achieve this may be by utilising the magnetic scalar potential ϕ and calculating its gradient to find the magnetostatic field, together with the magnetostatic energy density functional, to accurately simulate magnetostatics in our phase field model.

In considering the generality of our model, we must also consider the type of defects examined. In this thesis, we only considered the case for Eschelby-type inclusion defects, to generate the strain fields for use in our analysis. Crystalline dislocations were also considered for this, but were not examined due to technical difficulties (the singularity in the centre of the dislocation could not be handled correctly using ARC4). Whilst other defect types and strain structures were not considered, there is ample room to do so using our model; as long as the strain field can be entered as an initial condition, or is able to be calculated using MOOSE's Tensor Mech-

anics module, it can be used in our package, but was not done here due to time constraints.

BIBLIOGRAPHY

- [1] S. Blundell, *Magnetism in Condensed Matter*, n/a ed., Oxford Master Series in Condensed Matter Physics (Oxford University Press, 2003).
- [2] R. Hertel, O. Fruchart, S. Cherifi, P.-O. Jubert, S. Heun, A. Locatelli, and J. Kirschner, [Phys. Rev. B **72**, 214409 \(2005\)](#).
- [3] A. Vansteenkiste, J. Leliaert, M. Dvornik, M. Helsen, F. Garcia-Sanchez, and B. Van Waeyenberge, [AIP Advances **4**, 107133 \(2014\)](#).
- [4] C. D. Hansen and C. R. Johnson, eds., “Visualization Handbook,” (Elsevier, 2005) Chap. 36, p. 717, j. Ahrens, B. Geveci and C. Law, ParaView: An End-User Tool for Large Data Visualization.
- [5] D. Bacon, D. Barnett, and R. Scattergood, [Prog. Mater. Sci. **23**, 51 \(1980\)](#).
- [6] C. Meyer, “[Crack-inclusion interaction: A review](#),” (2014).
- [7] C. J. Permann, D. R. Gaston, D. Andrš, R. W. Carlsen, F. Kong, A. D. Lindsay, J. M. Miller, J. W. Peterson, A. E. Slaughter, R. H. Stogner, and R. C. Martineau, [SoftwareX **11**, 100430 \(2020\)](#).
- [8] P. Hirel, *Computer Physics Communications* **197**, 212 (2015).
- [9] A. Stukowski, [Model. Simul. Mater. Sci. Eng. **18**, 015012 \(2009\)](#).
- [10] G. Meunier, *The Finite Element Method for Electromagnetic Modeling*, n/a ed., N/A (John Wiley & Sons, Ltd, 2008).
- [11] L. Néel, [Ann. de Physique **10**, 5 \(1932\)](#).

-
- [12] B. Barbara, [Comptes Rendus Physique](#) **20**, 631 (2019).
- [13] M. L. Néel, [Ann. de Physique](#) **12**, 137 (1948).
- [14] W.-H. Hsu and R. Victora, [J. Magn. Magn. Mater.](#) **563**, 169973 (2022).
- [15] T. Jungwirth, X. Marti, P. Wadley, and J. Wunderlich, [Nat. Nanotechnol.](#) **11**, 231 (2016).
- [16] K. Olejník, T. Seifert, Z. Kašpar, V. Novák, P. Wadley, R. P. Campion, M. Baumgartner, P. Gambardella, P. Němec, J. Wunderlich, J. Sinova, P. Kužel, M. Müller, T. Kampfrath, and T. Jungwirth, [Sci. Adv.](#) **4**, eaar3566 (2018).
- [17] X. Marti, I. Fina, C. Frontera, J. Liu, P. Wadley, Q. He, R. J. Paull, J. D. Clarkson, J. Kudrnovský, I. Turek, J. Kuneš, D. Yi, J.-H. Chu, C. T. Nelson, L. You, E. Arenholz, S. Salahuddin, J. Fontcuberta, T. Jungwirth, and R. Ramesh, [Nat. Mater.](#) **13**, 367 (2014).
- [18] K. Olejník, V. Schuler, X. Marti, V. Novák, Z. Kašpar, P. Wadley, R. P. Campion, K. W. Edmonds, B. L. Gallagher, J. Garces, M. Baumgartner, P. Gambardella, and T. Jungwirth, [Nat. Commun.](#) **8**, 15434 (2017).
- [19] V. Brehm, J. W. Austefjord, S. Lepadatu, and A. Qaiumzadeh, [Sci. Rep.](#) **13**, 13404 (2023).
- [20] K. W. E. O. J. Amin and P. Wadley, [Appl. Phys. Lett.](#) **117**, 010501 (2020).
- [21] M. J. Grzybowski, P. Wadley, K. W. Edmonds, R. Beardsley, V. Hills, R. P. Campion, B. L. Gallagher, J. S. Chauhan, V. Novak, T. Jungwirth, F. Maccherozzi, and S. S. Dhesi, [Phys. Rev. Lett.](#) **118**, 057701 (2017).
- [22] H. Meer, O. Gomonay, C. Schmitt, R. Ramos, L. Schnitzspan, F. Kronast, M.-A. Mawass, S. Valencia, E. Saitoh, J. Sinova, L. Baldrati, and M. Kläui, [Phys. Rev. B](#) **106**, 094430 (2022).
- [23] A. Wittmann, O. Gomonay, K. Litzius, A. Kaczmarek, A. E. Kossak, D. Wolf, A. Lubk, T. N. Johnson, E. A. Tremsina, A. Churikova, F. Büttner, S. Wintz, M.-A. Mawass, M. Weigand, F. Kronast, L. Scipioni, A. Shepard, T. Newhouse-Illige, J. A. Greer, G. Schütz, N. O. Birge, and G. S. D. Beach, [Phys. Rev. B](#) **106**, 224419 (2022).
- [24] S. Reimers, O. Gomonay, O. J. Amin, F. Krizek, L. X. Barton, Y. Lytvynenko, S. F. Poole, V. Novák, R. P. Campion, F. Maccherozzi, G. Carbone, A. Björling, Y. Niu, E. Golias,

- D. Kriegner, J. Sinova, M. Kläui, M. Jourdan, S. S. Dhesi, K. W. Edmonds, and P. Wadley, *Phys. Rev. Appl.* **21**, 064030 (2024).
- [25] P. Li, J. Chen, R. Du, and X.-P. Wang, *IEEE Trans. Magn.* **56**, 1 (2020).
- [26] O. Gomonay and D. Bossini, *J. Phys. D: Appl. Phys.* **54**, 374004 (2021).
- [27] S. Reimers, D. Kriegner, O. Gomonay, D. Carbone, F. Krizek, V. Novák, R. P. Campion, F. Maccherozzi, A. Björling, O. J. Amin, L. X. Barton, S. F. Poole, K. A. Omari, J. Michalička, O. Man, J. Sinova, T. Jungwirth, P. Wadley, S. S. Dhesi, and K. W. Edmonds, *Nat. Commun.* **13**, 724 (2022).
- [28] T. Moriyama, L. Sánchez-Tejerina, K. Oda, T. Ohkochi, M. Kimata, Y. Shiota, H. Nojiri, G. Finocchio, and T. Ono, *Phys. Rev. Mater.* **7**, 054401 (2023).
- [29] G. Consolo, O. V. Gomonay, and P. Vergallo, *Ricerche di Matematica* (2023), [10.1007/s11587-023-00799-5](https://doi.org/10.1007/s11587-023-00799-5).
- [30] Z. Hong and V. Viswanathan, *ACS Energy Lett.* **3**, 1737 (2018).
- [31] G. R. Lázaro, I. Pagonabarraga, and A. Hernández-Machado, *Chem. Phys. Lipids* **185**, 46 (2015).
- [32] J. Wang and J. Zhang, *Int. J. Solids Struct.* **50**, 3597 (2013).
- [33] H. Kragh, *Niels Bohr and the quantum atom : the Bohr model of atomic structure, 1913-1925*, 1st ed., N/A (Oxford University Press, 2012).
- [34] M. d' Aquino, *Nonlinear Magnetization Dynamics in Thin-films and Nanoparticles*, Ph.D. thesis, Università degli studi di Napoli "Federico II" (2004).
- [35] J. B. Goodenough, *Phys. Rev.* **100**, 564 (1955).
- [36] J. B. Goodenough, *J. Phys. Chem. Solids* **6**, 287 (1958).
- [37] J. Kanamori, *J. Phys. Chem. Solids* **10**, 87 (1959).
- [38] H. Weihe and H. U. Güdel, *Inorg. Chem.* **36**, 3632 (1997).
- [39] A. Sapozhnik, *Magnetic Properties of Antiferromagnetic Mn₂Au: Exchange Interaction and Domain Manipulation*, Ph.D. thesis, Johannes Gutenberg-Universität Mainz (2018).

- [40] N. B. Weber, H. Ohldag, H. Gomonaj, and F. U. Hillebrecht, *Phys. Rev. Lett.* **91**, 237205 (2003).
- [41] E. V. Gomonay and V. M. Loktev, *Low Temp. Phys.* **30**, 804 (2004).
- [42] G. Consolo, O. V. Gomonay, and P. Vergallo, *Ricerche di Matematica* (2023), [10.1007/s11587-023-00799-5](https://doi.org/10.1007/s11587-023-00799-5).
- [43] A. P. Sutton, *Physics of Elasticity and Crystal Defects*, 1st ed., Oxford Series on Materials Modelling (Oxford University Press, 2020).
- [44] C. P. Society, *Transactions of the Cambridge Philosophical Society*, n/a ed., N/A (Cambridge University Press, 1833-1835).
- [45] J. F. Nye, *Physical properties of crystals : their representation by tensors and matrices*, n/a ed., N/A (Oxford University Press, 1957).
- [46] C. Kittel, *Rev. Mod. Phys.* **21**, 541 (1949).
- [47] G. C. Fletcher, *Proc. Phys. Soc.. Sect. A* **68**, 1066 (1955).
- [48] R. Wu, L. Chen, and A. Freeman, *J. Magn. Magn. Mater.* **170**, 103 (1997).
- [49] D. Fritsch and C. Ederer, *Phys. Rev. B* **86**, 014406 (2012).
- [50] N. Ekreem, A. Olabi, T. Prescott, A. Rafferty, and M. Hashmi, *J. Mater. Process. Technol.* **191**, 96 (2007).
- [51] T. Nussle, *Theoretical and Computational Studies of the Thermomechanics of Magnetic Materials*, Ph.D. thesis, University of Tours, University of Orleans (2019).
- [52] R. R. Birss, *Symmetry and Magnetism*, 1st ed., Series of Monographs on Selected Topics in Solid State Physics (North-Holland Publishing Company - Amsterdam, 1964).
- [53] Ö. Özdemir and D. J. Dunlop, *J. Geophys. Res.: Solid Earth* **102**, 20211 (1997).
- [54] J. D. Eshelby, *Proc. R. Soc. A* **241**, 376 (1957).
- [55] G. I. Taylor, *Proc. R. Soc. A* **145**, 362 (1934).
- [56] J. M. Burgers, *Proc. Kon. Ned. Akad. v. Wetensch.* **42**, 293 (1939).

- [57] I. Steinbach, *Annu. Rev. Mater. Res.* **43**, 89 (2013).
- [58] L.-Q. Chen and W. Yang, *Phys. Rev. B* **50**, 15752 (1994).
- [59] F. Xue, Y. Lei, T.-L. Cheng, W. K. Epting, G. Hackett, H. Abernathy, and Y.-H. Wen, *Int. J. Hydrogen Energy* **48**, 9845 (2023).
- [60] N. Goldenfeld, *Lectures on Phase Transitions and the Renormalisation Group*, 1st ed., Frontiers in Physics (Westview Press, 1992).
- [61] S. Allen and J. Cahn, *Acta Met.* **20**, 423 (1972).
- [62] I. Cimrak and M. Slodicka, *J. Comput. Appl. Math.* **169**, 17 (2004).
- [63] B. S. Kirk, J. W. Peterson, R. H. Stogner, and G. F. Carey, *Eng. with Comput.* **22**, 237 (2006).
- [64] S. Balay, W. D. Gropp, L. C. McInnes, and B. F. Smith, in *Modern Software Tools in Scientific Computing*, edited by E. Arge, A. M. Bruaset, and H. P. Langtangen (Birkhuser Press, 1997) pp. 163–202.
- [65] S. Balay, S. Abhyankar, M. F. Adams, J. Brown, P. Brune, K. Buschelman, L. Dalcin, V. Eijkhout, W. D. Gropp, D. Kaushik, M. G. Knepley, L. C. McInnes, K. Rupp, B. F. Smith, S. Zampini, and H. Zhang, *PETSc Users Manual*, Tech. Rep. ANL-95/11 - Revision 3.6 (Argonne National Laboratory, 2015).
- [66] S. Balay, S. Abhyankar, M. F. Adams, J. Brown, P. Brune, K. Buschelman, L. Dalcin, V. Eijkhout, W. D. Gropp, D. Kaushik, M. G. Knepley, L. C. McInnes, K. Rupp, B. F. Smith, S. Zampini, and H. Zhang, “PETSc Web page,” <http://www.mcs.anl.gov/petsc> (2015).
- [67] D. Schwen, L. Aagesen, J. Peterson, and M. Tonks, *Computational Materials Science* **132**, 36 (2017).
- [68] A. Lindsay, G. Giudicelli, P. German, J. Peterson, Y. Wang, R. Freile, D. Andrs, P. Balestra, M. Tano, R. Hu, *et al.*, *SoftwareX* **23**, 101503 (2023).
- [69] R. Herman, *Introduction to Partial Differential Equations*, n/a ed., N/A (LibreTexts, 2024).

- [70] J. C. Butcher, *J. Comput. Appl. Math.* **125**, 1 (2000).
- [71] Z. Li, Z. Qiao, and T. Tang, *Numerical Solution of Differential Equations: Introduction to Finite Difference and Finite Element Methods*, n/a ed., N/A (Cambridge University Press, 2017).
- [72] A. Leissa, *J. Sound Vib.* **287**, 961 (2005).
- [73] M. D. Kuz'min, K. P. Skokov, L. V. B. Diop, I. A. Radulov, and O. Gutfleisch, *Eur. Phys. J. Plus* **135**, 301 (2020).
- [74] B. D. Cullity and C. D. Graham, *Introduction to Magnetic Materials*, 2nd ed., N/A (Wiley-IEEE Press, 2009).
- [75] A. G. Gurevich and G. A. Melkov, *Magnetization oscillations and waves*, 1st ed., N/A (CRC Press, 1996).
- [76] M. Miller, J. Hyde, M. Hetherington, A. Cerezo, G. Smith, and C. Elliott, *Acta Met. et Materialia* **43**, 3385 (1995).
- [77] S. Kucheyev, J. Williams, and S. Pearton, *Mater. Sci. Eng.: R: Rep.* **33**, 51 (2001).
- [78] H. Benzerouk, F. Chouit, M. Mekhnache, L. Saad Hamideche, and A. Drici, *Mater. Sci. Eng.: B* **303**, 117323 (2024).
- [79] S.-W. Cheong, M. Fiebig, W. Wu, L. Chapon, and V. Kiryukhin, *npj Quantum Mater.* **5**, 3 (2020).